Doctoral Dissertation
Search for charged stable massive particles in 7 TeV proton-proton collisions with the ATLAS detector at the LHC

アトラス検出器による LHC の 7 TeV 陽子衝突データを用いた荷電長寿命重粒子探索

Shogo OKADA

Graduate School of Science
Kobe University

January 2011

Abstract

ATLAS is one of the experiments at the LHC, which is the largest proton-proton collider at CERN. The LHC collider has already achieved 7 TeV collisions, the highest energy human-made scatterings. The major purposes of the ATLAS experiment are to find Higgs boson in the Standard Model and to search for new physics beyond the Standard Model.

Some of beyond the Standard Models (e.g. Supersymmetry) predict the existence of charged stable massive particles (SMPs), which do not decay to other particles in the detector. Charged SMPs will reach the ATLAS muon system with high transverse momenta. They behave as "slowly-moving heavy muons" because their mass should be more than about 100 GeV. The existence of charged SMPs lighter than about 100 GeV are already excluded by previous experiments.

The ATLAS standard muon tracking algorithm measures muon momentum from their curvature using drift time information of muon spectrometers with an assumption that muons run at the speed of light from the proton-proton interaction point. If charged SMPs reach the muon spectrometers, their tracks will be reconstructed as muons. However, the hit points in the muon detector can be aligned on a trajectory only by assuming correct arrival time of the SMPs. This was utilized for measuring the velocity of SMPs.

An algorithm to measure the velocity using drift time information was developed and implemented in the ATLAS standard muon tracking algorithm. The performance of the velocity measurement algorithm was evaluated using both the Monte Carlo simulation and muons in 7 TeV proton-proton collisions. A search for charged SMPs was performed using 7 TeV collision data collected in 2010 by the ATLAS detector. The data analyzed corresponds to an integrated luminosity of 37.4 pb^{-1}. Events with an SMP were searched for by requesting a slow track in the muon detector with additional requirements on jets and missing transverse momentum, assuming that the SMP is produced via a cascade decay of heavier states. An upper limit of production cross section of charged stabled massive sleptons has been obtained.

Contents

Chapter 1

Introduction

1.1   The goal of the LHC

The smallest constituents of matter are called elementary particles. Thorough various experiments for about 100 years [*1)], it is found that there are twelve types of elementary particles. They are categorized two groups, quarks and leptons of three generations, where each generation consists of two quarks and two leptons. All atoms consist of the quarks and leptons.

The interactions between elementary particles are described by the Standard Model. The Standard Model is based on the gauge theory and all interaction are mediated by gauge bosons. The strong, electromagnetic and weak interactions are mediated by gluons (g), photons (γ) and W or Z bosons, respectively.

In a naive gauge theory, gauge bosons should be massless to keep the invariance under gauge transformations. However, W and Z bosons have been found to be massive from the result of the UA1 and UA2 experiments at the S$p\bar{p}$S collider at the European Organization for Nuclear Research (CERN). The Higgs mechanism is introduced in order to explain the existence of their masses. The W and Z bosons interact with the Higgs field and they obtain their masses by the spontaneous symmetry breaking of the vacuum of the Higgs field. Higgs searches have been performed for more than twenty years at the Large Electron-Positron (LEP) Collider at CERN and the Tevatron collider at Fermi National Accelerator Laboratory (Fermilab). The Large Hadron Collider (LHC) is expected to discover the Higgs boson.

According to the Higgs mechanism, a neutral Higgs boson appears in the Standard Model. However, even if the Higgs boson is discovered, there still exist a problem called "the hierarchy problem": the mass of the Higgs boson should have quadratic divergence assuming that the Standard Model is valid to the higher energy scale, for example, the GUT scale ($\Lambda \sim 10^{15}$ GeV) or the Planck scale ($\Lambda \sim 10^{18}$GeV).

Supersymmetry is considered as one of the solutions of this problem. It is a symmetry that relates bosons to fermions. In the Minimal Supersymmetric Standard Model (MSSM), there are new elementary particles, whose spins differ by one half compared to ordinary particles in the Standard Model. They are called "superpartners". The lightest super part-

---

[*1)]Electron was discovered by Joseph John Thomson in 1897. Tau neutrino was discovered at Fermilab in 2000.

ner (LSP) is considered as the candidate of the Cold Dark Matter, if R-parity conservation is assumed. Superpartners are considered to have masses close to the TeV energy scale. Therefore, the discovery of superpartners is expected at the LHC.

In the year 2008, the LHC at CERN came into operation. It is the world's largest proton-proton synchrotron collider, accelerating bunches of protons to 7 TeV and resulting in the world's highest center of mass energy of 14 TeV in its design. This is 7 times higher than that of the Tevatron, the most powerful hadron collider in the past. The LHC can produce the energy scale up to a few TeV center-of-mass energy parton-parton collisions, which is enough to produce the new particles.

Another feature of the LHC is its high design luminosity of 10^{34} cm^{-2}s^{-1}, with which studies of rare physics processes can be performed. To achieve such high luminosity, the bunch crossing rate is planned to have 40 MHz, corresponding to about 10^9 collision events per second.

At one of the four collision points at the LHC, a general-purpose detector called ATLAS (A Toroidal LHC ApparatuS) has been built. The detector is 22 m in height and 44 m in length and its weight is about 7000 t. In the experiment, various physics studies are being performed.

1.2 Search for Charged Stable Massive Particles in the AT-LAS experiment

Existence of charged stable massive particles (SMP) are predicted by some of the theories beyond the Standard Model (e.g. Supersymmetry), which are expected to be discovered at the ATLAS experiment. For example, scalar tau ($\tilde{\tau}$), the superpartner of tau (τ) in the Standard Model, might become the charged SMP in the gauge mediated supersymmetry-breaking (GMSB) model. From the results of previous experiments, the lower limit of charged SMP's mass is set to be about 100 GeV. If charged SMPs are generated with high momenta in proton-proton collisions, they will reach the muon spectrometers, the outermost detector of ATLAS, and behave as "slowly-moving heavy muons". When the velocity ($\beta = v/c$) and the momentum (p) of a charged SMP are measured with the muon spectrometers, their mass (m) is calculated with the following formula:

$$m = \frac{p}{\beta\gamma}, \tag{1.1}$$

where $\gamma = 1/\sqrt{1 - \beta^2}$.

Muon spectrometers of the ATLAS detector consist of four types of detectors. The MDT and the CSC measure the position of muon hits precisely. The RPC and the TGC are muon trigger chambers in the barrel regions and the endcap regions, respectively. By assuming that muons run at the speed of light ($\beta = 1$) from the proton-proton collision points, the ATLAS standard muon tracking algorithms reconstruct muon tracks using the drift time information of the MDT and the ϕ positions of muon hits of the RPC or the TGC.

If charged SMPs reach the muon spectrometers, their tracks are reconstructed as muons. However, drift circles of charged SMP's tracks are overestimated due to late arrival at the muon spectrometers and may not be fitted to a track well. In addition, it is possible that

muon trigger hits are not recorded in the nominal bunch crossing (BC), but in the next BC. The lack of ϕ hits in RPC/TGC makes muon track reconstruction impossible. Therefore, a special track reconstruction was developed in search for charged SMPs.

A track reconstruction algorithm, MuonBetaRefitTool, has been developed in order to detect charged SMPs by correctly solving the problems mentioned above. The algorithm determines β by re-estimating the drift circles traversed "seed-tracks", which are reconstructed with drift circles assuming a particular β value.

In Spring 2010, the LHC started to collect physics data at the center of mass energy of 7 TeV. The performance study of MuonBetaRefitTool has been made using muons in 7 TeV collisions.

The search for charged SMPs was performed using collision data collected from August 2010 to November 2010. A 95% C.L. upper limit on the production cross section was obtained assuming that charged SMPs were generated in the GMSB model.

1.3 Outline of this thesis

This thesis contains the following contents. Chapter 2 describes the physics motivation of the ATLAS experiment. In Chapter 3, a brief description of the LHC and the ATLAS experiment is given. Chapter 4 summaries the Monte Carlo samples used in the performance study of MuonBetaRefitTool and the search for charged SMPs. Chapter 5 describes the standard algorithm of muon track reconstruction in ATLAS, the problem of charged SMP reconstruction by using it, and development of the algorithm for velocity determination of charged SMPs with ATLAS Muon spectrometers. In chapter 6, the performance of the reconstruction of charged SMPs by using the Monte Carlo samples and 7 TeV collision data is described. Chapter 7 describes the search for charged SMPs by using 7 TeV collision data collected in 2010 assuming that charged SMPs are generated in the GMSB model. Chapter 8 gives the summary.

Chapter 2

Physics motivation of the ATLAS experiment

2.1 The Standard Model

The Standard Model (SM) describes the electroweak and strong interactions of spin-1/2 point-like fermions, whose interactions are mediated by spin-1 gauge bosons up to the energy scale of ~ 200 GeV [1, 2, 3].

The fermions are divided into a category of particles that are insensitive to the strong interactions, the leptons, and a category of particles that are subject to the strong interactions, the quarks. They are ordered in three generations. Each generation consists of two leptons and two quarks, each set with a difference of unit electric charge. The first generation consists of the electron (e), the electron neutrino (ν_e), the up quark (u) and the down quark (d). All these fermions are stable and are the building blocks of ordinary matter. The up and down quarks form protons and neutrons, which together with the electrons build up atoms and subsequently all forms of matter. The second generation consists of the muon (μ), the muon neutrino (ν_μ), the charm quark (c) and the strange quark (s). The third generation consists of the tau (τ), the tau neutrino (ν_τ), the top quark (t) and the bottom quark (b). These particles in the second and third generations have the same properties as the first generation particles, except they have larger masses and are not stable. The neutrinos are neutral particles while all other particles are charged.

The gauge bosons play roles in communicating interactions between fermions in the Standard Model. The electroweak interactions are mediated by the photon (γ) and weak bosons ($W^{\pm}$, Z^0). The strong interaction is mediated by the gluon (g). While the photon and gluon are massless particles, $W^{\pm}$ and Z^0 bosons are massive, whose masses are $M_W = 80.399 \pm 0.023$ GeV and $M_Z = 91.1876 \pm 0.0021$ GeV, respectively [4].

2.1.1 Higgs mechanism

Although all gauge bosons are necessarily massless in order to keep the gauge invariance under the local gauge transformations, the gauge bosons related to weak interactions, $W^{\pm}$ and Z^0, are massive particles, and their masses are measured precisely at LEP/SLC and the Tevatorn collider. The Higgs mechanism [5, 6, 7] provides a possible explanation of the origin of masses through the spontaneous symmetry breaking of the gauge invariance.

8

The Higgs mechanism is an extension of the Nambu-Goldstone Theorem, which states that if a Lagrangian has a global symmetry, which is not a symmetry of the vacuum. In the Higgs mechanism, a weak isospin doublet of complex scalar fields $\phi^0(x)$ and $\psi^+(x)$ is introduced as follows:

$$\phi(x) = \begin{pmatrix} \phi^+(x) \\ \phi^0(x) \end{pmatrix} = \frac{1}{\sqrt{2}} \begin{pmatrix} \phi_1(x) + i\phi_2(x) \\ \phi_3(x) + i\phi_4(x) \end{pmatrix}. \tag{2.1}$$

It belongs to the $SU(2)_L \otimes U(1)_Y$ multiplets. The scalar potential $V(\phi)$ is represented as:

$$V(\phi) = \mu^2 \phi^\dagger \phi + \lambda (\phi^\dagger \phi)^2, \; \lambda > 0. \tag{2.2}$$

This gives a contribution to the electroweak Lagrangian $\mathcal{L}$ as:

$$\mathcal{L}_{\text{Higgs}} = (D_\mu \phi)^\dagger (D_\mu \phi) - V(\phi), \; D^\mu = \partial^\mu - i\frac{g}{2}\sigma \cdot \mathbf{W}^\mu - i\frac{g\prime}{2}YB^\mu, \tag{2.3}$$

where D_μ is the covariant derivative.

The minimum of V corresponding to the ground state of the system (i.e. vacuum) is realized at $|\phi| = 0$ for the case $\mu^2 > 0$, while, for the case $\mu^2 < 0$, the minimum shifts to

$$|\phi|^2 = \phi^\dagger \phi = \frac{1}{2}(\phi_1^2 + \phi_2^2 + \phi_3^2 + \phi_4^2) = -\frac{\mu}{2\lambda} = \frac{v^2}{2}, \tag{2.4}$$

where v is the vacuum expectation value. This leads to a definition of new field variables, $\eta_1 = \phi_1$, $\eta_2 = \phi_2$, $\eta_3 = \phi_3 - v$ and $\eta_4 = \phi_4$. The potential takes the form as shown in Fig. 2.1. They have their origin at an arbitrarily minimum chosen as:

$$|\langle 0|\phi|0\rangle| = \frac{1}{\sqrt{2}} \begin{pmatrix} 0 \\ v \end{pmatrix}. \tag{2.5}$$

The symmetry of the Lagrangian becomes hidden by the choice of a particular minimum. The Lagrangian expressed in the new fields reveals a massive scalar particle η_3 of mass $\sqrt{2\lambda v^2}$, the Higgs boson H and three massless Goldstone bosons, ϕ_1, ϕ_2 and ϕ_4. These Goldstone bosons can be removed by applying a unitary gauge transformation to $\phi(x)$ such that only the real Higgs field remains like the following:

$$\phi(x) = U\phi(x) = \frac{1}{\sqrt{2}} \begin{pmatrix} 0 \\ v + H(x) \end{pmatrix}. \tag{2.6}$$

In this way, the degree of freedom corresponding to the three disappeared Goldstone boson are eaten by the $W^\pm$ and Z^0 fields which acquire mass and a third, longitudinal polarization state. Then, the gauge boson masses are generated as:

$$M_W = \frac{gv}{2}, \tag{2.7}$$

$$M_Z = \frac{1}{2}v\sqrt{g^2 + g\prime^2}, \tag{2.8}$$

$$M_\gamma = 0. \tag{2.9}$$
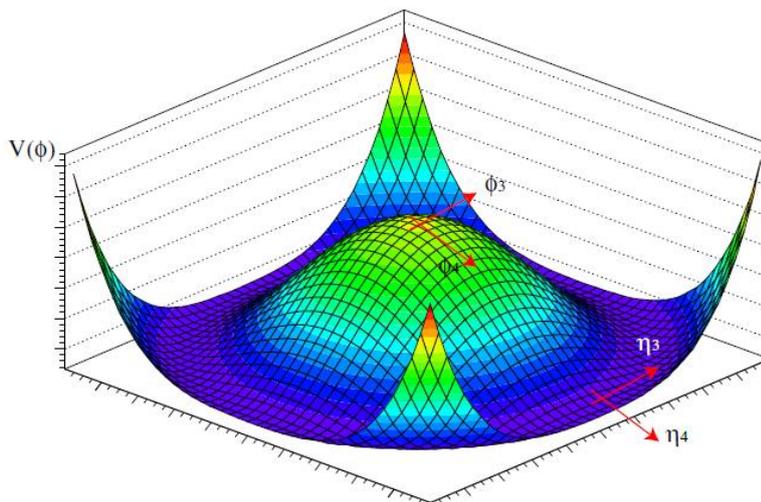
Figure 2.1: The Higgs potential for a complex scalar field with $\mu^2 < 0$ and $\lambda > 0$.

The massive physical field Z_μ and the massless one A_μ are represented using their mixing angle θ_W (called the Weinberg angle) as:

$$A_\mu = \cos\theta_W B_\mu + \sin W_\mu^3, \tag{2.10}$$

$$Z_\mu = -\sin\theta_W B_\mu + \cos\theta_W W_\mu^3, \tag{2.11}$$

where the value θ_W satisfies the following equation:

$$\frac{g'}{g} = \tan\theta_W. \tag{2.12}$$

In addition, the Higgs field couples to the fermion matter fields to generate their masses. The coupling of the Higgs field to a fermion pair is parameterized by an arbitrary Yukawa coupling constant $\lambda_f = \sqrt{2}m_f/v$, which is proportional to its mass m_f. Lepton number conservation is assumed within the SM, giving a diagonal lepton mass matrix. The lack of quark generation number conservation in electroweak interactions means that the observed physical mass eigenstates of quarks are not eigenstates of the weak isospin. The level of quark mixing is parameterized in terms of the Cabibbo-Kobayashi-Maskawa mixing matrix.

2.1.2 Experimental constraint of the Higgs mass

The mass of the Higgs boson can not be predicted by the Standard Model. From past experimental measurements, several constraints on the Higgs mass have been obtained. Higgs mass smaller than 114.4 GeV is excluded with a 95% confidence level by direct searches at the four LEP experiments [9]. In addition, the CDF and D0 experiments at the Tevatron collider have recently excluded the SM Higgs boson in the mass range of $160 < m_H < 170$ GeV [10].

An indirect upper bound on the SM Higgs mass can be obtained by a global electroweak fit assuming that the Standard Model is valid. The result is shown in Fig. 2.2. The yellow

areas correspond to the mass regions excluded at 95 % confidence level by direct searches at the LEP and the Tevatron. The associated band represents the estimated theoretical uncertainty due to higher-order corrections, where the constraints from the masses of the top quark and $W^{\pm}$ bosons measured at the Tevatron are included. An upper limit of the SM Higgs mass is obtained to be 157 GeV at 95 % confidence level with new precision measurements of the top quark [11] and $W^{\pm}$ boson [12] masses at the Tevatron.
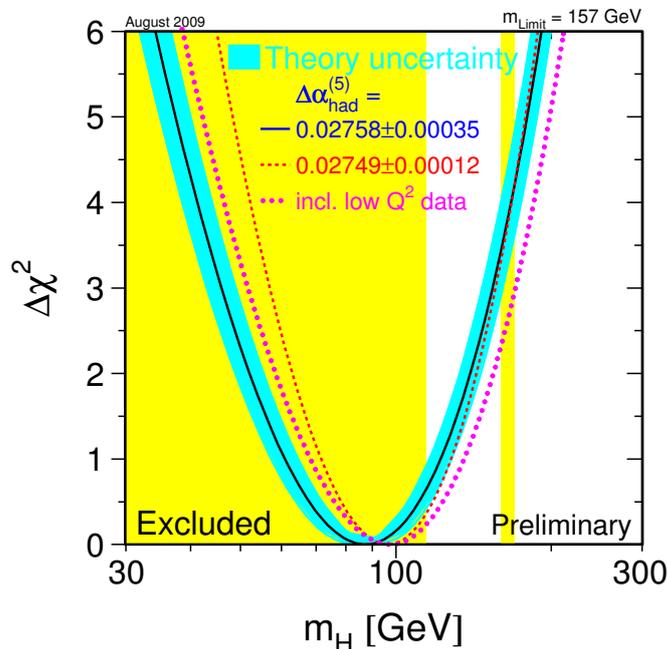
Figure 2.2: $\Delta\chi^2$ with respect to the minimum of the global fit to electroweak precision data as a function of the SM Higgs mass [10].

2.1.3   The production processes of the SM Higgs boson at the LHC

In this section, the production processes of the SM Higgs at the LHC are described in detail. Figure 2.4 shows the Feynman diagrams of such processes.

- $gg \rightarrow H$
  The gluon fusion (Fig. 2.4-(a)) proceeds primarily through a top quark triangle loop and is the dominant neutral Higgs boson production process at the LHC, with a cross section of roughly $200 \sim 0.1$ pb for $M_H = 100 \sim 1000$ GeV. The dependence of the gluon fusion cross section on different parton densities yields roughly a 15 % uncertainty in the theoretical prediction.

- $qq \rightarrow qqV^*V^* \rightarrow qqH$
  The vector boson fusion (VBF, Fig. 2.4-(b)) is a shorthand notation for the full
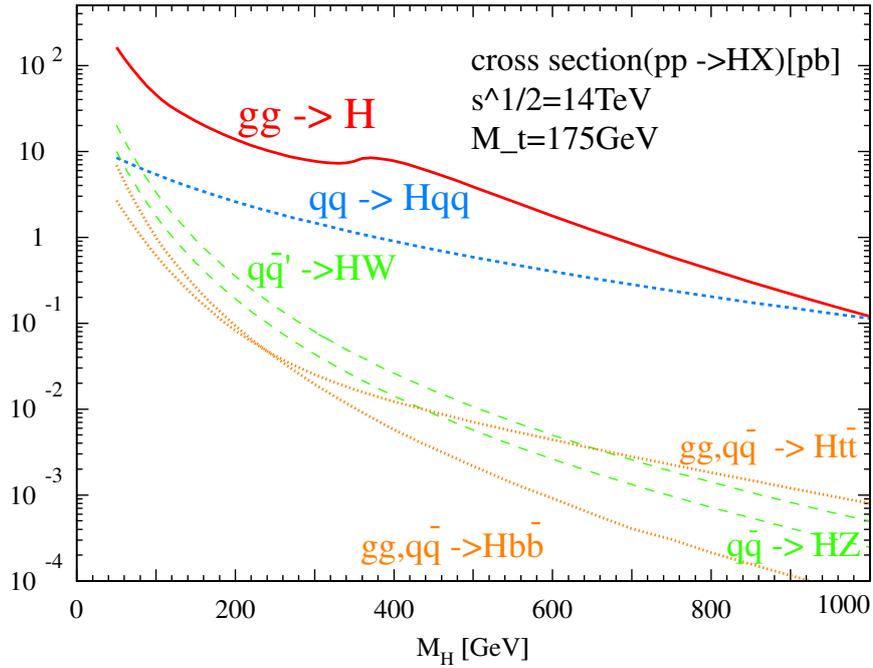
Figure 2.3: The production cross section of the SM Higgs as a function of the Higgs Mass M_H [13].

$qq \rightarrow qqH$ process, where both quarks radiate virtual vector bosons which then annihilate to produce the Higgs boson. The resulting Standard Model cross sections are in the range $5 \sim 0.01$ pb for $M_H = 100 \sim 1000$ GeV.

- $q\bar{q} \rightarrow V^* \rightarrow VH$
  The cross section for $q\bar{q} \rightarrow W^{\pm}H$ (Fig. 2.4-(c), summed over both W charge states) reaches values of $2 \sim 0.001$ pb for $M_H = 100 \sim 1000$ GeV/c^2. The corresponding $q\bar{q} \rightarrow ZH$ cross section is roughly a factor of two lower in the same Higgs boson mass range. The theoretical uncertainty is estimated to be about 15% from the remaining scale dependence. The dependence on different sets of parton densities is rather weak and leads to a variation of the production cross sections by about 15%. The signature of the Higgs boson production in the VH channel are governed by the decays of the Higgs boson and the vector bosons.

- $gg,\ qq \rightarrow t\bar{t}H$
  The process $gg,\ q\bar{q} \rightarrow t\bar{t}H$ (Fig. 2.4-(d)) is relevant only for small Higgs masses. The analytical expression for the parton cross section, even at lowest order, is quite involved, so that just the final results for the LHC cross section are shown in Fig. 2.3.
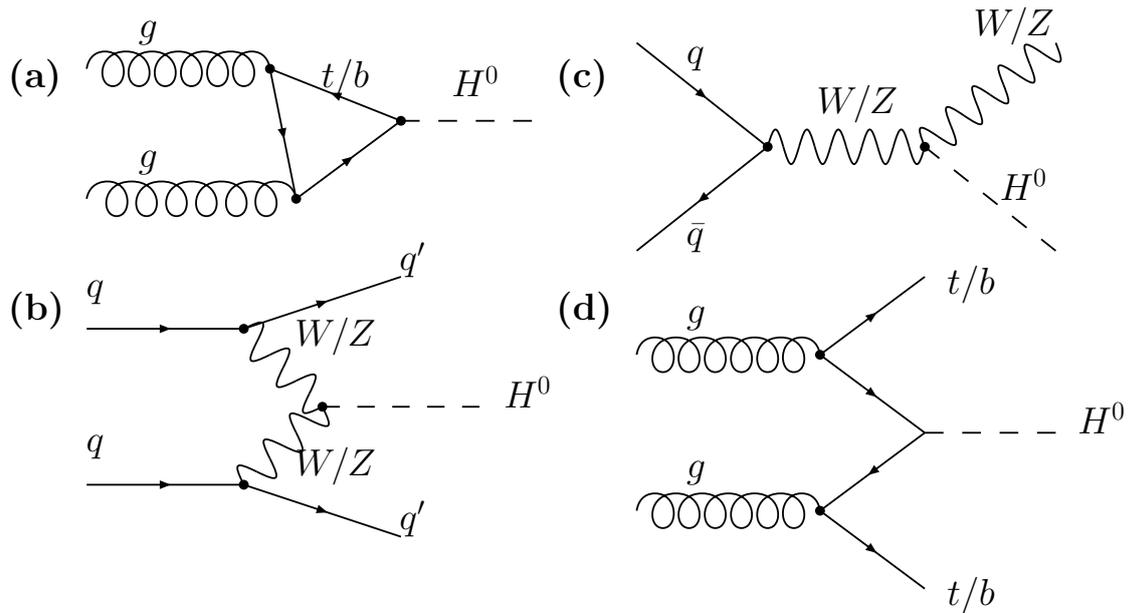
Figure 2.4: The Feynman diagram of production processes of the SM Higgs. (a) gluon fusion (b) Vector boson fusion (c)W/Z associate production process and (d) $t\bar{t}H$ production process.
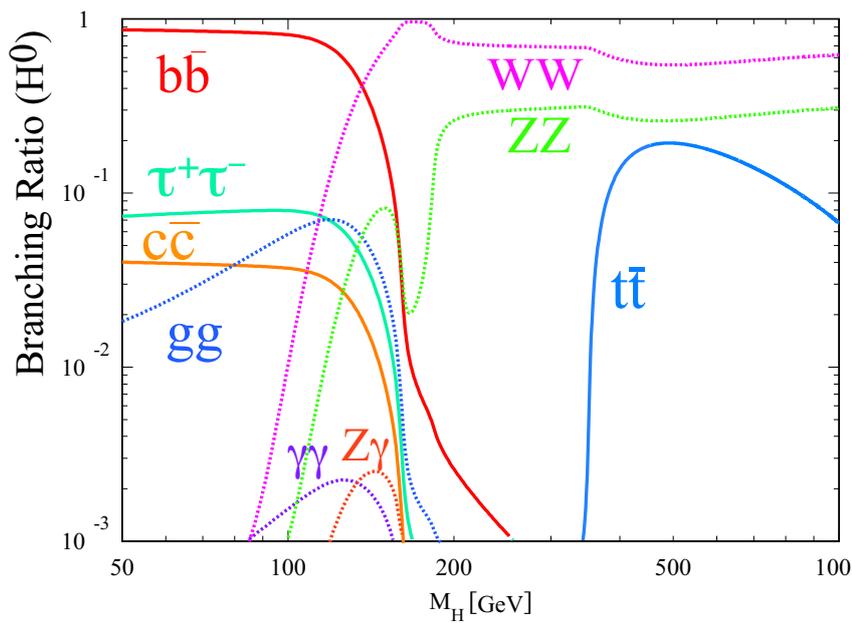
Figure 2.5: The decay branching ratio of the SM Higgs boson in terms of the Higgs mass M_H [13].

2.1.4 The decay processes of the SM Higgs boson

The Standard Model precisely predicts the decay processes of the Higgs boson if its mass is given. Figure 2.5 shows the decay branching rations of the Higgs boson in terms of its mass, M_H. In this section, the decay processes for each predicted mass of the Higgs are described.

- **Low-Mass Higgs boson** ($M_H < 120$ GeV)
  If M_H is below the WW threshold ($M_H < 2M_W$), the dominant decay process is $H \rightarrow b\bar{b}$. However, it is difficult to observe the signal of the Higgs due to high QCD backgrounds. Therefore, in this mass region, the search for Higgs boson will be mainly performed with following decay channel:

$$H \rightarrow \gamma\gamma. \tag{2.13}$$

  The main background processes are $q\bar{q} \rightarrow \gamma\gamma$, $gg \rightarrow \gamma\gamma$, $gq \rightarrow q\gamma\gamma$ and $Z \rightarrow e^+e^-$, where the jets or $e^\pm$ fake a γ. These backgrounds can be rejected with good photon energy resolution and γ/jet and $\gamma/e^\pm$ separation. Hence an electromagnetic calorimeter with excellent performance, both spacial separation and energy resolution is required.

- **Search for VBF $H \rightarrow \tau\tau$ mode**
  When the Higgs mass is relatively small ($115 < M_H < 140$ GeV), the search can be also made using the vector boson fusion process with

$$H \rightarrow \tau^+\tau^-. \tag{2.14}$$

  In this channel, since the branching ratio of hadronic tau decay is larger than that of leptonic tau decay by a factor of ~ 2, $\tau\tau \rightarrow$ leptonic decay + hadronic decay, so-called lepton-hadron mode, is as important as $\tau\tau \rightarrow$ leptonic decay + leptonic decay, so-called lepton-lepton mode. By using the mode, the $\tau\tau$ channel may lead to the first discovery of the SM Higgs. Since W and Z are heavy, the outgoing quarks have larger transverse momenta (p_T) than the QCD backgrounds. They will be observed in a forward region with high-p_T. Tagging these forward jets helps to suppress the backgrounds. Furthermore, since there is no color exchange between two outgoing quarks, the Higgs boson will be observed in large rapidity gap, where activities of QCD jets are small. A lepton with high-p_T is provided from leptonic tau decay, which are generated from $H \rightarrow \tau\tau$, and can be used as a trigger of this event. Momenta carried by neutrinos emitted from tau decays can be estimated using the missing transverse energy ($\not{E}_T$) information. Dominant background process is Drell-Yan with two high-p_T jets, whose invariant mass distribution makes a peak at the Z^0 mass.

- **Intermediate-mass Higgs boson** ($120 < M_H < 800$ GeV)
  The decay channel
$$H \rightarrow ZZ^{(*)} \rightarrow \ell^+\ell^-\ell^+\ell^- \tag{2.15}$$

  provides a very clean signature of the Higgs boson in this mass region. If the Higgs mass is less than double of the Z^0 boson mass ($M_H < 2M_Z$), one of the two Z^0 bosons is off-shell. The four leptons have high transverse momenta. The background mainly comes from prompt muons, decay muons, hadronic punch through, neutrons
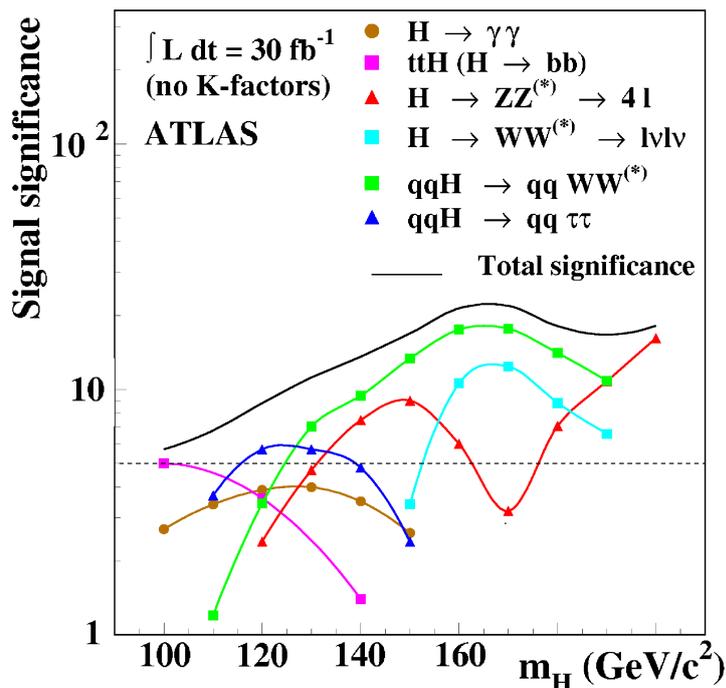
Figure 2.6: The sensitivity of the discovery of the SM Higgs at the ATLAS Experiment [14].

and muon induced electromagnetic secondaries. To achieve a good acceptance for the signal events, the geometrical and kinematic acceptance for leptons has to be maximized. The significance of the signal will depend on the four-lepton mass resolution in the low mass range. For large Higgs boson masses the Higgs width increases rapidly and the signal will be rate limited. The accelerator luminosity hence becomes more important than the detector performance.

- **Heavy-mass Higgs boson** ($M_H > 800$ GeV)
  The channel

$$H \to ZZ \to \ell^+\ell^-\nu\bar{\nu} \tag{2.16}$$

is six times more frequent than $H \to ZZ \to \ell^+\ell^-\ell^+\ell^-$ and can be detected with measurements of two high-p_T leptons and a high missing transverse energy $\not{E}_T$ due to escaping neutrinos at high mass. The channels

$$H \to WW, \; ZZ \to \ell^\pm + \nu + 2\text{jets}, \; 2\ell^\pm + 2\text{jets} \tag{2.17}$$

also provide promising signatures for a heavy Higgs boson. Since the Higgs boson decays to two W bosons in the mass region around 160 GeV dominantly, the $WW \to \ell\nu\ell\nu$ channel has high sensitivity in this mass range.
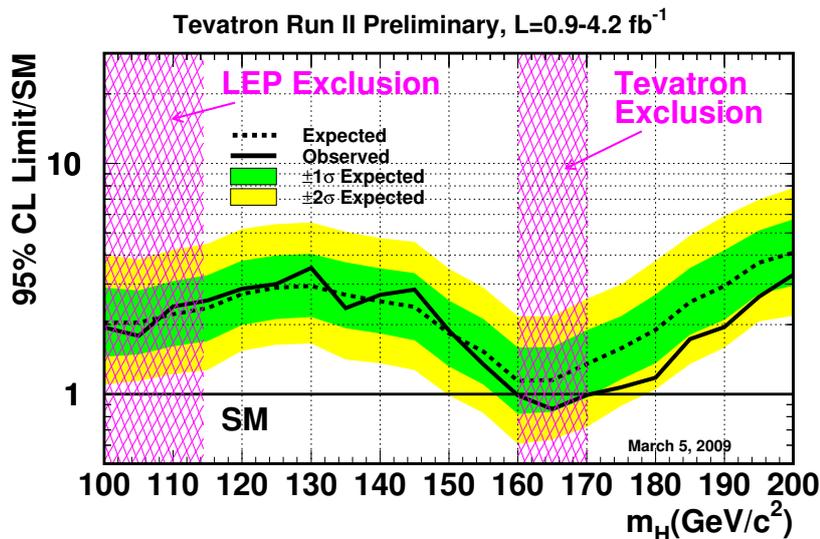
Figure 2.7: Observed and expected 95% C.L. upper limits on the ratios to the Standard Model cross section, as functions of the Higgs boson mass for the combined CDF and D0 analyses [10].

2.1.5   Discovery potential at ATLAS and Tevatron Exclusion for the SM Higgs boson

Figure 2.6 shows the sensitivity for the discovery of the Standard Model Higgs boson for several Higgs decay channels by the ATLAS experiment. The results shown here assume $\sqrt{s} = 14$ TeV and an integrated luminosity of 30 fb^{-1} which corresponds to the estimated data volume after the first three years of data taking. The figure shows that if the Higgs boson exists, the ATLAS experiment will be able to observe it with a 5σ statistical significance over the full mass range from 100 GeV up to 1 TeV.

Figure 2.7 shows the combined cross section limit relative to the Standard Model expectation. The limits are expressed as a multiple of the SM prediction for test masses (every 5 GeV) for which both the CDF and the D0 experiments have performed dedicated searches in different channels [10]. The points are joined by straight lines for better readability. The bands indicate the 68 % and 95 % probability regions where the limits can fluctuate, in the absence of signal. The limits displayed in this figure are obtained with the Bayesian calculation. This result is based on an effective luminosity of 2.6 fb^{-1} around masses of 115 GeV and 3.8 fb^{-1} at masses around 160 GeV. Observed and expected limits agree within one standard deviation and no indication of a Higgs boson signal has been observed. A mass range of 160 to 170 GeV has been excluded at the 95% C.L. This is the first direct exclusion of a SM Higgs in a mass range above the LEP limits.

2.2   Surpersymmetry

Supersymmetry[15, 16, 17, 18, 19] imposes a new symmetry between the fermions and bosons. The supersymmetric extension of the Standard Model makes improvements to phenomenological problems in the physics of elementary particles. It provides a natural solution for the gauge hierarchy problem by introducing one superpartner (sparticle) with mass at the TeV scale for each SM particle. Moreover, the extrapolation of LEP data within the framework of supresymmetric extension yields a precise unification of gauge couplings at a scale of $\sim 10^{16}$ GeV [20, 21]. Due to these reasons, SUSY has been one of the most attractive alternatives beyond the Standard Model and is the subject of many studies in particle physics. However, up to now, no direct evidence for SUSY has been found.

2.2.1   The Minimal Supersymmetric Standard Model (MSSM)

The Minimal Supersymmetric Standard Model (MSSM) extends the Standard Model by introducing one superpartner for each of the Standard Model particle. Table 2.1 shows the constituent particles of the MSSM.

The SM particles			The SUSY particles		
spin	name		spin	name	
1/2	quarks	$(u_L, d_L), (c_L, s_L), (t_L, b_L)$ $u_R, d_R, c_R, s_R, t_R, b_R$	0	squarks	$(\tilde{u}_L, \tilde{d}_L), (\tilde{c}_L, \tilde{s}_L), (\tilde{t}_L, \tilde{b}_L)$ $\tilde{u}_R, \tilde{d}_R, \tilde{c}_R, \tilde{s}_R, \tilde{t}_R, \tilde{b}_R$
1/2	leptons	$(\nu_{eL}, e_L), (\nu_{\mu L}, \mu_L), (\nu_{\tau L}, \tau_L)$ e_R, μ_R, τ_R	0	sleptons	$(\tilde{\nu}_{eL}, \tilde{e}_L), (\tilde{\nu}_{\mu L}, \tilde{\mu}_L), (\tilde{\nu}_{\tau L}, \tilde{\tau}_L)$ $\tilde{e}_R, \tilde{\mu}_R, \tilde{\tau}_R$
0	higgs	$h, H^0, A, H^{\pm}$	1/2	higgsino	$\tilde{H}_1^0, \tilde{H}_2^0, \tilde{H}^{\pm}$
1	gluon	g	1/2	gluino	$\tilde{g}$
1	photon	γ	1/2	bino	$\tilde{B}^0$
1	weak bosons	$W^{\pm}, Z^0$	1/2	winos	$\tilde{W}^{\pm}, \tilde{W}^0$
2	graviton	G	3/2	gravitino	$\tilde{G}$

Table 2.1: The particles in the MSSM

The superpartners of quarks and leptons are "squarks" and "sleptons", respectively, which have spin-0 and are bosons. The gauge bosons have superpartners called "gauginos" which are fermions. There is one Higgs doublet in the Standard Model while two Higgs doublets are introduced in the MSSM to avoid an anomaly problem. Three degrees of freedom are eaten by $W^{\pm}$ and Z^0 bosons in order to get their masses under the Electroweak symmetry breaking. On the other hand, remaining five degrees of freedom become five Higgs particles, h^0, H^0, A^0 and $H^{\pm}$. Their superpartners are $\tilde{H}_1^0, \tilde{H}_2^0$ and $\tilde{H}^{\pm}$ called "higgsino".

In the MSSM, conservation of a discrete symmetry called R-parity is assumed in order to avoid too-rapid proton decay. The R-parity is defined as follows:

$$R = (-1)^{3B-L+2S} = \begin{cases} +1 & \text{non SUSY} \\ -1 & \text{SUSY} \end{cases} \tag{2.18}$$

where B is the baryon number, L is the lepton number, and S is the spin. All the Standard Model particles carry even parity while their superpartners carry odd parity due to the $(-1)^{2S}$ factor. The R-parity conservation leads into the following collider phenomenology.

- In the collider experiments, SUSY particles should be generated in pairs under the conservation of the R-parity.

- The lightest SUSY particle (LSP) is stable due to its odd R-parity, and is expected to be a candidate of the cold dark matter. The LSP is seen as a massive neutral particle and hardly interacts other particles like neutrinos. Therefore, the large missing transverse energy is an important charasteristic in collider experiments.

If the supersymmetry is conserved completely, selectron and photino should have been discovered because they have the same mass of electron and photon, respectively. However, both SUSY particles have not been observed yet. Supersymmetry is broken. It is thought that SUSY breaking may occur at $\mathcal{O}(\text{TeV})$. When both supersymmetry and electroweak symmetry are broken, the mixing among particles with same quantum numbers occurs.

Charginos

The chargino $\tilde{\chi}^{\pm}_{1,2}$ are the physical mass eigenstates. The mass matrix of the charged gaugino is given by

$$M_{\tilde{\chi}^{\pm}} = \begin{pmatrix} M_2 & \sqrt{2}M_W \sin\beta \\ \sqrt{2}M_W \cos\beta & \mu \end{pmatrix}, \tag{2.19}$$

where M_2, M_W, μ are masses of charged gaugino $\tilde{W}^{\pm}$, $W^{\pm}$ boson, and higgsino, respectively, and β is the ratio of two vacuum expectation values for two Higgs fields $\tan\beta = \langle H_2 \rangle / \langle H_1 \rangle$. The mass eigenvalues of two charginos are given by

$$m^2_{\tilde{\chi}^+_1}, m^2_{\tilde{\chi}^+_2} = \frac{1}{2}\left[M_2^2 + \mu^2 + 2M_W^2 \pm \sqrt{(M_2^2 + \mu^2 + 2M_w^2)^2 - 4(\mu M_2 - M_W^2 \sin 2\beta)^2} \right]. \tag{2.20}$$

Neutralinos

Similarly, the neutralinos $\tilde{\chi}^0_{1,2,3,4}$ are the physical mass eigenstates given by the mass matrix in the basis $(\tilde{B}^0, \tilde{W}^0, \tilde{H}^0_1, \tilde{H}^0_2)$;

$$M_{\tilde{\chi}^0} = \begin{pmatrix} M_1 & 0 & -M_Z \cos\beta \sin\theta_W & M_Z \sin\beta \sin\theta_W \\ 0 & M_2 & M_Z \cos\beta \cos\theta_W & -M_Z \sin\beta \cos\theta_W \\ -M_Z \cos\beta \sin\theta_W & M_Z \cos\beta \cos\theta_W & 0 & -\mu \\ M_Z \sin\beta \sin\theta_W & -M_Z \sin\beta \cos\theta_W & -\mu & 0 \end{pmatrix}, \tag{2.21}$$

where M_1 and M_z are mass of neutral gaugino $\tilde{B}^0$ and Z^0 boson respectively, and θ_W is the Weinberg angle.

Sfermions

While chiral fermions f_L and f_R must have the same mass by Lorentz invariance, their superpartners $\tilde{f}_L$ and $\tilde{f}_R$ are scalars with separate masses. Their squared-mass matrix also gets off-diagonal contributions proportional to the fermion mass. The mass matrix of the top squark in the basis $(\tilde{t}_L, \tilde{t}_R)$ is given as follows:

$$M_{\tilde{t}}^2 = \begin{pmatrix} M_{\tilde{t}_L}^2 + m_t^2 + \frac{1}{6}(4M_W^2 - M_Z^2)\cos 2\beta & -m_t(A_t - \mu\cot\beta) \\ -m_t(A_t - \mu\cot\beta) & M_{\tilde{t}_R}^2 + m_t^2 - \frac{2}{3}(M_W^2 - M_Z^2)\cos 2\beta \end{pmatrix}.$$
(2.22)

The resulting left-right mixing is mainly important for the third generation. The eigenstates are called $\tilde{t}_{1,2}, \tilde{b}_{1,2}$ and $\tilde{\tau}_{1,2}$. There can also be mixings among generations of sfermions - including new sources of CP-violation.

2.2.2 Inclusive search for SUSY signature

The production of gluinos $\tilde{g}$ and squarks $\tilde{q}$ occurs dominantly via the strong interactions and its rate may be expected to be considerably large at the LHC. Figure 2.8 shows the Feynman diagrams for the production of $\tilde{g}$ and $\tilde{q}$. Since there are no third generation partons in the initial state, gluino and squark production rates are assumed by QCD as the function of masses of gluino and squark.

The model-independent feature of SUSY events is the multi jets (and leptons) with high transverse momentum generated via cascade decays of gluinos and/or squarks and the large missing transverse energy due to the LSP. Therefore, inclusive SUSY searches with early data rely on excesses of events in this channel. Table 2.2 shows the experimental signatures and the Standard Model backgrounds for each SUSY scenario. They cover realistic supersymmetric models of minimal supergravity (mSUGRA) [23, 24, 25, 26], anomaly mediated SUSY breaking (AMSB) model [27, 28] and gauge mediated SUSY breaking (GMSB) model [29, 30].
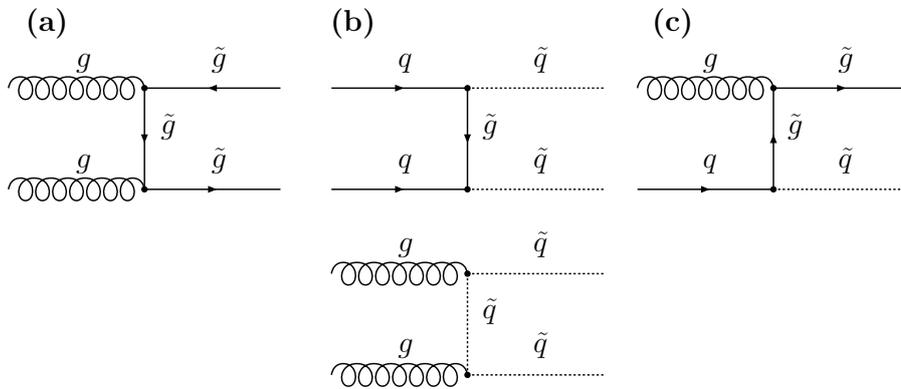

Figure 2.8: The production process of gluinos and squarks at the LHC. (a) is the $\tilde{g}\tilde{g}$ pair production. (b) (a) is the $\tilde{q}\tilde{q}$ pair production. (c) is the $\tilde{g}\tilde{q}$ associated production.

jet multiplicity	additional signature	covered scenario	background
$N_{\text{jet}} \geq 4$	no lepton	mSUGRA, AMSB, split SUSY, heavy squark	QCD, $t\bar{t}, W/Z$
	one lepton	mSUGRA, AMSB, split SUSY, heavy squark	$t\bar{t}, W$
	dilepton	mSUGRA, AMSB, GMSB	$t\bar{t}$
	ditau	GMSB, large $\tan\beta$	$t\bar{t}, W$
	$\gamma\gamma$	GMSB	——
$N_{\text{jet}} \sim 2$	——	light squark	Z

Table 2.2: Summary of experimental signatures with missing transverse energy and corresponding SUSY scenarios and the Standard Model background processes [31].

The effective mass M_{eff} is defined as

$$M_{\text{eff}} = \sum_{i=1}^{i\leq 4} p_{T,i} + \not{E}_T, \tag{2.23}$$

where $p_{T,i}$ is the transverse momentum of i-th leading jet, $\not{E}_T$ is the missing transverse energy. The value of M_{eff} provides a first estimate of the sparticle masses. SUSY events will be searched in the region of large M_{eff} where the signal exceeds the Standard Model backgrounds. Figure 2.9 shows the expected distributions of the effective mass for no and one lepton channels. If SUSY particles are generated at the LHC, the signal excess over the SM backgrounds are expected in the distribution for each event topology with an integrated luminosity up to 1 fb^{-1}.

5σ discovery reach in the $m_{\tilde{g}}$-$m_{\tilde{q}}$ space for each event topology in the mSUGRA model is shown in Fig. 2.10. The discovery of sparticles with $m \sim 1$ TeV are expected for an integrated luminosity of 1 fb^{-1}.
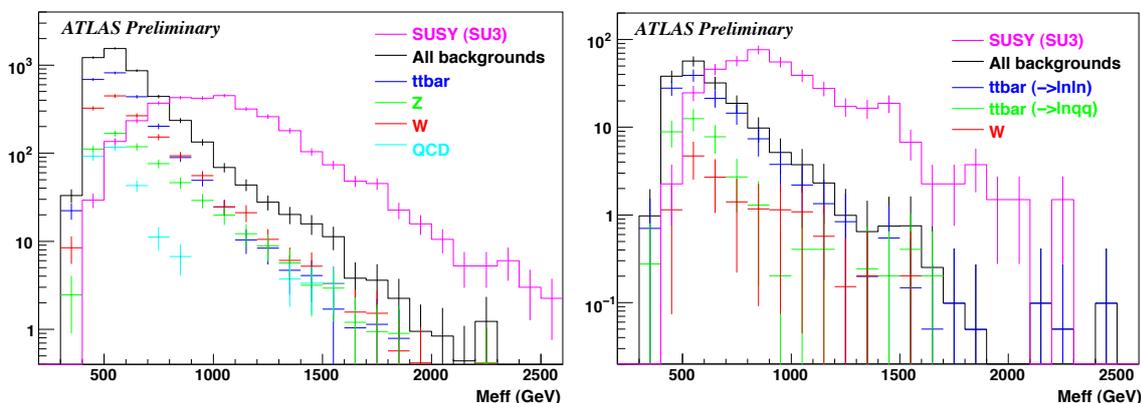

Figure 2.9: The M_{eff} distributions for no-lepton channel (left) and one-lepton channel normalized to the integrated luminosity 1 fb^{-1} [31].
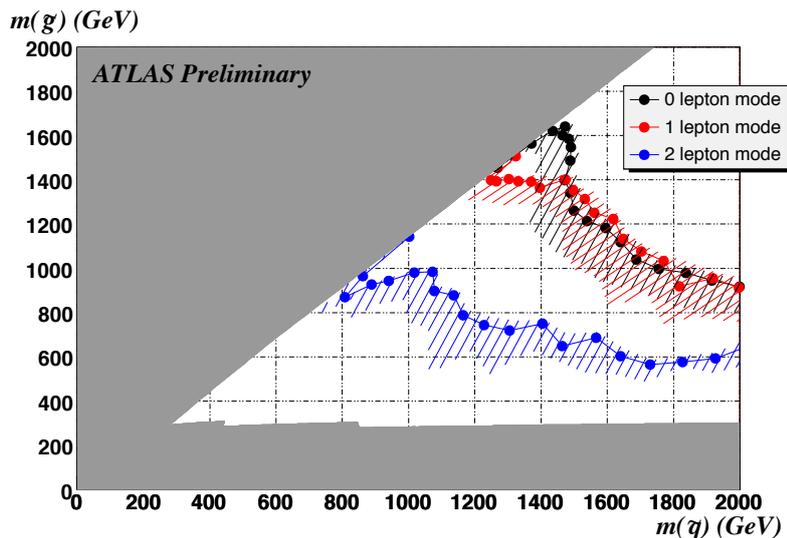
Figure 2.10: 5σ-discovery reaches in the $m_{\tilde{g}}$-$m_{\tilde{q}}$ space for each event topology [31].

2.3   Charged stable massive particles (SMPs)

Stable Massive Particles (SMPs) [32] are defined as particles which do not decay during their flight through detectors, and which would undergo electromegnetic and/or strong interactions with matter.

The most obvious possibility for SMPs is that new states exist which carry a new conserved global quantum number. For example, SUSY with R-parity and extra dimension with Kaluza-Klein (KK)-parity fall into this category. The lightest of the new states will be stable due to conservation of the new parity, and depending on quantum numbers, mass spectra and interaction strengths, one ore more higher-lying states may also be stable or meta-stable. In general, electrically charged stable states are excluded by cosmology, and also colored particles are strongly constrainted. For this reason, models are usually constructed to provide neutral stable dark-matter candidates, which are often weakly interacting massive particles (WIMPs). Therefore, SMP models come from following two categories:

- Models which have a WIMP-type dark matter candidate and one or more higher-lying meta-stable SMP states.

- Models which have SMP states, but which either do not address dark matter or address it with a non-WIMP type dark matter.

2.3.1   Charged SMPs in the GMSB model

In the Gauge mediated SUSY-breaking (GMSB) model [29, 30], the gravitino is very light ($M_{\tilde{G}} < 1$ keV) and is the LSP. Minimal model is specified in terms of six parameters:

$$\Lambda, M, N_m, \tan\beta, \mathrm{sgn}(\mu), C_{\mathrm{grav}}. \tag{2.24}$$

The phenomenological meaning and theoretical bounds of the GMSB parameters are summarized as follows:

- Λ is to set the scale of SUSY-breaking in the observable sector. Masses of SUSY particles are typically smaller by a one-loop factor than Λ, with coefficients completely determined by the particle gauge quantum numbers. The parameter Λ should be larger than several TeV so that the Higgs boson has a correct vacuum expectation value.

- M is the messenger scale, which affects supersymmetric masses logarithmically from their renormalized group evolution. The M should be larger than Λ, and well below the GUT scale (M_{GUT}) to guarantee flavor-invariant supersymmetry breaking mass terms.

- N_m is the messenger index. The maximum number of N_m can be bounded by requiring that the gauge interactions remain perturbative up to the GUT scale, although this bound depends on M: for $M = 100$ TeV, $N_m \leq 5$ while for $M = 10^{10}$ TeV, $N_m \leq 10$.

- $\tan\beta$ is the ratio of the Higgs vacuum expectation values, which affects the mixing angles between left- and right-handed sparticles, especially, the third generation sparticles. The upper limit is determined by a positiveness of mass squared of the lightest stau.

- $\mathrm{sgn}(\mu)$: The magnitude of μ can be computed from the condition of the correct electroweak breaking;

$$\mu^2 = -\frac{m_{Z^0}^2}{2} + \frac{1}{\tan^2\beta - 1}(m_{H_1}^2 - \tan^2\beta m_{H_2}^2), \qquad (2.25)$$

and the sign of μ is still a free parameter. The parameters μ^2 is roughly (electroweak scale)^2.

- C_{grav} is the ratio of the intrinsic SUSY-breaking parameter (F_0) to the messenger sector SUSY-breaking parameters (F). It controls the coupling to the gravitino. C_{grav} is an independent parameter, and it is set to be small enough so that the NLSP decays into the LSP promptly.

The NLSP decays only via the gravitational coupling and can have a very long-life. For a slepton NLSP:

$$c\tau_{\mathrm{NLSP}} = 0.1 \left(\frac{100\ \mathrm{GeV}}{m_{\mathrm{NLSP}}}\right)^5 \left(\frac{m_{\tilde{G}}}{2.4\ \mathrm{eV}}\right)\ \mathrm{mm}, \qquad (2.26)$$

with the gravitino mass $m_{\tilde{G}}$ controlled by C_{grav} and F_0:

$$m_{\tilde{G}} = 2.4 C_{\mathrm{grav}} \left(\frac{\sqrt{F_0}}{100\ \mathrm{TeV}}\right)^2\ \mathrm{eV}. \qquad (2.27)$$

In a tiny and near excluded region at small values of the model parameters Λ and M, the NLSP is a scalar neutrino, otherwise it is the $\tilde{\tau}_1$. Therefore, the messenger index N_m is required to be a large value in order to obtain a slepton NLSP. However, N_m cannot

be chosen arbitrarily large values due to the theoretical constraints. Fig. 2.11 shows the smallest messenger index N_m required to have a $\tilde{\tau}_1$ NLSP for $\mu > 0$ and (a) relatively light messengers $M = 2\Lambda$ and (b) heavy messengers $M = 10^{10}$ GeV as a function of $\tan\beta$ and Λ. The light grey areas at small Λ are theoretically excluded due to unstable vacua and/or non-perturbative couplings at the GUT scale; no experimental or indirect constraints were included here.

A long-lived $\tilde{\tau}_1$ is not the only SMP possibility in the GMSB. If the mixing and consequently the mass splitting in the stau sector is not too large (small $\tan\beta \lesssim 8$), the $\tilde{e}_R$ and $\tilde{\mu}_R$ may be nearly mass-degenerate (co-NLSP) with the $\tilde{\tau}_1$ and hence can simultaneously be SMPs.

In this thesis, the search for charged SMPs has been performed assuming that they are generated from GMSB processes (see Chapter 7).
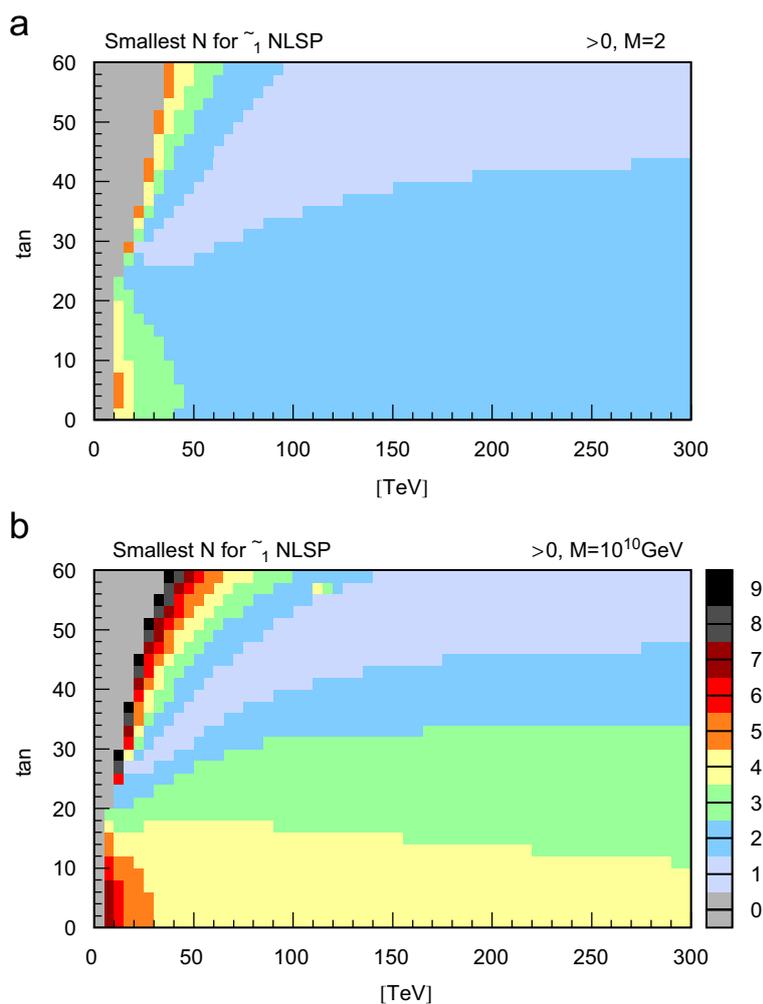

Figure 2.11: The smallest index number N_m required to obtain a $\tilde{\tau}_1$ NLSP as a function of Λ and $\tan\beta$ for (a) light messengers ($M = 2\Lambda$) and (b) heavy messengers ($M = 10^{10}$ GeV). [32]

Chapter 3

The LHC collider and the ATLAS detector

This chapter describes the LHC (Large Hadron Collider) and the ATLAS (A Toroidal LHC ApparatuS) detector. The LHC is a proton-proton collider with its design center of mass energy of 14 TeV, which is the largest in the world. Thus, the LHC can reach unexplored energy region for new physics studies. Its design luminosity is $10^{34}\mathrm{cm}^{-2}\mathrm{s}^{-1}$. Bunch crossing rate is 25 nsec, leading to a total event rate of up to 10^9 events per second. ATLAS is a general-purpose detector at the LHC, with which various physics studies, especially new particle searches, can be performed.

3.1   The LHC collider

The LHC is a synchrotron accelerator with a circumference of 27 km, where protons are accelerated to 7 TeV. Super Proton Synchrotron (SPS) is the pre-injector for the LHC and accelerates 26 GeV protons from Proton Synchrotron (PS) to 450 GeV. The beam line of the LHC is composed of accelerating cavities and super-conducting NbTi bending magnets and quadruples for the beam optics. These dipole magnets are placed along two separated beam lines and produce magnetic fields of 8.4 T strength in vertical direction. There are four collision points in the LHC, where the following detectors are placed.

1. ATLAS (A Toroidal LHC ApparatuS)

2. CMS (The Compact Muon Solenoid)

3. LHC-B

4. ALICE (A Large Ion Collider Experiment)

ATLAS and CMS are general-purpose detectors, while LHC-B is specialized for b-physics and ALICE is for heavy ion collisions (1 PeV Pb-Pb collision at the maximum energy). Locations of these detectors and proton rings are shown in Fig. 3.1.
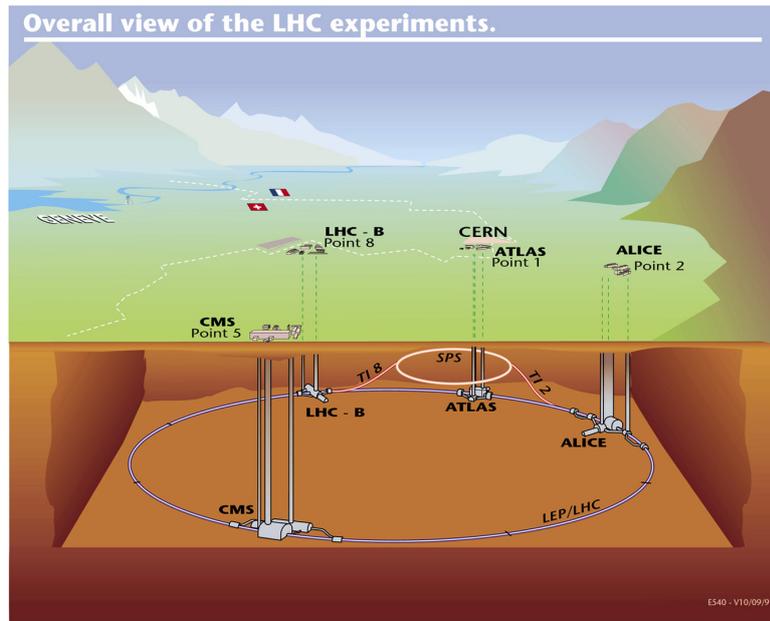
Figure 3.1: Schematic view of the CERN accelerator complex [33].

3.1.1 Luminosity

One of the important parameters of a collider is the luminosity L. For a physical process with cross section σ, the event rate $\left(\frac{dN}{dt}\right)$ is given by:

$$\frac{dN}{dt} = \sigma \times L. \tag{3.1}$$

In the case of a collider like the LHC, the luminosity is given by:

$$L = \frac{N_{p1} N_{p2} f_{\text{cross}}}{4\pi \sigma_x^* \sigma_y^*}, \tag{3.2}$$

where N_{p1} and N_{p2} are the number of protons per each bunch and f_{cross} is the bunch crossing frequency. σ_x^* and σ_y^* are transverse beam sizes of horizontal and vertical directions at the interaction point, respectively, and $\sigma_x^* \sigma_y^*$ gives the cross section of the beam. It is clear that increase of N_{p1}, N_{p2} and f_{cross} and decrease of σ_x^* and σ_y^* produce higher luminosity.

There are mainly two operation modes at the LHC; one is called "high-luminosity mode" with the design luminosity and the other is "low-luminosity mode" with a luminosity of 10^{33} cm^{-2}s^{-1}. The latter will be continued for the first 3 years. Another mode with the luminosity of 10^{31} cm^{-2}s^{-1} is also planned in the very early stage of the LHC. Parameters of the LHC for the high-luminosity mode are listed in Table 3.1.

Main ring	26658.87 m	Injector energy	450 GeV
Proton energy	7.0 TeV	Number of protons	1.1×10^{11}/bunch
Bunch Length	77 mm	Bunch interval	24.95 nsec
beam radius	15.9 μm	beam crossing angle	300 μrad
Luminosity Lifetime	10 hours		

Table 3.1: Parameters of LHC [34].

3.1.2   Physics run in 2010

The LHC collider started proton-proton collisions with 7 TeV center-of-mass energy on 30 March 2010. The number of bunch was one in the LHC accelerator ring. The luminosity was 10^{27} cm^{-2}sec^{-1}.

The goal of physics run in 2010 was to perform stable collisions with luminosity of 10^{32} cm^{-2}sec^{-1}. From Eq. 3.2, it is necessary to increase the number of bunch in the accelerator ring and narrow the size of proton beam in order to increase luminosity. In August 2010, the luminosity of 10^{31} cm^{-2}sec^{-1} was achieved by increasing the bunch number to fifty and narrowing the proton beam size. Finally, the number of bunch was 368 and the luminosity of about 2×10^{32} cm^{-2}sec^{-1} was achieved at the end of October (Fig. 3.2-(a)). ATLAS has collected collision data, which corresponds to an integrated luminosity of 45.0 pb^{-1} (Fig. 3.2-(b)).

Physics run will re-start with luminosity of 10^{32} cm^{-2}sec^{-1} in 2011. The total integrated luminosity of more than 1 fb^{-1} is expected to be achieved in the end of 2011.
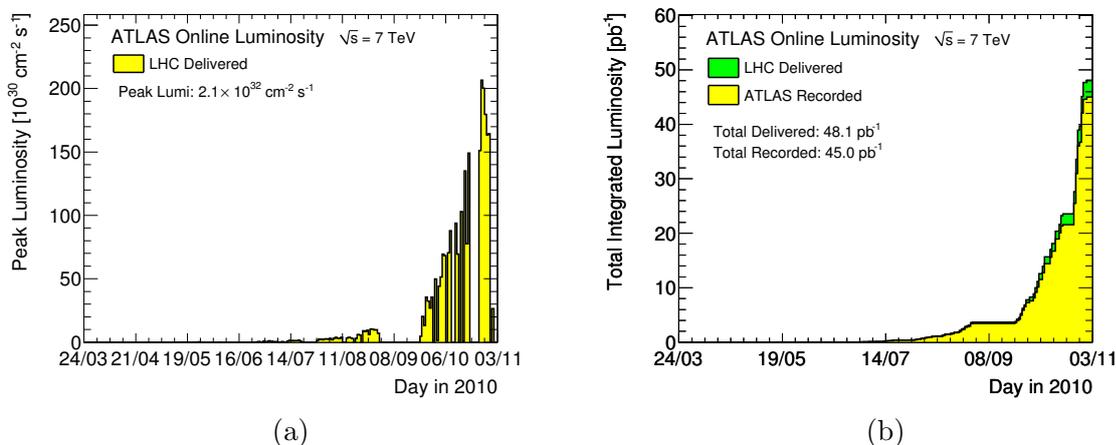

Figure 3.2: (a); The maximum instantaneous luminosity versus day delivered to ATLAS, (b); Cumulative luminosity versus day delivered to (green), and recorded by ATLAS (yellow) during stable beams and for proton-proton collisions at 7 TeV centre-of-mass energy [35].

3.1.3   Particle production rates

As a proton is a composite particle, the center of mass energy of 14 TeV is distributed to
each elementary particle. At these energies, not only the valence-quarks but also the gluons
holding them together can interact and additionally, a whole sea of quark-antiquark pairs
that are allowed a fleeting existence under the law of quantum mechanics, too. Therefore,
only mass states up to a few TeV can be created. Figure 3.3 shows the prediction of
particle-production cross section for the particles of most interest at the LHC together
with production rates at the high luminosity mode. One at the Tevatron, which is the
proton-antiproton collider at Fermilab, is also shown for a comparison. It can be seen that
the total cross section is more than ten orders of magnitude larger than that of the Higgs
production. Therefore, detectors must have capability to handle such an enormous total
event rate and distinguish the signals of interest from other events such as proton-proton
inelastic events and minimum bias events (QCD events), or backgrounds such as beam halo
events and beam gas events.

3.2   The ATLAS detector

Figure 3.4 shows a 3D view of the whole ATLAS Detector, which is characterized by
its magnet configuration as follows: a superconducting solenoid is installed around the
Inner Detector and large superconducting air-core toroids consisting of independent coils
is arranged with an eight-fold symmetry outside the calorimetries. ATLAS is 22 m in
height and 44 m in length and its weight is about 7000 tons.

For physics studies at the LHC, we need to know what kind of particles are produced,
by using combinations of various detectors. Particles' behavior in each detector is shown
in Fig. 3.5. The produced particles can be distinguished by their differences of interaction
with matters. For example, charged particles can be detected by a tracking detector and,
by generating a magnetic field and detecting their trajectories there, their momenta can be
measured. Particles with electric charge and photons can be detected by an electromagnetic
calorimetry and electrons and photons can be identified there. Strongly interacting particles
such as pions, neutrons and protons can be detected by a hadron calorimetry. Since muons
deposit little energy in the calorimetry and have a long life time, they reach outside of
the calorimetry and are detected by the muon spectrometer. Details of each detector are
explained later.

For not only particle identification but also event selection, combined information from
the detectors is very useful. For example, b quarks can be identified by the following way.
While t quarks immediately decay after its production, b hadrons have relatively long life
time and fly for a moment. Then they decay far enough away from the primary vertex
and make the secondary vertices. Therefore, b hadrons can be identified by finding the
secondary vertices.

To exploit the full physics potential of the LHC, the ATLAS detector was designed to
fulfill the following requirements;

- large acceptance and maximum angular coverage for hermetic jet and missing E_T
  calorimetry.

- very good electromagnetic calorimetry for electron and photon measurements;
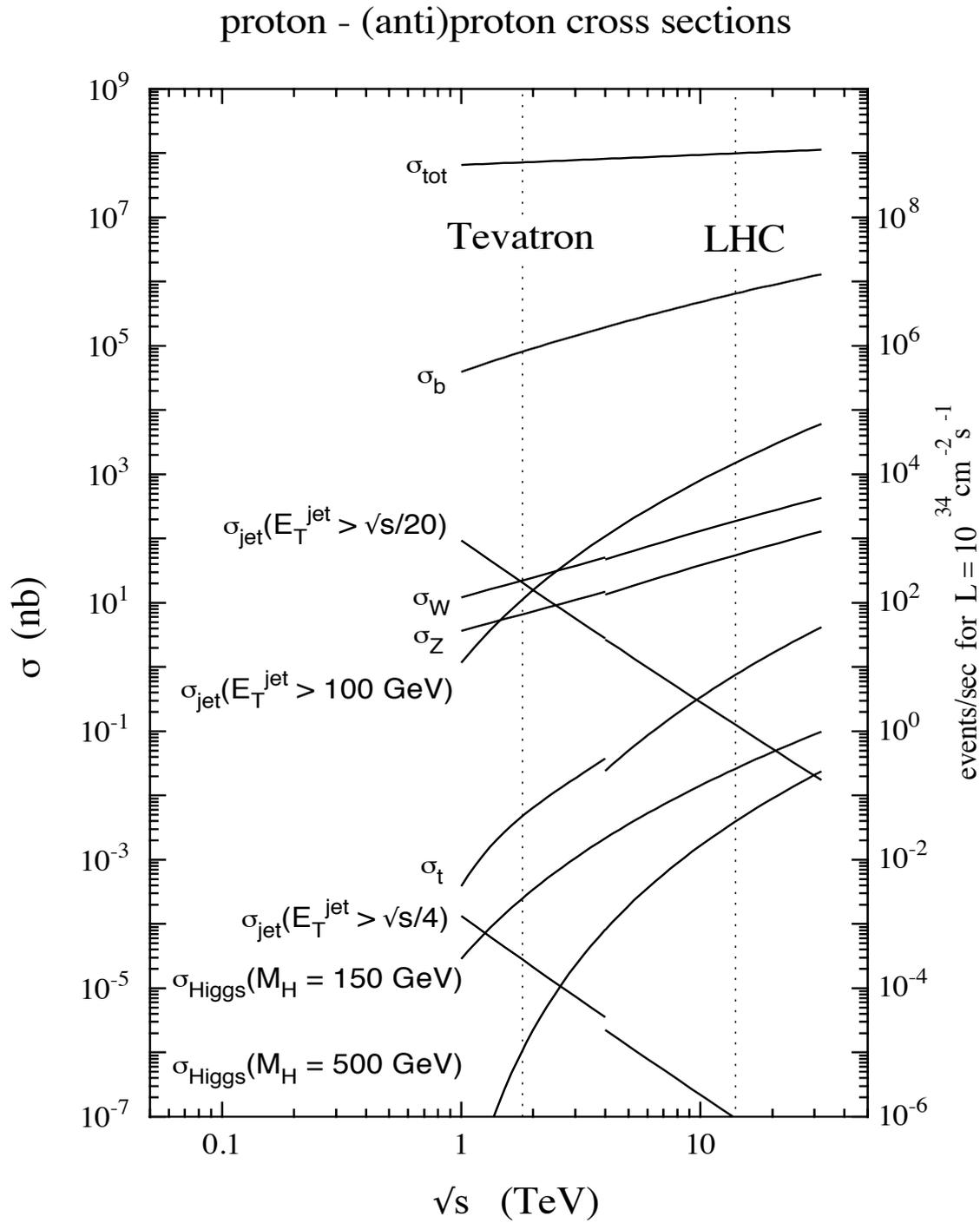
Figure 3.3: Predicted cross section of proton-proton interaction as a function of interaction energy as a function of center-of-mass energy. The energy at the Tevatron, Fermilab as well as for the LHC are indicated [40].
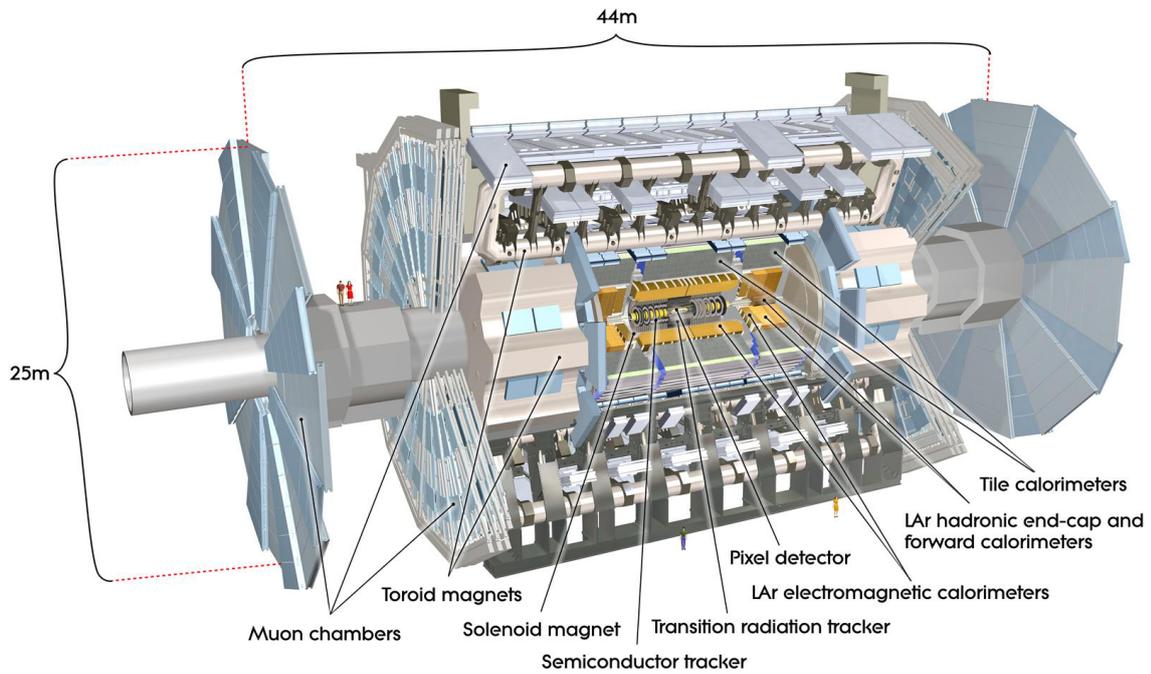
Figure 3.4: ATLAS Detector [33]
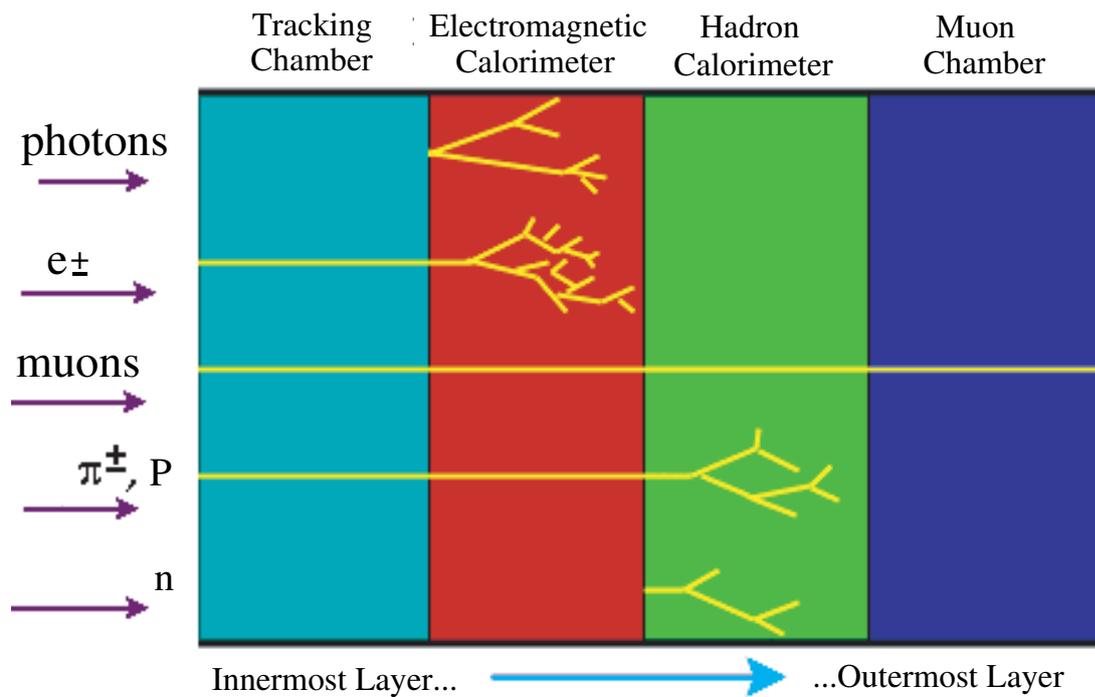
Figure 3.5: Particles' behavior in each detector

- very good tracking efficiency for lepton-momentum measurements, secondary vertex findings and enhancement of the accuracy of electron and photon identification. Here, tracking in jets have to be done;

- stand-alone muon-momentum measurements at high luminosity;

- very low-p_T trigger and reconstruction capability at low luminosity.

Definition of coordinates

The coordinates are defined as follows. The beam line is defined as z-axis whose positive direction points in the direction of LHC-B. The plane transverse to the z-axis is defined as the x-y plane. The positive x-axis is pointing from the interaction point to the center of the LHC ring and the positive y-axis is pointing to upwards.

While the Cartesian coordinate system is defined, cylindrical coordinates are often used because of the detectors being cylindrically symmetric. In this case, the z-axis is the same as for the Cartesian coordinate system. The azimuthal angle ϕ is defined as the angle from positive x-axis in x-y plane with the $-\pi$ to π range. The polar angle θ is also defined as the angle from the positive z-axis, and then, pseudo rapidity η is defined as $\eta = -\ln\tan\frac{\theta}{2}$. For hadron colliders, η is often used because the particle distribution in pseudo rapidity $(\frac{\Delta N}{\Delta \eta})$ is basically flat in low p_T and invariant under the Lorentz transformation.

3.2.1   Inner Detector

The ATLAS Inner Detector is contained within a cylinder with a length of 7 m and a radius of 1.15 m, in a solenoidal magnetic field of 2 T. Momentum and vertex measurements are achieved with a combination of discrete high-resolution semiconductor pixel and strip detectors in the inner part of the tracking volume. Electron identification is performed by continuous straw-tube tracking detectors with transition radiation capability in the outer part. Overall inner detector layout is shown in Fig. 3.6 and details for each detector are mentioned below.

Silicon-pixel vertex-detector (Pixel)

ATLAS Pixel Detector provides a very high granularity and high precision set of measurements at as close to the interaction point as possible. A Pixel sensor is a 16.4×60.8 mm^2 wafer of silicon with 46,080 pixels, 50×400 μm^2 each. Each sensor is read out by 16 chips, each serving for an array of 18 by 160 pixels. The 80 million pixels cover an area of 1.7 m^2. The system consists of three barrels at average radii of $\sim$ 5, 9 and 12 cm (1456 modules) respectively, and three discs on each side between radii of 9 and 15 cm (288 modules) as shown in Fig. 3.7. The modules are overlapped on the support structure to give hermetic coverage. The thickness of each layer is expected to be about 2.5 % of a radiation length at normal incidence. Typically three pixel layers are crossed by each track.

Semi Conductor Tracker (SCT)

The SCT system is designed to provide four precision measurements per track in the intermediate radial range, contributing to the measurement of momentum, impact parameter
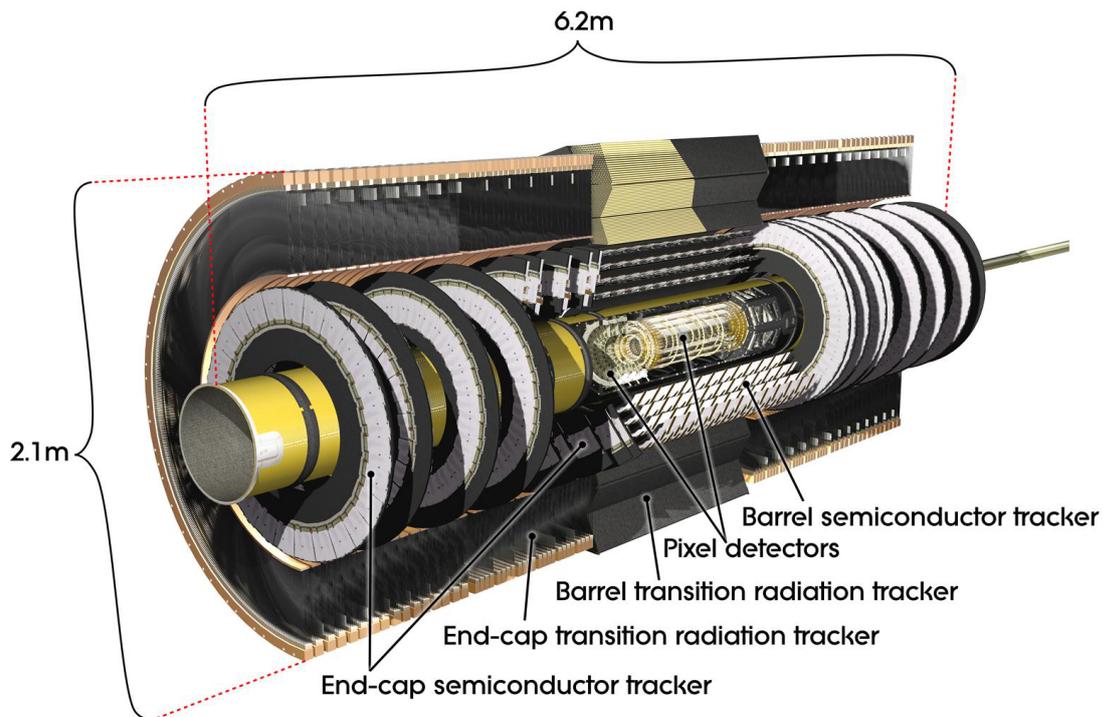
Figure 3.6: 3D overall inner detector layout [33].

and vertex position, as well as providing good pattern recognition by the use of high granularity. The system is an order of magnitude larger in surface area than previous generations of silicon microstrip detectors, and, in addition, must face radiation levels which will alter the fundamental characteristics of the silicon wafers themselves.

Figure 3.8 shows view of the SCT system, which covers $|\eta| < 2.5$. The barrel SCT uses four layers of silicon microstrip detectors to provide precision points in the r-ϕ and z coordinates. Each silicon detector is 6.36×6.40 cm^2 with 768 readout strips each with 80 μm pitch. Each module consists of four detectors. On each side of the module, two detectors are wire-bonded together to form 12.8 cm long strips. Two such detector pairs are then glued together back-to-back at a 40 mrad angle, separated by a heat transport plate, and the electronics is mounted above the detectors on a hybrid. The readout chain consists of a front-end amplifier and discriminator, followed by a binary pipeline which stores the hits above threshold until the first level trigger decision. The forward modules are very similar in construction but use tapered strips, with one set aligned radially. Forward modules are made with both $\sim$ 12 and 7 cm lengths. The detector contains 61 m^2 of silicon detectors with 6.2 million readout channels. The spatial resolution is 16 μm in r-ϕ and 580 μm in z. Tracks can be distinguished if separated by more than $\sim$200 μm.

Figure 3.7: Pixel Detector [33]
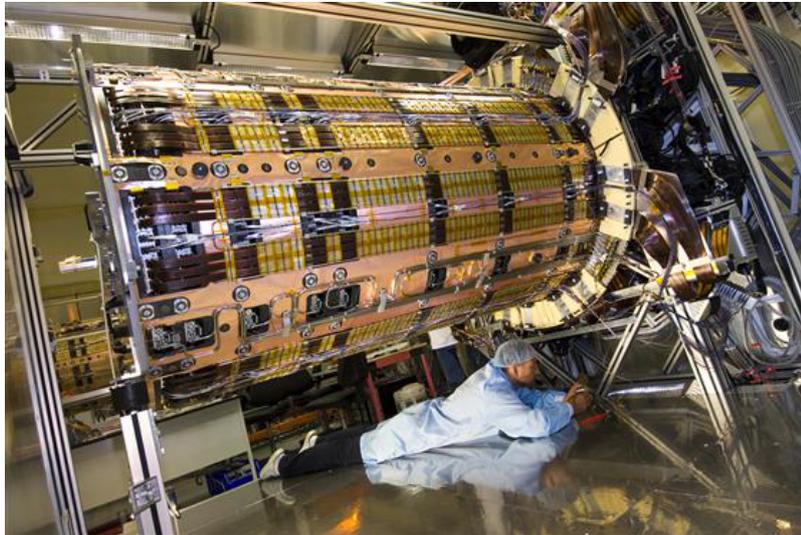
Figure 3.8: SCT [33]

Transition Radiation Tracker (TRT)

TRT, whose photo is shown in Fig. 3.9, is based on the use of straw detectors, or tubes, which can operate at the expected high rates due to their small diameter and the isolation of the sensitive wires within individual gas volumes. Electron identification capability is added by employing Xenon gas to detect transition radiation photons created in a radiator between the straws. The nonflammable gas mixture is Xe (70%)/CO_2 (27%)/O_2 (3%) with a total volume. The barrel section is built of individual modules covering the radial range

from 56 cm to 107 cm. Each end-cap consists of 18 wheels. Each channel provides a drift time measurement that gives a spatial resolution of 170 μm per straw.
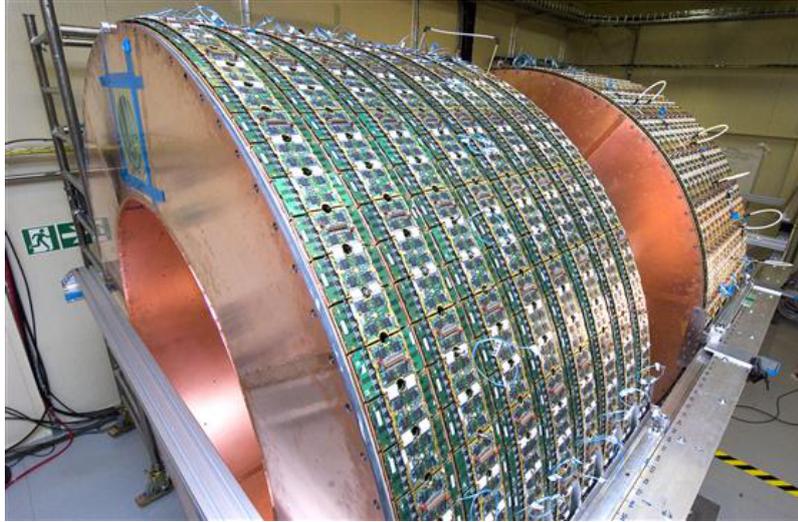
Figure 3.9: TRT [33]

3.2.2 Calorimeters

In contrast to other detectors, such as magnetic spectrometers, intrinsic resolution of calorimeters improves with energy, which makes themselves very suitable detectors at high-energy machines.

The task of the calorimeters at hadron colliders are the following:

- accurate measurement of the energy and position of electrons and photons;

- measurement of the energy and direction of jets and measurement of the missing transverse energy ($\not{E}_T$) of the event;

- particle identification, for instance separation of electrons and photons from hadrons and jets, and of tau hadronic decays from jets;

- event selection at the trigger level.

The overall detector layout is shown in Fig. 3.10. Highly granular liquid-argon (LAr) electromagnetic sampling calorimetry, with an emphasis on energy and position resolution, covers the pseudorapidity range $|\eta| < 3.2$. At larger rapidities, higher radiation resistance is needed and the intrinsically-hard LAr technology is used. In the end-cap, the LAr technology is also used for the hadronic calorimeters. There are special LAr forward calorimeters which extend the pseudorapidity coverage to $|\eta| = 4.9$. The LAr calorimetry is contained in a cylinder with an outer radius of 2.25 m and extends longitudinally to ± 6.65 m along the beam axis. The bulk of the hadronic calorimetry is provided by scintillator-tile calorimeter, which is separated into a large barrel and two smaller extended barrel cylinders, one on
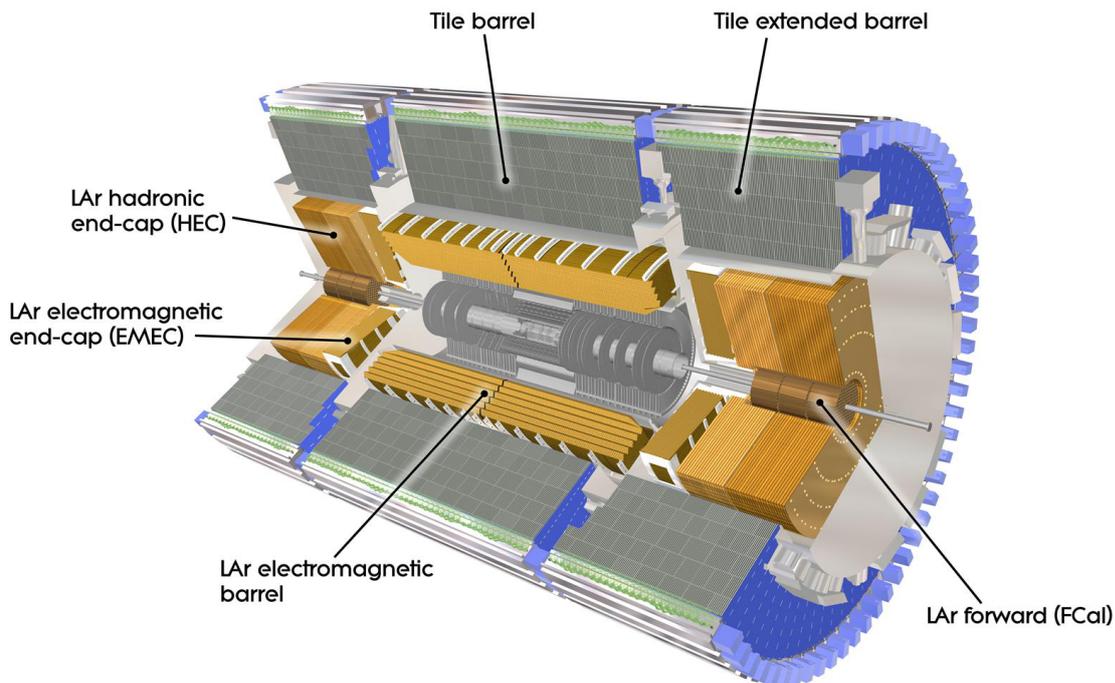
Figure 3.10: 3D overall calorimeter layout [33].

each side of the barrel. The outer radius of the scintillator-tile calorimeter is 4.25 m and its half length is 6.10 m. The overall calorimeter system provides good jet and missing E_T performance of the detector.

Electromagnetic Calorimeter

The electromagnetic calorimeter is a sampling calorimeter which uses lead as absorber and liquid argon as sampling material. It covers the rapidity range up to $|\eta| < 3.2$. Its accordion geometry (shown in Fig. 3.11) provides a complete ϕ coverage without azimuthal cracks. The system is divided into a barrel ($|\eta| < 1.475$) and two end-caps ($1.375 < |\eta| < 3.2$). The barrel calorimeter consists of two identical half-barrels, separated by a small gap (6 mm) at $\eta = 0$. Each end-cap calorimeter is mechanically divided into two coaxial wheels: an outer wheel covering the region $1.375 < |\eta| < 2.5$ and an inner wheel covering the region $2.5 < |\eta| < 3.2$. The lead thickness in the absorber plates has been chosen as a function of rapidity as shown in Table 3.2, so as to optimize the calorimeter performance in terms of energy resolution. The LAr gap has a constant thickness of 2.1 mm in the barrel. In the end-cap, the shape of the Kapton electrodes and lead converter plates is more complicated, since the amplitude of the accordion waves increases with radius. The absorbers have constant thickness, and therefore the LAr gap also increases with radius. The total thickness of the electromagnetic calorimeter, which is shown in Fig. 3.12 as a function of η, is above 24 radiation lengths in the barrel and above 26 radiation lengths in

the end-caps. The typically achieved energy resolution is:

$$\frac{\Delta E}{E} = \frac{11.5\%}{\sqrt{E}} \oplus 0.5\%, \tag{3.3}$$

and the resolution of the polar direction of a shower is:

$$\Delta\theta = \frac{50 \text{ mrad}}{\sqrt{E}}, \tag{3.4}$$

where E is represented in GeV.
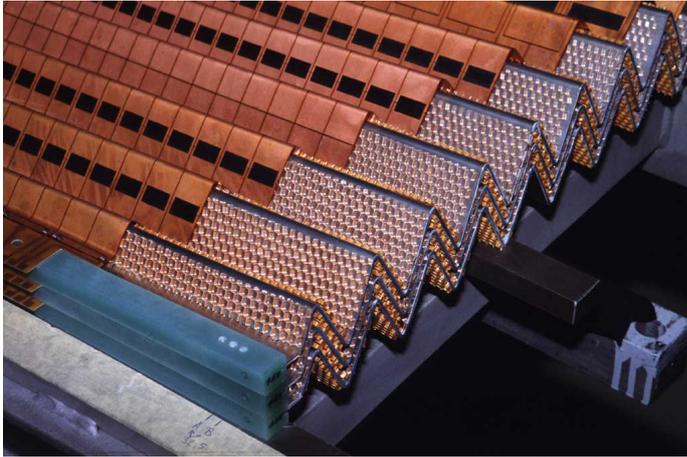
Figure 3.11: The accordion geometry of the LAr electromagnetic calorimeter [33].
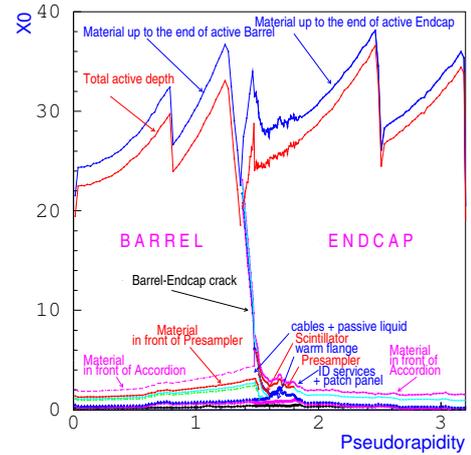
Figure 3.12: Total thickness in radiation lengths of the ATLAS EM calorimeter as a function of η [37].

	η range	Pb thickness	Gap thickness
Barrel	$|\eta| < 0.8$	1.5 mm	2.1 mm
	$0.8 < |\eta| < 1.475$	1.1 mm	2.1 mm
End-cap	$1.375 < |\eta| < 2.5$	1.7 mm	2.8-0.9 mm
	$2.5 < |\eta| < 3.2$	2.2 mm	3.1-1.8 mm

Table 3.2: Lead thickness in the absorber plates and LAr gap thickness in the EM calorimeter as a funcfion of η.

Hadronic Calorimeter

The ATLAS hadronic calorimetry covers the range $|\eta| < 5$ using different techniques and devices as best suited for the different requirements and radiation environment. The system is divided into three subdetectors.

In the range $|\eta| < 1.6$, the iron-scintillating-tile technique (its schematic is illustrated in Fig. 3.13) is used for the barrel and extended barrel Tile calorimeters and, for partially instrumenting the crack between them, with the Intermediate Tile calorimeter. This gap provides space for cables and services from the innermost detectors. The tiles are placed perpendicular to the colliding beams and are staggered in depth, and the structure is periodic along z. The tiles are 3 mm thick and the total thickness of the iron plates in one period is 14 mm. Both sides of the scintillating tiles are read out by wavelength shifting (WLS) fibers into two separate Photo Multiplier Tubes (PMT). The resulting granularity of the detector is $\Delta\eta \times \Delta\phi = 0.1 \times 0.1$. It has a longitudinal segmentation of three samplings.
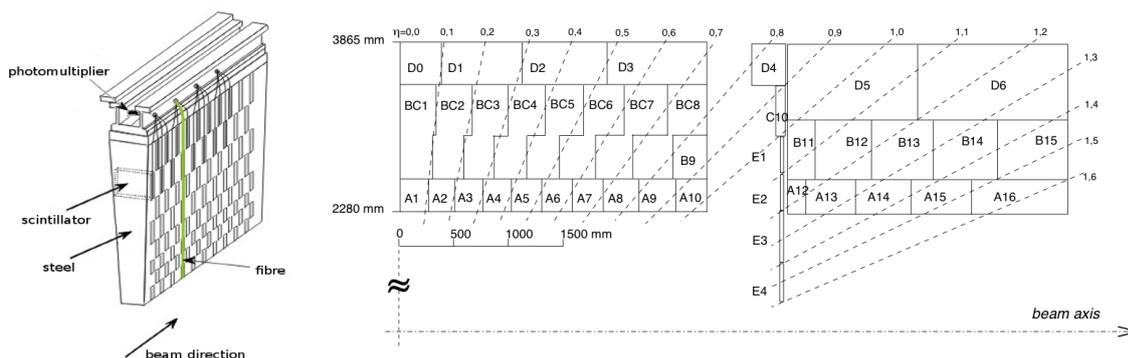

Figure 3.13: Left: a schematic display of a module, showing the passive and active material, and the optical readout system. Right: a schematic display of the cell structure in the central and extended barrel [37].

In the range $1.5 < |\eta| < 4.9$, the LAr calorimetry takes over: the end-cap hadronic calorimeter extends to $|\eta| < 3.2$, while the range $3.1 < |\eta| < 4.9$ is covered by the high-density forward calorimeter. Each hadronic end-cap calorimeter consists of two, equal diameter, independent wheels. The first wheel is built out of 25 mm copper plates, while the second one uses 50 mm plates. The end-cap hadronic calorimeter has a $\Delta\eta \times \Delta\phi = 0.1 \times 0.1$ segmentation in the range up to $|\eta| < 2.5$ and a segmentation of $\Delta\eta \times \Delta\phi = 0.2 \times 0.2$ in the range up to $2.5 < |\eta| < 3.2$. The forward calorimeter consists of three sections. The first is made out of copper, while the others are made out of tungsten. In each of them, the calorimeter consists of a metal matrix with regularly spaced longitudinal channels filled with rods. The sensitive medium is LAr which fills the gap between the rod and the matrix. Both the hadronic end-cap and forward calorimeters are integrated in the same cryostat housing as the electromagnetic end-cap calorimeters.

The total thickness is 11 interaction lengths at $\eta = 0$, including 1.5 interaction lengths of the outer support. It is sufficient to reduce the punch-through below the irreducible level of prompt or decay muons. The thickness of active calorimeter being close to 10 interaction lengths is also adequate to provide good performance on resolution for high

energy jets. Over the full η range, four longitudinal samples are available. The average jet energy resolution is:

$$\frac{\Delta E}{E} = \frac{50\%}{\sqrt{E}} \oplus 3\%, \tag{3.5}$$

where E is represented in GeV.

3.2.3   Muon Spectrometer

While muons interact weakly and electromagnetically like electrons, they can reach outside of the calorimeter because the muon mass is about 200 times heavier than the electron mass. Therefore, the muon spectrometer is placed at the outermost of the detectors.

High-momentum final-state muons are one of the most promising and robust signatures of physics at the LHC. To exploit this potential, the ATLAS detector is equipped with a high-resolution muon spectrometer with stand-alone triggering and momentum measurement capability over a wide range of transverse momentum (p_T), pseudorapidity (η) and azimuthal angle (ϕ). Muon measurement at ATLAS is based on the magnetic deflection measurement of muon tracks in a system of the large superconducting air-core toroids instrumented with tracking chambers. Figure 3.14 shows the 3D overall layout of the muon spectrometer and Figure 3.15 is the sectional view of a quarter of the system. There can be seen four detectors, two of them, Thin Gap Chambers (TGC) and Resistive Plate Chambers (RPC) are trigger chambers and the others, Monitored Drift Tube chambers (MDT) and Cathode Strip Chambers (CSC) are for precision measurement. In the range $|\eta| < 1.0$, bending fields are provided by a large barrel magnet consisting of eight coils surrounding the hadron calorimeter. For $1.4 < |\eta| < 2.7$, muon tracks are bent in two smaller end-cap magnets inserted into both ends of the barrel toroid. In the interval $1.0 < |\eta| < 1.4$, magnetic deflection is provided by a combination of barrel and end-cap fields. This magnet configuration provides a field that is mostly orthogonal to the muon trajectories, while minimizing the degradation of resolution due to multiple scattering.
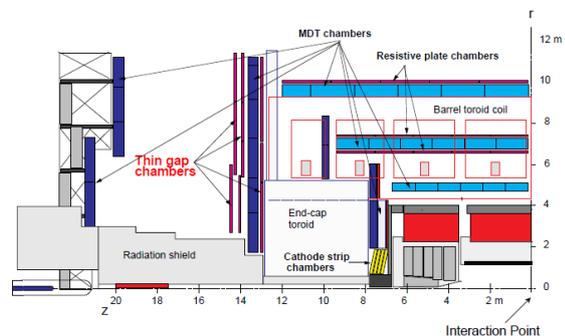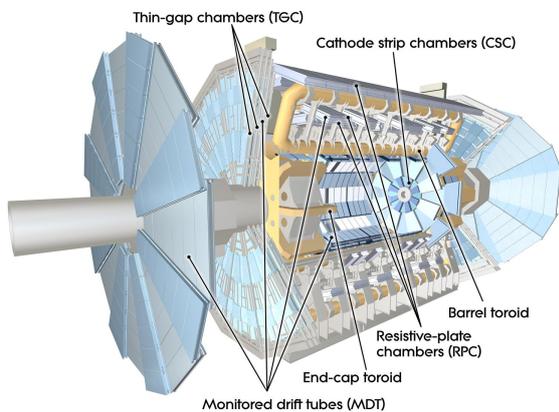

Figure 3.14: 3D muon spectrometer layout [33].

Figure 3.15: A sectional plan of the muon spectrometer layout [38].

Physics requirements

While high-p_T muons are expected to be produced from new particle production, physics of CP violation through B meson decays can be studied by requiring low-p_T muons. Therefore, performance of the spectrometer should be optimized on the basis of selected benchmark processes. Important parameters to be optimized for maximum physics reach are:

- Resolution: momentum and mass resolutions at the level of 1 % should be achieved for muons with $p_T > 6$ GeV against high background levels;

- Second-coordinate measurement: a measurement of muon tracks in the non-bending projections with a spatial resolution of about 1cm is required for the track reconstruction and reliable momentum determination;

- Rapidity coverage of track reconstruction: all physics channels in particular rare high-mass processes need a pseudo-rapidity coverage up to $|\eta| \sim 3$ and good hermeticity;

- Trigger selectivity: a transverse momentum threshold of around 20 GeV is adequate for high-mass states, which is focused on physics at the LHC at nominal luminosity. Lower thresholds of 6 GeV are also required for CP violation in the B sector;

- Trigger coverage: adequate trigger efficiencies can be obtained with η coverage smaller than that of the precision chambers. The actual requirements are mostly determined by processes at opposite ends of the LHC mass scale: the need for good acceptance for rare high-mass Higgs particles, and the need for very high statistics to study small rate asymmetries due to CP violation in the B sector. Trigger coverage of $|\eta| < 2.4$ is found to be sufficient;

- Bunch-crossing identification: the LHC bunch-crossing interval of 25 nsec sets the scale for the required time resolution of the first-level trigger system;

Magnet system

The magnet system consists of three air-core superconducting toroids designed to produce a large-volume magnetic field covering the rapidity range $0 < |\eta| < 2.7$, with an open structure that minimizes the contribution of multiple scattering to the momentum resolution. Geometry of the magnet is shown in Fig. 3.16. The barrel toroid extends over a length of 25 m, with an inner bore of 9.4 m and an outer diameter of 20.1 m. The two end-cap toroids are inserted in the barrel at each end. They have a length of 5.0 m, an inner bore of 1.65 m and an outer diameter of 10.7 m. Each toroid consists of eight flat coils assembled radially and symmetrically around the beam axis. The end-cap toroid coils are rotated in azimuth by an angle of 22.5 degree with respect to the barrel toroid coils to provide for radial overlap, and to optimize the bending power in the transition region between the two toroids. The barrel toroid coils are contained in individual cryostats and are held rigidly together by means of eight rings of voussoirs and struts that contain the gravitational and magnetic forces. The eight coils of each end-cap toroid are assembled in a single large cryostat. The magnetic field provides for typical bending powers of 3 Tm in the barrel and 6 Tm in the end-cap regions. Owing to the finite number of coils, the field configuration is not perfectly toroidal and presents a regularly rippled profile (see Fig. 3.17). These effects

are most visible in the transition region between the barrel toroids and the end-cap toroids, where there exist significant radial field components, as well as small regions with degraded momentum resolution. The bending power is shown in Fig. 3.18.

(a)   (b)
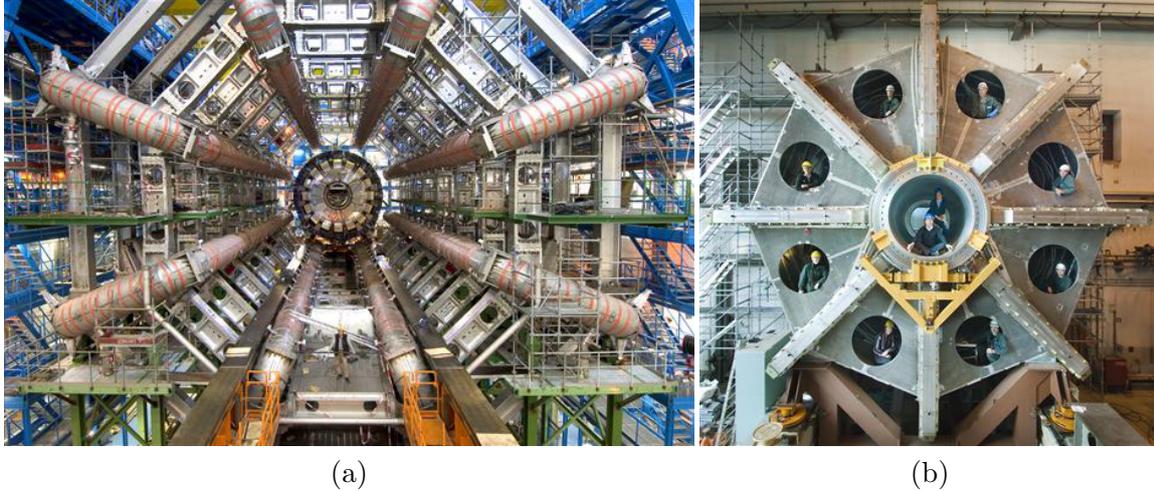
Figure 3.16: The toroidal magnets for the barrel (a) and the endcap (b) regions [33].
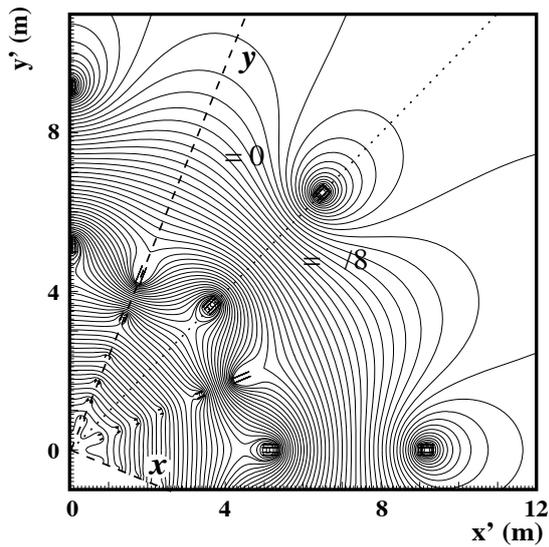
Figure 3.17: Magnetic field map in the transition region between the barrel and the endcap. The field lines in the transverse plane are shown. The coordinate system of the magnetic field is rotated by $\frac{\pi}{8}$ with respect to the ATLAS coordinate system[38].
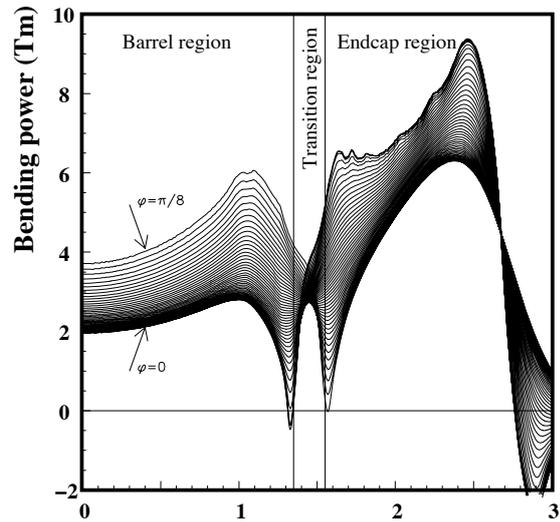
Figure 3.18: Toroid bending power $\int Bdl$ of the azimuthal field component, integrated between the inner and outer muon station as a function of η[38].

Momentum measurement

The momenta of charged particles can be calculated by detecting their trajectories in the magnetic field. Assuming that a track is detected at three equally-spaced points, the sagitta s of the circular orbit is defined as shown in Fig. 3.19 and calculated as

$$s = R\left(1 - \cos\frac{\alpha}{2}\right) \sim \frac{R\alpha^2}{8} \ (\alpha \ll 1). \quad (3.6)$$

At the same time, the momentum P of a charged particle in magnetic field B [T] is calculated as

$$P = 0.3BR, \quad (3.7)$$

where R [m] is the measured radius of the orbit. Then, concerning α to be

$$\alpha = 0.3\frac{BL}{P}, \quad (3.8)$$

the sagitta is represented as


Figure 3.19: Measurement of sagitta.

$$s = 0.3\frac{BL^2}{8P}. \quad (3.9)$$

Thus, the momentum can be obtained from the sagitta.

Muon precision chambers

Monitored Drift Tubes (MDT) cover 99.5 % of the area and Cathode Strip Chambers (CSC) cover the remaining forward area near the beam pipe where particle fluxes are high. Although this area is physically small, it covers a large range in pseudorapidity ($2 < |\eta| < 2.7$). The precision chambers measure the track coordinates in the bending plane with high precision. For the MDTs, no information on the non-bending coordinate exists. The CSCs, however, do measure both quantities.


Figure 3.20: The ATLAS muon precision chambers. MDT big wheel (left), CSC small wheel (right) [33].

MDT (Monitored Drift Tube)

The Monitored Drift Tube Chambers perform the precision coordinate measurement in the bending direction of the air-core toroidal magnet and provide the muon momentum measurement. They cover enough area needed for a good momentum determination of the muons with $|\eta| < 2.7$.

The basic detection element is a cylindrical aluminum drift tube of 30 mm diameter and a Tungsten-Rhenium central wire of 50 μm diameter. It is operated with nonflammable gas composed of Ar(93%) and CO_2(7%) at 3 bar absolute pressure for reduced diffusion and ionization fluctuation. The wire is at a potential of 3080 V. These operating conditions are optimum with regard to the requirements of linearity in the drift space time relation, a small occupation time (about 700 ns maximum drift time) and a small Lorentz angle of about 9.3 degree. The amplification factor is set to be very low, 2×10^4, to minimize the aging effect.

The operating parameters are summarized in Table 3.3. The relation between the drift time and the drift distance is shown in Fig. 3.21 without a magnetic field. In the magnetic field the wires are oriented essentially parallel to the field lines. The magnetic effect on the drift distance-drift time (r-t) relation gives a small deviation away from the radial drift (see Fig. 3.22) and a small reduction of the apparent drift velocity. The size of the equivalent coordinate shift depends on the gas and the fields.

The precise r-t relation is obtained by fitting tracks to the six measured drift times of a chamber in an 'auto calibration' procedure on the basis of the staggered wire arrangement. Corrections to the coordinates of an individual tube are applied beforehand. The drift signal is processed with a current-sensitive amplifier followed by a shaper and a discriminator set at a threshold which corresponds to 20 electrons when the avalanche amplification is 2×10^4. With these parameters the average single tube resolution is 80 μm.
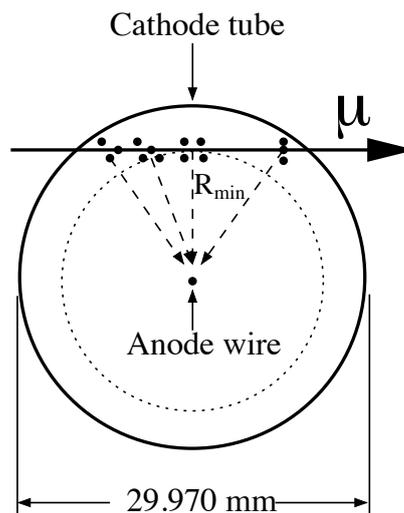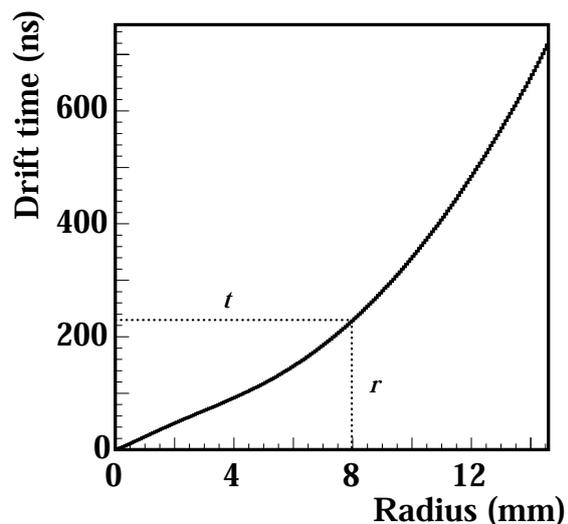

Figure 3.21: Relation between measured drift time and corresponding drift length in the absence of a magnetic field [36].

Figure 3.22: Drift tube operation in a magnetic field with curved drift pass [36].
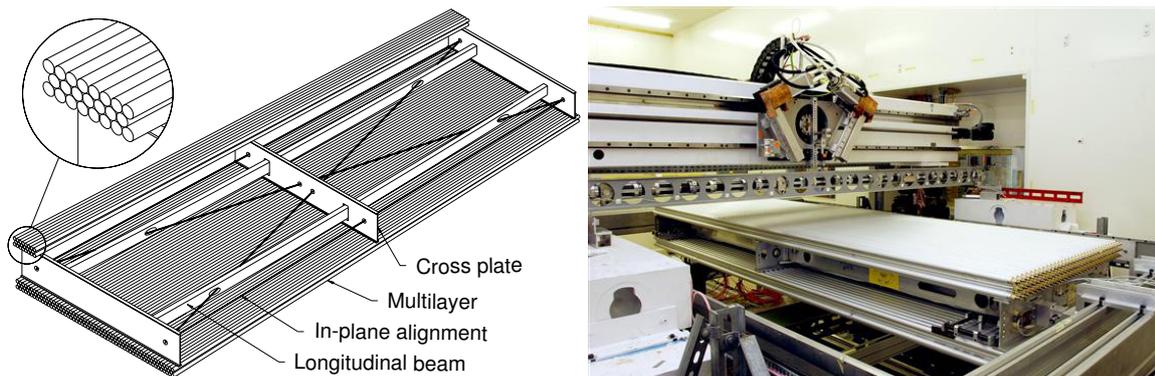
Figure 3.23: Schematic view of the MDT chamber [33][36].

An MDT Chamber is an assembly of six parallel layers of drift tubes on a support frame, and three layers on each side, see Fig. 3.23. The tubes with their diameter of 30 mm are closely spaced so that each 'triple layer' or 'multilayer' has a thickness of about 82 mm. By registering the drift times of the ionized electrons in the gas, one determines six coordinates of a typical track in the plane of the layer and in the direction across the tubes. This results in a measurement of effectively one coordinate with 40 μm precision and one angle with 3×10^{-4} precision.

To obtain such resolution with a light weight construction, the chambers are assembled on their support or spacer frame using precision mechanics during production. Their deformations are monitored by built-in optical systems once they have left the flat granite table on which they have been assembled. This explains the 'Monitored' of the MDTs.

The physical reference for the coordinate measurement is the wire position. It is determined by the two anchor points and by the gravitational sag of the wire in the presence of an electric field. For a determination of the momentum of a muon track in the spectrometer magnet, the sagitta, explained above, is used with the measured track coordinates of typically three MDT chambers. This requires the relative chamber positions to be known with a precision better than the achievable measurement accuracy of one chamber. The achievable accuracy is to be 30 μm, which gives significant contribution to the precision at very high-p_T. The stand-alone muon momentum resolution of the spectrometer is shown in Fig. 3.24 for the barrel part, and in Fig. 3.25 for the end-cap part. The different contributions to the resolution are indicated: multiple scattering, relative chamber alignment uncertainties, the drift tube measurement uncertainty, as well as the energy loss fluctuations in the calorimeter.

CSC (Cathode Strip Chamber)

MDTs well satisfy the requirements for the precision measurement of muons in ATLAS. However, their relatively large diameter and high operating pressure make themselves unsuitable for use in areas where high (> 200 Hz/cm^2) counting rates are expected. Such high background rates are encountered in the first muon measuring station at $|\eta| > 2.0$. In this region, CSCs are used and covering up to $|\eta| < 2.7$. Their operation is considered safe up to counting rates of about 1000 Hz/cm^2. They are multiwire proportional cham-

Parameter	Value
Tube material	Al
Outer tube diameter	29.970 mm
Tube wall thickness	0.4 mm
Wire material	gold-plated W (97%)/Re (3%)
Wire diameter	50 μm
Gas mixture	Ar (93%)/CO_2 (7%)
Gas gain	2×10^4
Wire potential	3080 V
Maximum drift time	$\sim$700 ns
Average drift velocity	30 μm/ns
Effective threshold	20th electron
Average resolution per tube	$\sim$80 μm

Table 3.3: Summary of the operating parameters of MDT chambers[39].
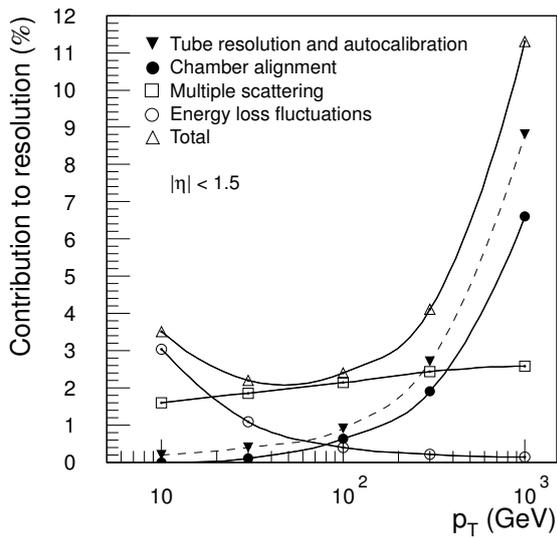
Figure 3.24: $\Delta p_T/p_T$ as a function of p_T for muons reconstructed in the barrel region $\eta < 1.5$ [36].
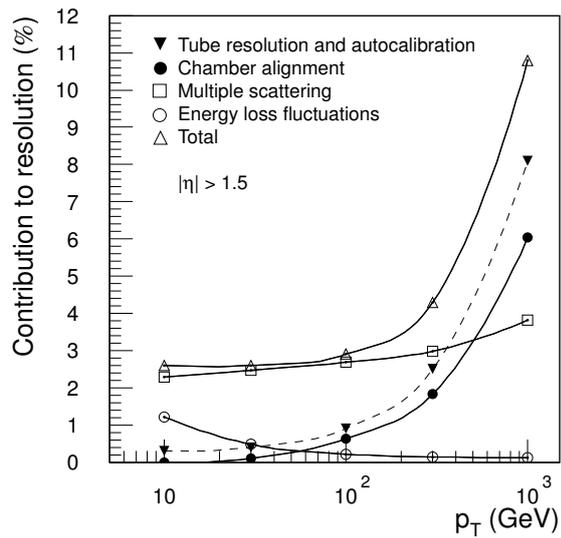
Figure 3.25: $\Delta p_T/p_T$ as a function of p_T for muons reconstructed in the end-cap region $\eta > 1.5$ [36].

bers with a cathode strip readout providing the required spatial resolution of $\sim 60\ \mu$m by charge interpolation. The schematic view of CSC is shown in Fig. 3.26 and the basic characteristics of the CSCs are summarized below:

- Excellent single layer track resolution; a sigma of $\sim 60\ \mu$m has been measured;

- Good two-track resolution; nominal single-track resolution is achieved for each of a pair of tracks separated in the bend direction by more than 5 mm corresponding to one-strip width;

- Electron drift time less than 40 ns resulting in a time resolution of 7 ns. By detecting the earliest arrival from four or more of the eight layers, the resolutions of 3.5 ns have been measured in a test beam providing a fully efficient bunch-crossing identification;

- Low neutron sensitivity; because of the small gas volume and the absence of hydrogen in the operating gas (Ar (80%)/CO_2 (20%) mixture), the measured neutron sensitivity is less than 10^{-4}. The sensitivity to photons was also measured and found to be of the order of 1 %.

- The transverse coordinate is derived by reading orthogonal strips on the second cathode of the chamber.

The operating parameters of the CSC are shown in Table 3.4.
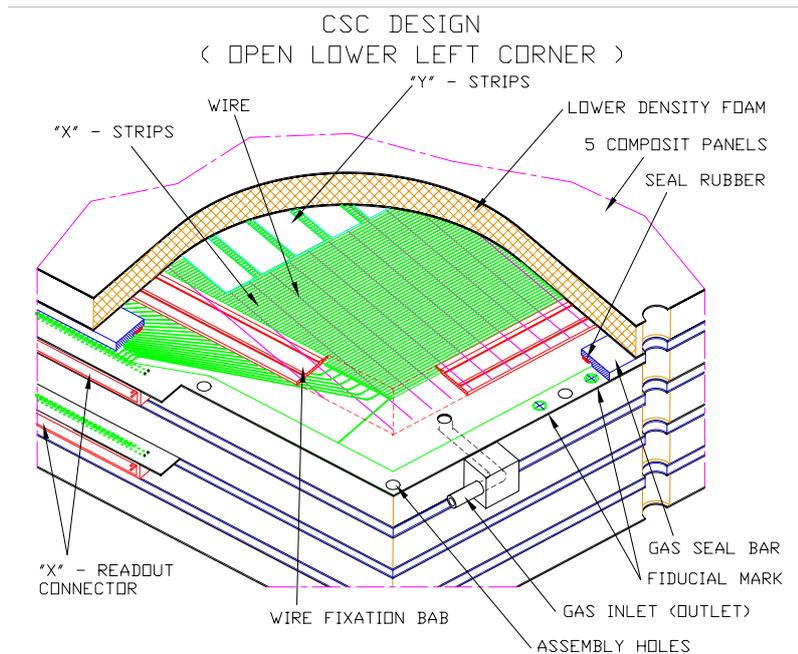
Figure 3.26: Schematic view of CSC [39].

Parameter	Value
Operating voltage	1900 V
Anode wire diameter	30 μm
Gas gain	6×10^4
Gas mixture	Ar (80%)/CO_2 (20%)
Total ionization	90 ion pairs

Table 3.4: Summary of the operating parameters of the CSC [39].

Muon trigger chambers

Because of the high background rates at the LHC, the muon drift chambers will have to operate at high levels of occupancy. For this reason, it was decided to use an dedicated, fast and hence low-occupancy chamber system for the trigger purpose.

The main tasks required to the ATLAS muon trigger system are:

- coarse measurement of and discrimination on the muon transverse momentum;

- bunch crossing identification;

- fast and coarse tracking to identify the hits of the precision chambers that are related to the detected muon track at the level-1 trigger;

- second-coordinate measurement with a required resolution of 5~10 mm.

Resistive Plate Chambers (RPC) are used for the barrel region and Thin Gap Chambers (TGC) are used for the end-cap regions. They cover the spectrometer acceptance up to $|\eta| \sim 2.4$. Both types of chambers generate fast signals with a time resolution of a few nsec and are used for the level-1 trigger where bunch crossing identification is needed. A spatial resolution of a few mm is adequate for these chambers. It is also used in the pattern recognition algorithm and provides the only measurement of the track coordinate in the non-bending plane.
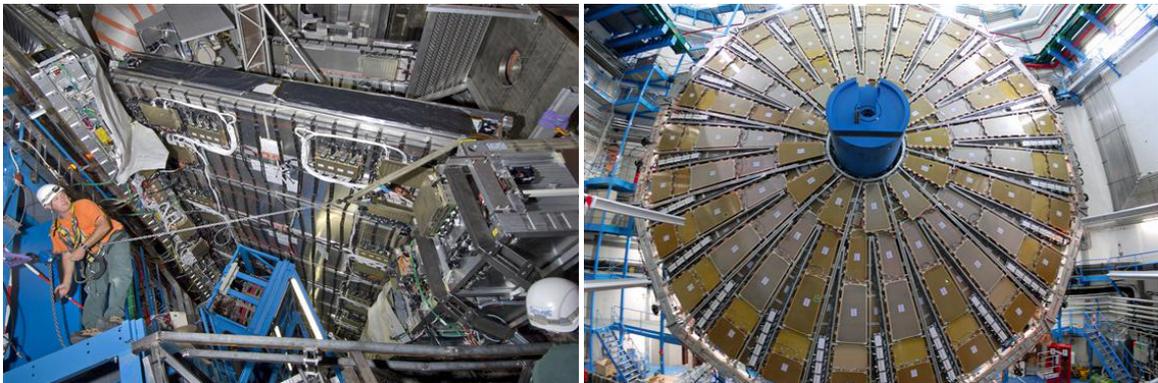
Figure 3.27: The ATLAS Muon Trigger chambers. RPC (left), TGC big wheel (right) [33].

TGC (Thin Gap Chamber)

Thin Gap Chambers operating in a saturated mode have a structure similar to Multi-Wire Proportional Chambers (MWPC), except that the anode-to-anode, i.e. wire-to-wire, distance is larger than the cathode-to-anode distance (see Fig. 3.28 and 3.29). With the use of a highly quenching gas mixture of CO_2 (55%) and n-C_5H_{12} (45%), this type of cell geometry allows operation in saturated mode. The mode has an advantage of small sensitivity to mechanical deformations, which is important for large detectors. Furthermore, operating in saturated mode leads to other beneficial properties of TGCs, for example:

- small parallax: the signal obtained by the passage of a minimum-ionizing particle has only a small dependence on the incident angle up to 40 degree.

- small Landau tails: less than two of the pulse-height distribution for a minimum-ionizing particle is contained in the tails (amplitudes more than 2σ above the mean of a Gaussian fit) of the pulse-height distribution.

The high electric field around the TGC wires (see Fig. 3.29) and the small distance between wires strongly reduce the drift component of ionization clusters, leading to very good time resolution. Figure 3.28 shows a cross section of a TGC triplet and of a doublet. The basic structure consists of 50 μm wires spaced every 1.8 mm. The anode plane is sandwiched between two graphite cathode planes at a distance of 1.4 mm. The cathode plane consists of a 1.6 mm FR4 plate on which the graphite is deposited. Behind the interior cathode plane, etched copper strips provide the readout of the azimuthal coordinate. In order to prevent the wire from sagging and to keep the anode-cathode distance constant, two types of the mechanical support parts are used; called "wire-support" and "button support". Each support part is intrinsically inefficient. On the outside, 1.6 mm FR4 plates with copper cladding, which provide the outside ground, are covered with a 5 mm thick low-cost paper honeycomb, to provide the needed protection from gas over-pressure. The outer honeycomb is covered by 500 μm of FR4. In the interior the two 1.6 mm FR4 plates are separated by a 20 mm thick paper honeycomb. The operating parameters are summarized in Table 3.5. Note that the triplet has three wire-planes, but only two strip-planes.

Parameter	Value
Gas gap	2.8±0.10 mm
Wire pitch	1.8±0.05 mm
Wire diameter	50 μm
Wire potential	2900±100 V
Operating plateau	200 V
Gas mixture	CO_2 (55%)/n-C_5H_{12} (45%)
Gas amplification	3×10^5

Table 3.5: Summary of the operating parameters of the TGC[39].

There are three stations with seven layers in the middle station around $z \sim$15 m. Each station is called "M1", "M2" or "M3" from the inner side, respectively. The layers are arranged in one triplet (M1 station) and two doublets (M2 and M3 station). These three
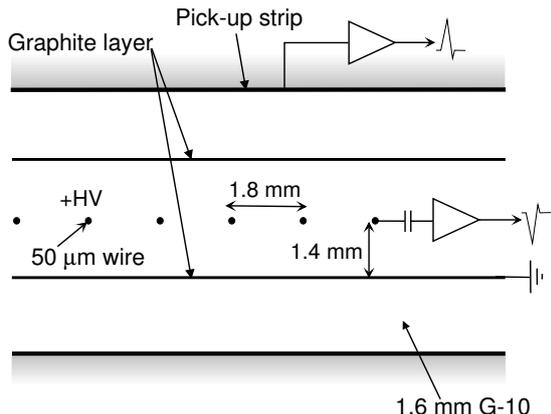
Figure 3.28: TGC structure [36].
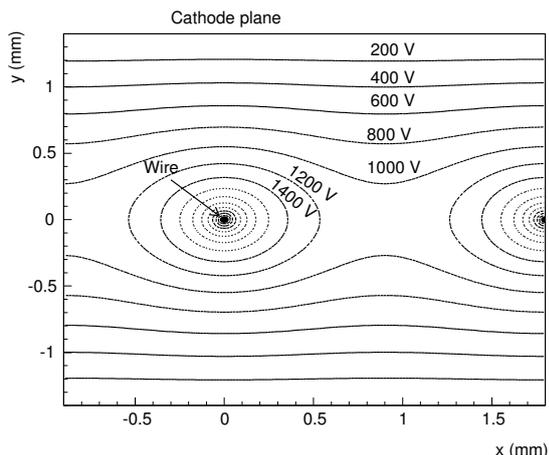
Figure 3.29: Equipotential lines in TGCs [36].

stations are mainly used for the muon trigger. There is another station (the inner station) around $z \sim 8$ m. A station with two layers is arranged in one doublet. The layout geometry, chamber overlapping and channel wiring have been arranged so that there are, to first order, no overlaps and no holes in this plane. The farthest plane from the interaction point is referred to as the "pivot" plane. Tracks passing through this plane can be given a unique η-ϕ coordinate. Because any track segment in the other planes must be in coincidence with this plane, double counting can be avoided in the level-1 trigger. The level-1 trigger looks for tracks in a cone opening backwards from the pivot plane.

RPC (Resistive Plate Chamber)

RPC is a gaseous detector providing a typical space-time resolution of 1 cm and 1 nsec with digital readout. The basic RPC unit is a narrow gas gap formed by two parallel resistive Bakelite plates, separated by insulating spacers. The primary ionization electrons are multiplied into avalanches by a high, uniform electric field of typically 4.9 kV/mm. Amplification in avalanche mode produces pulses of typically ~ 1 pC. RPCs will be operated with a gas mixture of $C_2H_2F_4$ (94.7%)/Iso-C_4H_{10} (5%)/SF_6 (0.3%), a non-flammable gas that allows for a relatively low operating voltage. The signal is read out via capacitive coupling by metal strips on both sides of the detector. A trigger chamber is made from two rectangular detector layers, each one is read out by two orthogonal series of pick-up strips. The one is the 'η strips' parallel to the MDT wires and provide the bending view of the trigger detector. The other is the 'ϕ strips' orthogonal to the MDT wires and provide the second-coordinate measurement also required for the offline pattern recognition.

The RPC has a simple mechanical structure, using no wires and, are therefore simple to manufacture. The 2 mm-thick plastic laminates are separated by a series of insulating spacers of 2 mm thickness, which define the size of the gas gap. The spacers are glued on both plates at 10 cm intervals. A 7 mm-wide frame of the same material and thickness as the spacers is used to seal the gas gap at all four edges. The mechanical structure of an RPC is shown in Fig. 3.30. The outside surfaces of the resistive plates are coated

with thin layers of graphite paint, which are connected to the high voltage supply. These graphite electrodes are separated from the pick-up strips by 190 μm thick PET films glued on both graphite surfaces. The readout strips are arranged with a pitch varying from 28 to 38 mm. Each chamber is made from two detector layers and four readout strip panels. These elements are rigidly held together by two support panels which provide the required mechanical stiffness of the chambers. The panels are made of light-weight paper honeycomb (40 kg/m^3) sandwiched between two copper sheets. One panel is flat, 50 mm thick, with 0.5 mm thick aluminum coatings. The other panel is 10 mm thick with 0.3 mm coatings and is preloaded with a 1 cm sagitta. The two panels are rigidly connected by 2 mm thick aluminum profiles, such that the preloaded support panel provides uniform pressure over the whole surface of an RPC module. The principal RPC parameters are summarized in Table 3.6. To preserve the good intrinsic time resolution of RPCs, the readout strips are optimized for good transmission properties and are terminated at both ends to avoid signal reflections. The front-end electronics are based on a three-stage voltage amplifier followed by a variable-threshold comparator. The amplifier frequency response is optimized for the typical time structure of RPC avalanches.

The middle plane is called the pivot plane, where the level-1 trigger procedure starts.
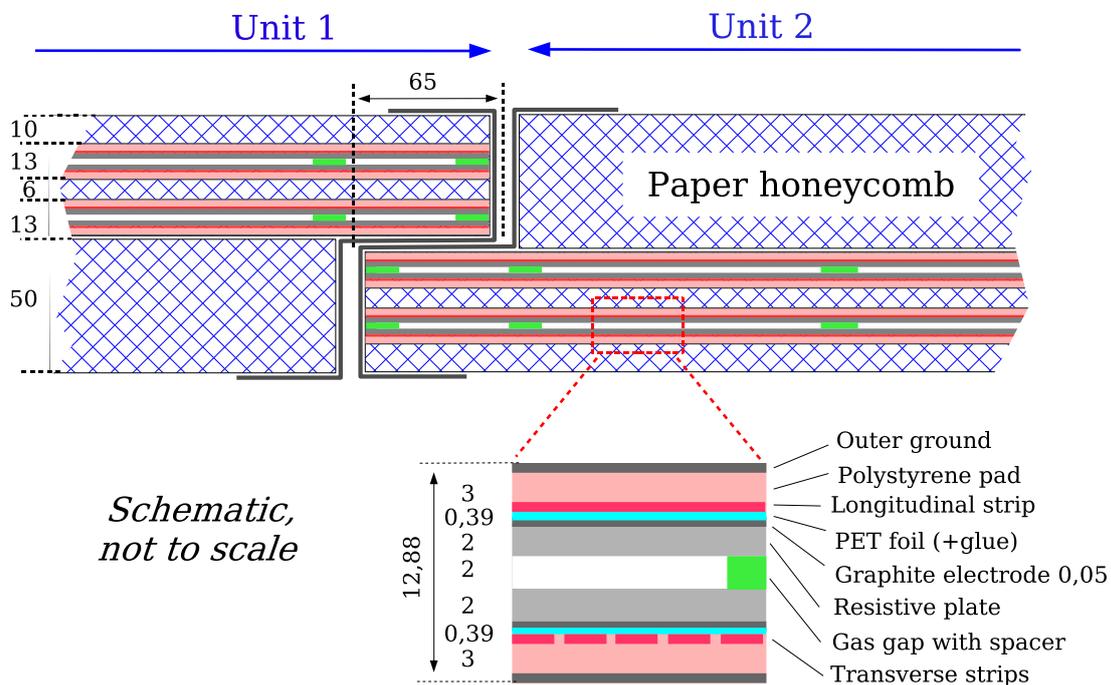

Figure 3.30: RPC structure [39].

Parameter	Value
E-field in gap	4.9 kV/mm
Gas gap	2 mm
Gas mixture	$C_2H_2F_4$ (94.7%)/Iso-C_4H_{10} (5%)/SF_6 (0.3%)
Readout pitch of η and ϕ strips	23–35 mm
Detection efficiency per layer	$\geq$98.5 %
Efficiency including spacers and frames	$\geq$97 %
Intrinsic time jitter	$\leq$1.5 nsec
Jitter including strip propagation time	$\leq$10 nsec
Local rate capability	$\sim$1 kHz/cm^2
Streamer probability	$\leq$1 %

Table 3.6: Summary of the operating parameters of the RPC [39].

3.3 The trigger system

At the LHC, the interaction rate of protons at the design luminosity is expected to be about 1 GHz. The trigger system is required to select interesting events effectively among enormous amount of such background events. The ATLAS trigger system is organized in three levels as shown in Fig. 3.31. Each step refines the previous decision by using the larger fraction of the data and more advanced algorithms.

3.3.1 The Level-1 trigger

The level-1 trigger (LVL1) is a hardware-based trigger which searches for high transverse momentum (high-p_T) leptons, photons, jets and large missing transverse energy ($\not{E}_T$) . It is designed to reduce the 40 MHz bunch-bunch crossing rate to 75 kHz (upgradable to 100 kHz). The latency, which is the time from the collision to LVL1 trigger decision, is required less than 2.5 μsec. The LVL1 trigger decisions are performed by using the calorimeters and the muon trigger chambers, the RPC and the TGC. The LVL1 trigger defines so-called "Region of Interest (ROIs)", where interesting features have been identified by using η and ϕ coordinates. The ROIs are used as staring points for higher level trigger algorithms.

3.3.2 The Level-2 trigger

The level-2 trigger (LVL2) is a software trigger, and uses the ROIs defined by the LVL1 trigger as seeds. The LVL2 trigger is dedicated to make trigger decision by using all the detector information inside the ROIs. The final trigger rate is about 3.5 kHz and the average processing time per event is 40 msec.

3.3.3 The Event Filter

The final event selection is performed by the Event Filter (EF), which reduces the event rate further to 200 Hz by using the ATLAS standard offline reconstruction algorithms. The

average processing time per event is 4 sec. The LVL2 and the EF together are called the High Level Trigger (HLT).

The decision for accepting an event is based on so-called trigger menus, which are sets of one or more event characteristics, e.g. $\not{E}_T$, muon etc., with certain thresholds. The thresholds of trigger menus can be adjusted depending on the luminosity to use the full capacity of the bandwidth.

The events passed the selection criteria are tagged on basis of the results of the EF and sorted into data streams. The physics streams defined in ATLAS are electrons, photons, muons, jets, taus, $\not{E}_T$ and B-physics. As ATLAS uses inclusive streaming: an event can be recorded in more than one stream. In addition, there are also calibration streams used to calibrate the detectors, and express streams used for monitoring and perform data quality checks.
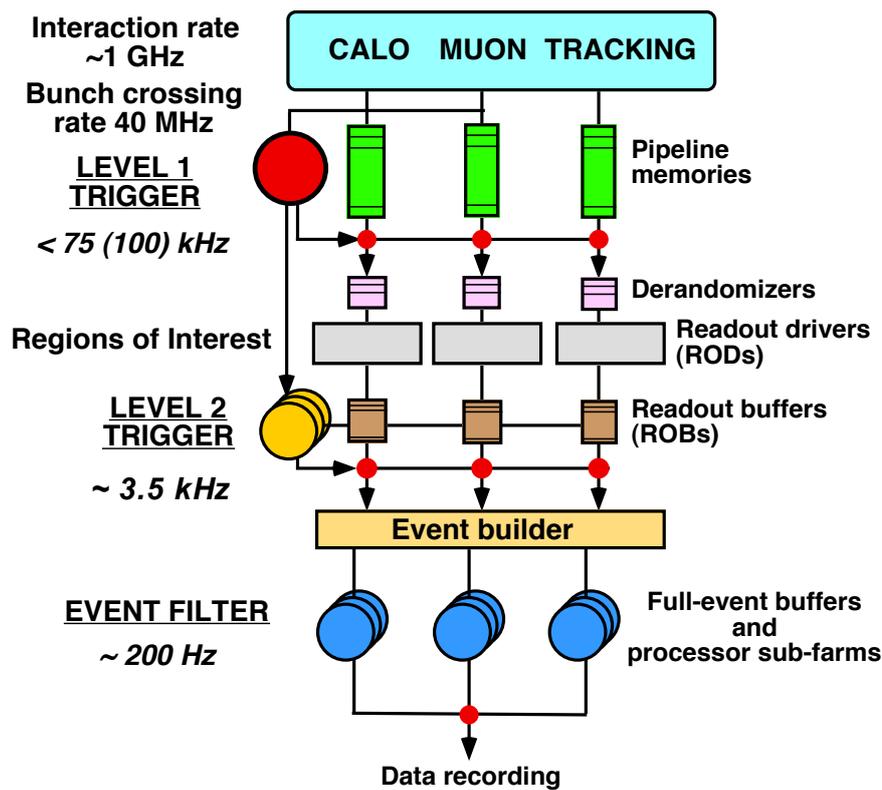

Figure 3.31: Schematic view of the ATLAS trigger system [41].

Chapter 4

Monte Carlo samples

The Monte Carlo samples used in this thesis are summarized in this chapter. The signal and background samples are generated at the center of mass energy of 7 TeV. Samples generated with PYTHIA [42] and HERWIG [43] (with JIMMY [44]) used a set of parameters tuned by ATLAS for its 2009 Monte Carlo generation [45]. All signals and backgrounds were passed through a GEANT4 [46] based simulation and were reconstructed with the same algorithms used for the data.

4.1   The Standard Model background samples

The main backgrounds in search for the charged SMPs are muons from the following Standard Model processes:

- **QCD jet production:**
  A large sample of inclusive jet events has been generated with PYTHIA 6.4.21. The hard interaction of the event is modeled via $2 \rightarrow 2$ matrix elements at leading order in the strong coupling constant. The production of top quarks is not included in this sample and instead a dedicated sample has been produced (see below). Additional initial and final state radiation are generated by a parton shower algorithm in the leading logarithm approximation. The QCD process provides the largest contribution for relatively low p_T jets, a region in which the leading logarithm approach provides a good description of the data. Multiple parton-parton interactions are simulated by extra $2 \rightarrow 2$ processes. The parton density functions used for this sample were the modified leading order distributions of MRST2007LO [47].

- $W/Z + \text{jets}$ **production:**
  The muons from $W^{\pm}$ or Z^0 bosons processes in association with jets is expected to be one of the most important backgrounds. As the event selection often requires many jets in the final state assuming that charged SMPs are generated in the SUSY event, it is particularly important to model multiparton final states. For this reason, the ALPGEN [48] Monte Carlo generator including electroweak and QCD effects for multiparton hard processes has been chosen. Jet production was generated for up to five-parton matrix elements, in different slices of momentum of the hard process ($\hat{p}_T$). The generator is interfaced to HERWIG [43] for showering and fragmentation

processes and JIMMY [44] generating the underlying event. The parton density functions used for these samples were the CTEQ6L1 set [49]. The limited number of such events in the current data sample precludes a data-driven estimate of the normalization, so that the samples were normalized to the integrated luminosity accumulated using the cross sections in Table 4.1. The overall normalizations of the $W \to \nu$ and $Z \to \nu\nu$ processes are based on next-to-next-to-leading order (NNLO) QCD corrections estimated from FEWZ program [50]. The same normalization scaling factor has been applied for all ALPGEN parton multiplicities.

- **Top pair ($t\bar{t}$) production:**
  The top pair production ($t\bar{t}$) process is an important background. The MC@NLO [51] [52] generator, including full next-to-leading order QCD corrections has been used to simulate the hard process. Parton showering and fragmentation were simulated by the HERWIG event generator with JIMMY [44] generating the underlying event. The $t\bar{t}$ cross sections were normalized to the next-to-leading order and next-to-leading log result [53]. The CTEQ6.6 next-to-leading-order parton set is used for the matrix element, the parton shower and the underlying event.

Physics process	Generator	cross section $\times$ Br [pb]
Di-jet (QCD) $17 \le \hat{p}_T \le 35$ GeV	Pythia	6.78×10^8 pb
Di-jet (QCD) $35 \le \hat{p}_T \le 70$ GeV	Pythia	4.10×10^7 pb
Di-jet (QCD) $70 \le \hat{p}_T \le 140$ GeV	Pythia	2.20×10^6 pb
Di-jet (QCD) $140 \le \hat{p}_T \le 280$ GeV	Pythia	8.8×10^4 pb
Di-jet (QCD) $280 \le \hat{p}_T \le 560$ GeV	Pythia	2.35×10^3 pb
Di-jet (QCD) $560 \le \hat{p}_T$	Pythia	34 pb
$W \to e\nu \ + \ N$-Jets ($N = 0 \sim 5$)	Alpgen	8.67×10^3 pb
$W \to \mu\nu \ + \ N$-Jets ($N = 0 \sim 5$)	Alpgen	8.68×10^3 pb
$W \to \tau\nu \ + \ N$-Jets ($N = 0 \sim 5$)	Alpgen	8.68×10^3 pb
$Z \to ee \ + \ N$-Jets ($N = 0 \sim 5$)	Alpgen	852 pb
$Z \to \mu\mu \ + \ N$-Jets ($N = 0 \sim 5$)	Alpgen	852 pb
$Z \to \tau\tau \ + \ N$-Jets ($N = 0 \sim 5$)	Alpgen	851 pb
$Z \to \nu\nu \ + \ N$-Jets ($N = 0 \sim 5$)	Alpgen	4.57×10^3 pb
$t\bar{t}$	MC@NLO	164 pb

Table 4.1: The expected muon backgrounds from the Standard Model processes in search for the charged SMPs. $\hat{p}_t$ is the transverse momentum of the two partons involved in the hard scattering process.

4.2   The signal samples

The GMSB Monte Carlo samples were used in the search for charged SMPs. Five bench-
mark points with different effective SUSY breaking parameters Λ are set. Table 4.2 shows
the Λ, mass of sleptons, which become charged SMPs, and the inclusive SUSY produc-
tion cross section for each benchmark point. In addition, the remaining parameters of the
GMSB models other than Λ are common among five benchmark points, and are summa-
rized in Table 4.3. Mass spectrum and branching ration are calculated using ISAJET [54].
Five set samples of 10^4 inclusive SUSY events were generated with the HERWIG [43] event
generator with JIMMY [44]. GMSB30 has lowest mass tau slepton $\tilde{\tau}$ close to the LEP limit
[55] [56].

	Λ	$M_{\tilde{\tau}}$	$M_{\tilde{e}}$, $M_{\tilde{\mu}}$	σ ($\sqrt{s} = 7$ TeV)
GMSB30	30 TeV	101.9 GeV	103.8 GeV	2.0 pb
GMSB35	35 TeV	116.3 GeV	118.3 GeV	0.84 pb
GMSB40	40 TeV	131.0 GeV	133.1 GeV	0.39 pb
GMSB50	50 TeV	160.7 GeV	163.0 GeV	0.11 pb
GMSB60	60 TeV	190.7 GeV	193.3 GeV	0.04 pb

Table 4.2: The parameter sets of the GMSB Monte Carlo samples used in this analysis.
The effective SUSY breaking parameter Λ, mass of the charged massive sleptons and the
inclusive SUSY production cross section are summarized.

C_{grav}	M_{mes}	N_5	$\tan \beta$	$\text{sgn}(\mu)$
5000	250 TeV	3	5	+

Table 4.3: The GMSB model parameters other than Λ.

Chapter 5

Velocity determination of the charged SMPs with the ATLAS muon spectrometer

Charged SMPs are expected to be reconstructed as muons with the ATLAS standard muon tracking algorithm. The algorithm reconstructs muon tracks by fitting segments, which are made from muon trigger chamber hits and the MDT hits. The MDT drift circles are calculated from drift time assuming that muons run from proton-proton interaction point at the speed of light. The drift circles for charged SMPs are reconstructed larger than the real drift circles due to late arrival in the muon spectrometers. This may confuse the segment finding. The confusion can be recovered, however, if a correct particle velocity $\beta = v/c$ is assumed. In fact, finding an optimal β value in the segment finding leads to a determination of β. MuonBetaRefitTool has been developed for this purpose. In this chapter, the method of the β measurement and performance of MuonBetaRefitTool are described.

5.1 Muon reconstruction algorithm at the ATLAS experiment

The purpose of the muon reconstruction is to measure properties of muons, namely 3-momentum and the charge from their trajectory in the magnetic filed. In ATLAS, three types of muon reconstruction are used:

- **Standalone:** muon track reconstruction using solely muon spectrometer data.

- **Combined:** matching the standalone muon tracks with inner detector tracks and possibly calorimeter measurements. The inner detector track improves the momentum resolution for muons with momenta below 100 GeV and reduce the fake rates of the standalone reconstruction.

- **Segment tag:** combining inner detector tracks with inner layer muon station measurements. This strategy provides additional information for detector regions where

standalone reconstruction is degraded, such as the region near $\eta = 0$ and the transition region where the track may not pass more than one MDT station. Also low energy muons not reaching the middle and outer stations can be recovered.

This section describes briefly one of the standalone muon tracking algorithm, MOORE (Muon Oriented Object REconstruction). More detail information of MOORE is written in the thesis [57] and [58]. The muon reconstruction is performed in three distinct steps.

- Pattern Finding

- Segment Making

- Track Building
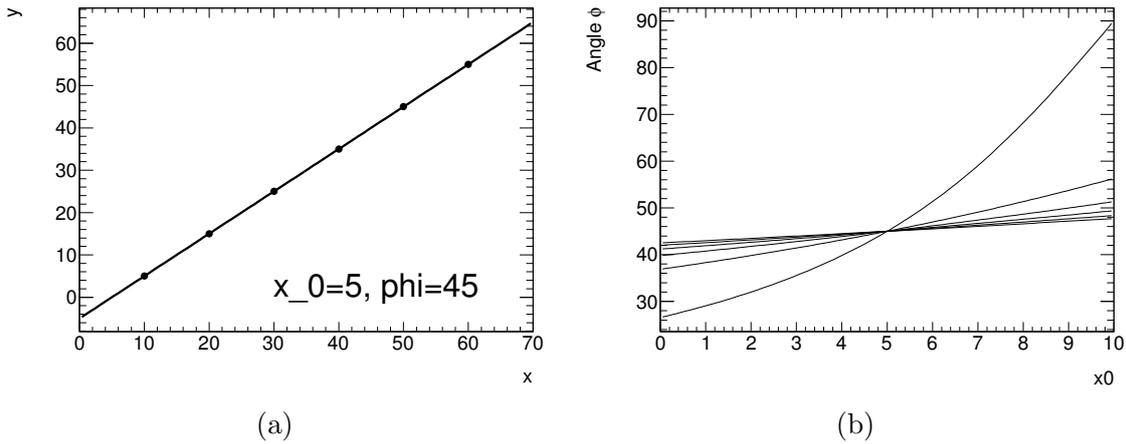
Figure 5.1: Set of points (a) and their representation in the Hough space (b).

5.1.1   Pattern Finding

The aim of the pattern finding is to group hits belonging to same trajectory. In pattern finding, MOORE uses the Hough transformation [59, 60, 61, 62], which is widely used in estimating parameters for shapes and patterns in digital images. A specific example is given in Fig.5.1-(a) where a line going through points in an xy-plane is searched for using the Hough transformation:

$$\phi(x, y, x_0) = \tan^{-1}\left(\frac{y}{x - x_0}\right).$$
(5.1)

For any points (x, y) in nominal space, the transformation gives a relation in (x_0, ϕ) space, so-called Hough space (Fig.5.1-(b)), as a curve. The parameter x_0 is the free parameter of the transformation. The curves corresponding to points belonging to a line cross in one point in Hough space. The position of the crossing point corresponds to the parameters of the line in the nominal space.

In practice, the crossing point is obtained with binned Hough space. The value of ϕ is calculated for all bin of x_0, and filled in Hough space as shown in Fig 5.2. The problem to

find the crossing point of the curves, i.e. parameters of the straight line, can be solved by finding the maximum peak in binned Hough space.

The muon spectrometers measure either a position in xy-plane or in rz-plane. Therefore, the pattern search is split in two independent steps.
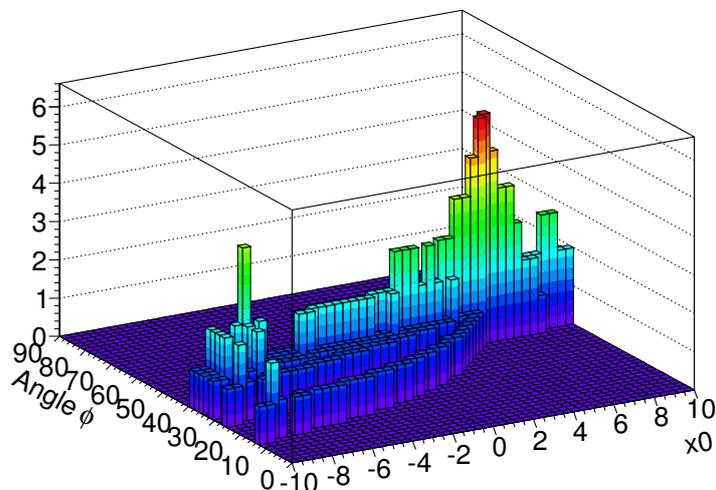

Figure 5.2: Representation points in binned Hough space.

xy-plane

Since the toroidal magnetic field in the radial direction is negligible, a trajectory of muon in the xy-plane can be considered as a straight line approximately pointing to the proton-proton interaction point. Therefore, patterns of muon tracks are described with the azimuthal angle ϕ and the impact parameter r_0 in the xy-plane. The following Hough transformation is used in determining two parameters:

$$\phi(x_{\mathrm{hit}}, y_{\mathrm{hit}}, r_0) = \tan^{-1}\left(\frac{y_{\mathrm{hit}}}{x_{\mathrm{hit}}}\right) + \tan^{-1}\left(\frac{\sqrt{r_{\mathrm{hit}}^2 - r_0^2}}{r_0}\right), \qquad (5.2)$$

where ϕ is the angle with respect to the x-axis, x_{hit} and y_{hit} are the x and y coordinates of the global hit position and $r_{\mathrm{hit}} = \sqrt{x_{\mathrm{hit}}^2 + y_{\mathrm{hit}}^2}$.

For each hit in events, ϕ values are calculated with all possible value of r_0, and filled in the Hough space. When a trajectory is determined by finding maximum in the Hough space, the distances d in xy-plane of the hits to the trajectory are calculated, and hits satisfying $d < 250$ mm are associated to the trajectory. If more than one hit are associated, the trajectory is accepted as "ϕ-pattern".
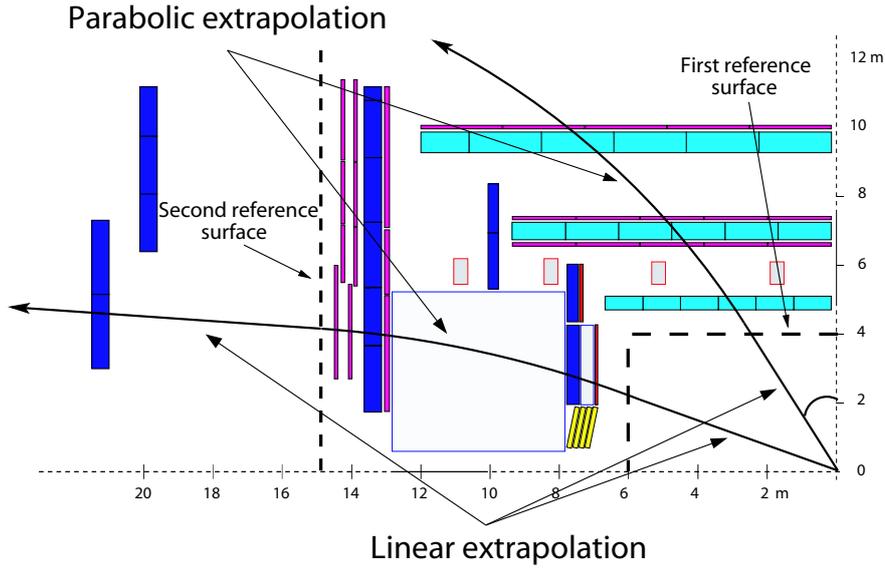
Figure 5.3: Track extrapolation in the barrel and end-cap regions [57, 58]. A straight
line trajectory approximation is used up to the entrance of the muon spectrometer ($r =$
4 m, $z = 6$ m) and in the end-cap outer regions ($z > 15$ m). In the barrel and end-cap
part ($z < 15$ m), trajectories are curved.

rz-plane

In rz-plane, a more complex track model is used as shown in Fig. 5.3 because a straight
line approximation is not sufficient to describe the trajectory for low momentum muons.

In the inner detector and calorimeters, the solenoidal magnetic field dose not affect
muons in rz plane. Therefore, a straight line approximation is used up to the entrance of
the muon spectrometers. After that, muons are bent in the toroidal magnetic field. This
bending curve is described using parabola. If muons run in the direction of end-cap regions,
a straight line approximation is used again after the middle stations because there is no
magnetic field.

The Hough space in the bending plane has two parameters, the polar angle θ between
y-axis and a straight line pointing to the interaction point and the curvature C. The
curvature is a free parameter in the Hough transformation and used together with the hit
position in order to calculate the angle θ:

$$\theta = \theta(r, z, C). \tag{5.3}$$

The hit positions measured in rz-plane fills the Hough space. After trajectories are
determined by finding the maximum in the Hough space, the hits are associated to the
trajectory. The trajectory with more than one associated hit is accepted as "η-pattern".
The detail of the Hough transformation and hit association in the bending plane on the
MOORE algorithm are given elsewhere [57].

Merging

After the pattern search is done, MOORE pattern finding algorithm combines the ϕ and η patterns to a three-dimensional pattern.

5.1.2 Segment Making

After the pattern finding, the MDT hits in a station are combined to form a segment. The first step of this procedure is to list up all possible combinations of hit pairs. For each pair, four tangent lines to their drift circles are calculated as shown in Fig. 5.4. Each tangent line is taken as a seed for the segment. Comparing the seed angle θ_{line} with the angle θ_{pred} from patten prediction, only the lines, which satisfy $|\sin(\theta_{\text{line}} - \theta_{\text{pred}})| < 0.2$, are chosen. Furthermore, segment candidates are formed by associating MDT hits in a station within the radial residual, $|\Delta r| = |r_{\text{drift}} - r_{\text{line}}|$, less than 1.5 mm with respect to the seed lines as shown in Fig. 5.5. Segments are reconstructed by fitting a straight line to drift circles in a
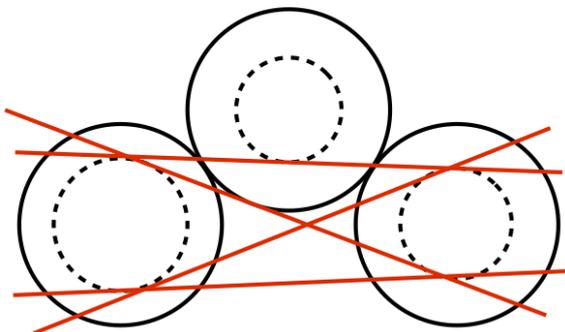

Figure 5.4: Drift circle seeds with four tangent lines
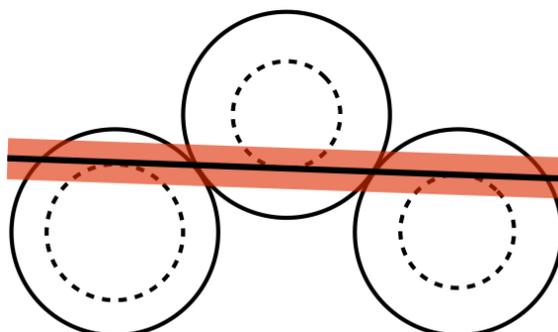
Figure 5.5: Make segment candidate by associating hits with tangent line.

segment candidate. The fit χ^2 is calculated as follows:

$$\chi^2 = \sum_{i=1}^{n} \frac{(\Delta_i - r_i)^2}{\sigma_i^2}, \tag{5.4}$$

where Δ_i is the distance from the track to the wire, r_i is measured drift radius and σ_i is corresponding error. When the angle θ and the distance d are defined as in Fig. 5.6, Δ_i can be represented using θ and d:

$$\Delta_i = d + z_i \sin\theta - y_i \cos\theta. \tag{5.5}$$

The measured drift radius r_i is estimated using the drift time t_{drift} defined as follows:

$$t_{\text{drift}} = t_{\text{TDC}} - t_{\text{TOF}} - t_{\text{prop}} - t_0, \tag{5.6}$$

where t_{TDC} is the measured TDC counts for each tube. t_{TOF} is the arrival time of muons, which is calculated assuming that muons originated from proton-proton collisions runs at the speed of light ($\beta = v/c = 1$). t_{prop} is the propagation delay time during which the signal

pulse propagates from the impact position of the muons along the tube to the readout. t_0 is defined as the sum of all remaining delays. The largest contribution to the t_0 are delays due to cabling.

After the reconstruction, segments are associated with the trigger hits of the RPC or the TGC using the pull p value defined as:

$$p = d/\sqrt{\sigma_{\mathrm{clus}}^2 + \sigma_{\mathrm{seg}}^2}, \tag{5.7}$$

where d is the distance of the trigger hit to the segment in the precision plane of the MDT, σ_{seg} is the error on the track prediction and σ_{clus} is the measurement error of the trigger hit. The RPC hits are associated with a segment if the distance to the segment is smaller than 7 times the total error: $|p| < 7$. The TGC hits are associated with a segment by requiring $|p| < 20$.
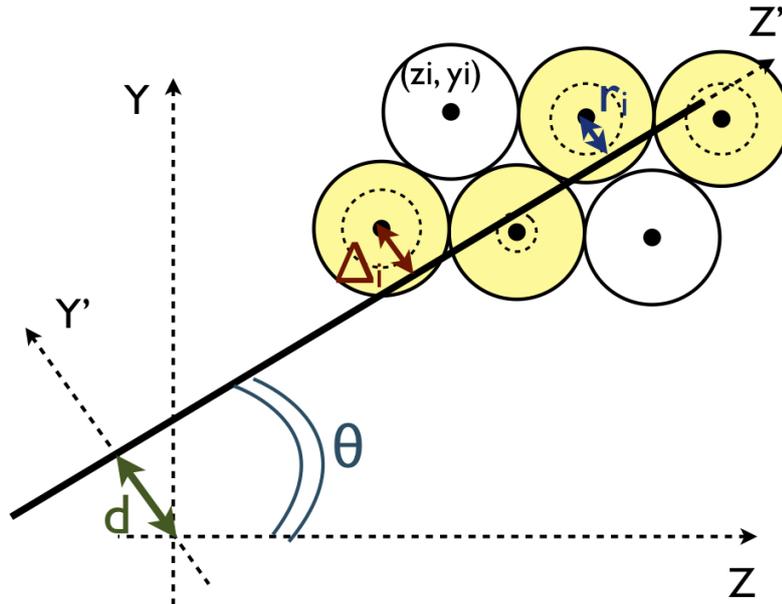

Figure 5.6: Segment reconstruction

5.1.3 Track Building

SegmentCombiner performs to find track candidates by combining with at least two segments reconstructed in the previous stage. In general, a segment is considered to be combined with another segment when they are originated from same pattern and a simple χ^2 fit gives an absolute pull lower than 5 for the position and direction of both of the segments. The pull p of a fitted value x, where x represents either the position or the direction, is defined as:

$$p = \frac{x_{\mathrm{meas}} - x_{\mathrm{fit}}}{\sqrt{\sigma_{\mathrm{meas}}^2 + \sigma_{\mathrm{fit}}^2}}, \tag{5.8}$$
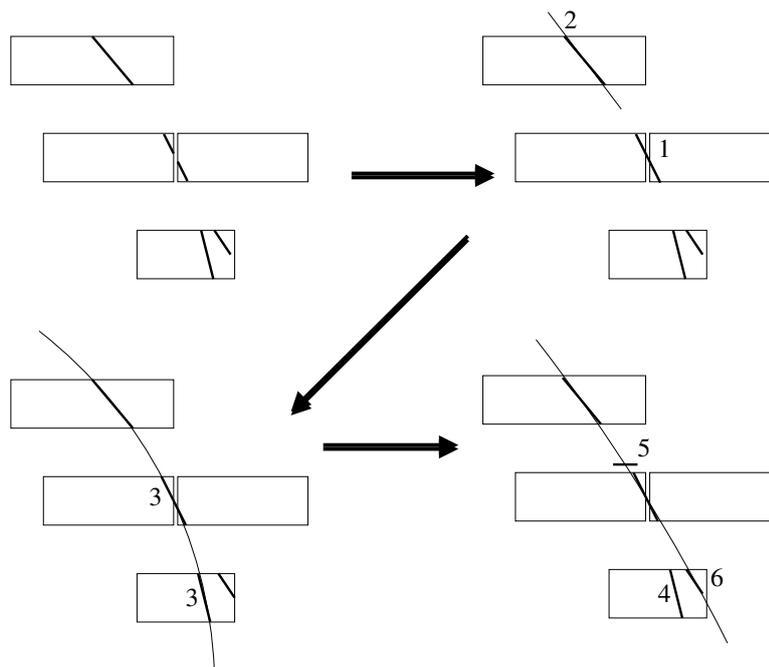
Figure 5.7: Schematic overview of the track building [58]. Step1: resolving segments in neighboring station into on segment; step2: select a seed segment for building the track; step3: add segments to the track; step4: remove wrongly associated segment from the track; step5: add possibly hits (in this case, a trigger hit is added); step6: add possible miss segment to the track.

where x_{meas} is the measured value and σ_{meas} is its error; x_{fit} is fit value and σ_{fit} is its error. For two segments in a overlap region and middle-outer end-cap regions, a straight line fit is performed. For other chambers, a curved line fit with IP constraint is performed. If it is failed to fit with a curved line (i.e. one of the absolute pull values is larger than 5), the fitting is retried using a straight line.

These track candidates are finally fit to a track by MOORE track builder in the following steps, as shown in Fig. 5.7. More detailed information for each step is given elsewhere [58].

1. **Resolving station overlaps:** Segments in neighboring stations are merged for tracks.

2. **Seed selection:** As the tracks are built segment by segment, it is preferred to start with a well-reconstructed segment (e.g. isolated in a station) as the seed.

3. **Adding segments:** Segments associated to a same track candidate are added to the track.

4. **Track cleaning:** After the track building, wrongly associated segments are removed.

5. **Hit recovery:** Possible missed hits (e.g. trigger hits) are put on the track.

6. **Segment recovery:** Possible missed segments are put on the track.

7. **Ambiguity solving:** If individual hits can be assigned to multiple tracks, this needs
to be resolved.

5.1.4 Reconstruction of the combined muon tracks

The Muid (Muon identification) algorithm [63] combines muon spectrometer tracks reconstructed by MOORE with the inner detector tracks and determines the parameters of
muons at the primary vertex. The advantages of reconstructing the combined muon tracks
are as follows:

- **Improve momentum resolution:** For $p_T < 30$ GeV, the inner detector provides
  the best measurement. Therefore, low momentum muons will be reconstructed with
  a high efficiency and a better momentum resolution. Furthermore, although the momentum resolution in the muon spectrometers suffers from the energy loss fluctuation
  in the calorimeters, the effect can be reduced by combined fitting with the parameters
  of the inner detector tracks.

- **Reduce background and fake rate:** Muons produced in the calorimeters, e.g.
  from π/K decays, will be reduced by reconstructing combined tracks. In addition,
  fake tracks from pile-up and cavern backgrounds will be reduced because there will
  not be inner detector tracks matched with these tracks in general.

The Muid extrapolates the spectrometer tracks back to the interaction point through
the calorimeters, taking into account scattering and enregy loss in the first stage (Muid
standalone). These muons are called "standalone muons".

In the second stage (Muid combined), tracks are matched by calculating a match-χ^2
with five track parameters, d_0, z_0, ϕ_0, θ and q/p, of the inner detector tracks and standalone
muon tracks. If a match-χ^2 is less than 30, a combined muon track is built by refitting to
all the measurements and scatters from the inner detectors, the calorimeters and the muon
spectrometers.

5.2 Reconstruction of charged SMPs with Muid and Staco

Figure 5.8 shows the track reconstruction efficiency in terms of β for stable massive sleptons
in GMSB30 Monte Carlo sample using two algorithms for muon track reconstruction, Muid
and Staco [*1)] [64]. The track reconstruction efficiency is defined as the number of sleptons
in $|\eta| < 2.4$ reconstructed with each muon track reconstruction algorithm divided by the
number of sleptons generated in $|\eta| < 2.4$.

[*1)]The other muon tracking algorithm for ATLAS. Using hits in the muon spectrometers, the Muonboy
algorithm [64] reconstructs standalone track with the following steps: (i) identification of regions of activity
in the muon system, through the RPC/TGC systems; (ii) reconstruction of local segments in each muon
station in these regions of activity; (iii) combination of segments of different muon stations to form track
candidates using three-dimensional tracking; (iv) global track fit of the muon track candidates through the
full system using individual hit information.

After the reconstruction of standalone muon tracks, the Staco (Statistical combination) algorithm combines the standalone tracks with inner detector tracks by using statistical method in order to form combined
muon tracks.
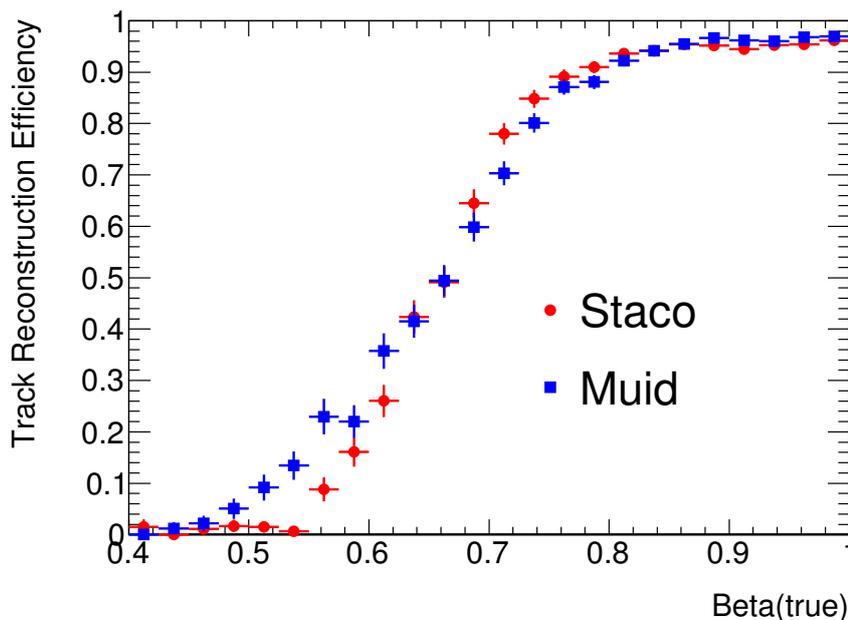
Figure 5.8: The track reconstruction efficiency for stable massive sleptons in Gauge Mediated SUSY-breaking (GMSB30) Monte Carlo sample with the Staco and the Muid.

In $\beta > 0.8$, both algorithms can reconstruct tracks of sleptons as muons with high efficiency. However, the efficiency drops at β lower than 0.8. The reasons for degradation of the efficiency of sleptons with lower β are as follows.

- Muon tracks are reconstructed by fitting the segments found with MDT drift circles with the assumption of $\beta = 1.0$. Drift circles of the MDT for charged SMPs are reconstructed larger than the real drift circles due to late arrival in the muon spectrometers. In this case, bad fit quality tracks are reconstructed and may be rejected due to larger fit-χ^2 by MOORE. This causes the degradation of track reconstruction efficiency for sleptons with low β.

- There is a possibility that the hits of muon trigger chambers for sleptons are in the next bunch crossing (BC) instead of the nominal BC. The probability is larger for sleptons running to the direction of end-cap regions ($|\eta| > 1.05$) because the distance from the proton-proton interaction point to the TGC is larger than that to the RPC. In this case, track reconstruction for sleptons is impossible due to the lack of ϕ hits.

Therefore, for finding charged SMPs with the muon spectrometers, it is necessary to take into account the late arrival time of charged SMPs and to reconstruct tracks using trigger chamber hits in the next bunch crossing.

5.3   MuonBetaRefitTool

MuonBetaRefitTool has been developed to search for charged SMPs with a high efficiency using MOORE. This algorithm performs special reconstruction for tracks in the muon spectrometer by adding the following three steps:

- Reconstructing the "seed tracks" with given β values.

- Finding the best β value by finding a minimum in χ^2 of the seed track fit.

- combining refit tracks with the best β value with inner detector tracks using Muid.

5.3.1   Reconstruction of seed tracks with β assumptions

MuonBetaRefitTool reconstructs tracks using the MDT drift circles obtained by assuming a lower β. This algorithm is performed in two steps:

- **MooLowBetaSegmentCombinationFinder**, which finds segments with drift circles reconstructed using the assumed β value by the MOORE segment finder.

- **MuonLowBetaCombiTrackMaker**, which reconstructs tracks by fitting the segments found with MooLowBetaCombinationFinder.

In addition, MuonBetaRefitTool also uses not only the TGC hits in the nominal BC but also those in the next BC in seed track reconstruction to avoid failure of track reconstruction due to the lack of ϕ measurements because of late arrival of charged SMPs.

The tracks with a given β value is called "seed tracks". The seed tracks are obtained for various β values: $\beta = 0.8, 0.6, 0.5, 0.4$. In addition, tracks reconstructed by MOORE are used as the seed tracks with the assumption $\beta = 1.0$.

There are sometimes more than one seed tracks satisfying the following conditions:

- The degrees of freedom of seed tracks, which corresponds to the number of hits on the track in the muon spectrometer, are very similar. The directions (η, ϕ) are also similar. Therefore, the seed tracks are expected to be reconstructed by using the same hit pattern.

- However, the fit-χ^2 values of the seed tracks are very different because of different β assumption in track reconstruction.

To reduce the duplication, each seed track is compared with all previously reconstructed tracks and if a pair of tracks satisfies with the following requirements, the track with the largest reduced χ^2 is removed:

- same charge

- $\Delta R = \sqrt{\Delta\eta^2 + \Delta\phi^2} < 0.05$
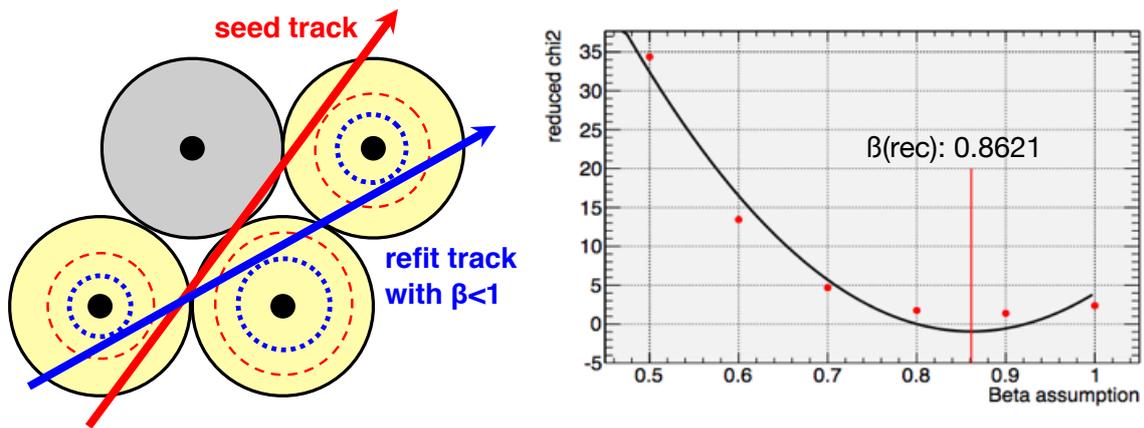
Figure 5.9: Refit seed track to drift circles of the MDT recalculated with β assumptions

5.3.2 β measurement

MuonBetaRefitTool measures β using the reconstructed seed tracks as follows.

1. recalculate drift circles of the MDT tubes traversed by the reconstructed seed track (depicted with yellow circles in Figure 5.9) changing β assumption between 0.5 and 1.0 by 0.1 steps and refit the seed track to the "new" drift circles, which are depicted with blue doted circles.

2. find $\beta_{\min}$, where reduced χ^2 of the refit seed track is minimum among the six β points and calculates the β_{expected}, where the quadratic function passing through three β points in $[\beta_{\min} - 0.1, \beta_{\min} + 0.1]$ is minimum.

3. refit seed tracks changing β assumptions in $[\beta_{\text{expected}} - 0.02, \beta_{\text{expected}} + 0.02]$ by 0.01 steps again and find the reduced χ^2 minimum with a quadratic function fitted to the five β points using the least squared method.

5.3.3 Combines refit tracks with inner detector tracks using the Muid

After having refit seed tracks with the measured β, these tracks are extrapolated to the primary vertex and combined with tracks in the inner detector using the Muid algorithm in order to correct their momenta due to the energy loss in the calorimeters.

Performance study of MuonBetaRefitTool will be described in next chapter.

Chapter 6

Performance of the reconstruction of charged stable massive particles

In this chapter, the performance study of MuonBetaRefitTool is described using the GMSB Monte Carlo samples, in which scalar leptons behave as charged SMPs. Muons in 7 TeV proton-proton collisions are also used for the performance study.

6.1 Performance for GMSB Monte Carlo samples

The performance of MuonBetaRefitTool is evaluated using various GMSB Monte Carlo samples (see section 4.2).

In this study, tracks of charged SMPs reconstructed by MuonBetaRefitTool are required to be in the detector acceptance, $|\eta| < 2.4$. A reconstructed track is considered to be originated from a true charged SMP if the distance between the reconstructed and true tracks, $\Delta R = \sqrt{(\Delta\eta)^2 + (\Delta\phi)^2}$, is less than 0.1.

6.1.1 β reconstruction

The resolution of measured β for the charged SMP tracks is represented by the fractional difference in β:

$$\frac{\Delta\beta}{\beta} = \frac{\beta_{\mathrm{rec}} - \beta_{\mathrm{true}}}{\beta_{\mathrm{true}}}, \tag{6.1}$$

where β_{rec} is the measured value and β_{true} is the true value for sleptons. Figure 6.1 shows the mean value and standard deviation obtained by fitting the $\Delta\beta/\beta$ distribution with the Gaussian function, as a function of the true value of β.

MuonBetaRefitTool can measure β with $3 \sim 5$ % accuracy for sleptons with β_{true} more than 0.6. On the other hand, the measured β values for sleptons with $\beta_{\mathrm{true}} < 0.6$ shift to lower values. This is because these sleptons becomes slower at the entrance of the muon spectrometer than at the proton-proton interaction point due to large energy loss at materials in front of the muon spectrometer. To prove the consideration, the fractional change of β due to the energy loss at the calorimeters, $\Delta\beta$, is checked. It is defined as follows:

$$\Delta\beta = \frac{\beta_{\mathrm{MS}} - \beta_{\mathrm{true}}}{\beta_{\mathrm{true}}}, \tag{6.2}$$
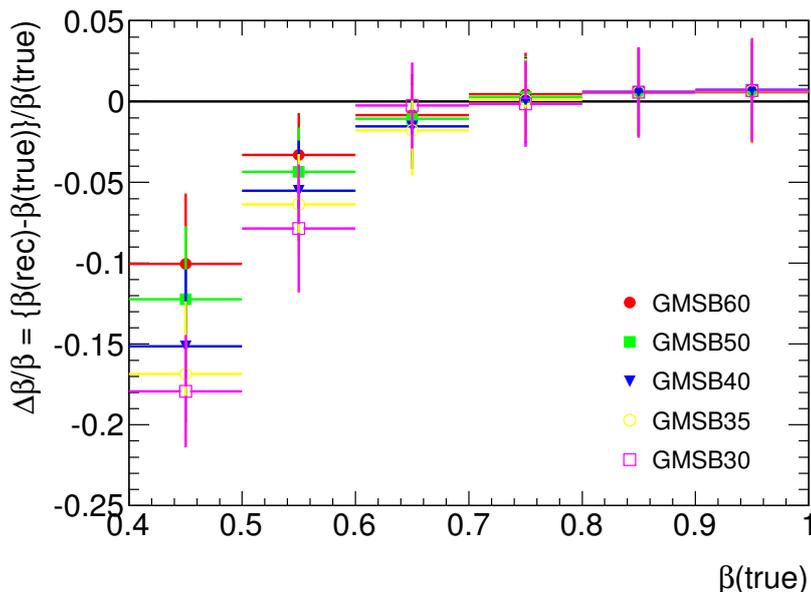
Figure 6.1: β measurement for sleptons in various GMSB Monte Carlo samples.

where β_{MS} is the velocity of slepton at the entrance of muon spectrometers calculated with the energy loss at the calorimeters. Figure 6.2 shows the energy loss at the calorimeters, and $\Delta\beta$ in terms of β_{true} for sleptons in the GMSB40 Monte Carlo sample. The energy loss at the calorimeter is larger as β_{true} becomes lower. It can be seen that $\Delta\beta$ for sleptons with $\beta_{\text{true}} < 0.6$ is large. Figure 6.3 shows the correlations between $\Delta\beta/\beta$ and $\Delta\beta$ for sleptons with $\beta_{\text{true}} < 0.6$ in the same Monte Carlo sample. From this figure, $\Delta\beta/\beta$ seems to be matched with $\Delta\beta$ reasonably well. Therefore, it can be concluded that sleptons with lower β at the interaction point run more slowly after traversing the calorimeters due to large energy loss.

Figure 6.4 shows the β reconstruction efficiency for various GMSB samples. The efficiency is defined as the number of sleptons with successfully reconstructed β divided by the total number of generated sleptons. MuonBetaRefitTool can recover the efficiency drop in $\beta < 0.8$ with the Staco and the Muid, and reconstruct sleptons with high efficiency ($90 \sim 95\%$) in the region $\beta > 0.5$. The reasons for the degradation of efficiency for sleptons are as follows.

- Figure 6.5 shows the distribution of θ (the angle between the track and the beam axis) of a fraction of sleptons with $\beta_{\text{true}} > 0.5$, whose β cannot be reconstructed. Sleptons are mainly running in the direction of $\theta = 90°$, where there are holes in the muon spectrometers. In addition, there are slptons running in the direction of $\theta = 30°$ and $150°$. The reason why these sleptons could not be reconstructed was studied with the two dimensional plot in Fig. 6.6, which shows the correlation between θ and ϕ. The ϕ dependence depicted red dots in the regions of $\theta \sim 30°$ and $\theta \sim 150°$ is seen clearly. Tracks of sleptons in thses directions cannot be reconstructed because
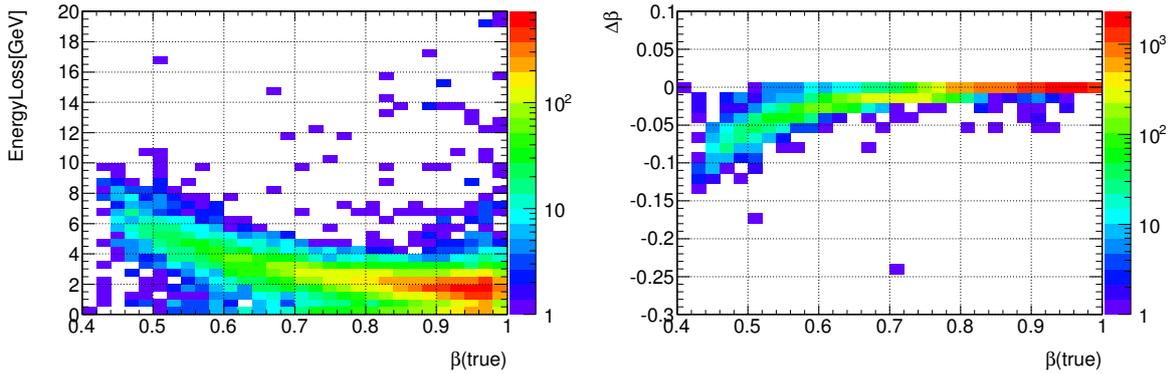
Figure 6.2: The energy loss at the calorimeter (left) and $\Delta\beta$ (right) in terms of β_{true} for sleptons in GMSB40 Monte Carlo sample.
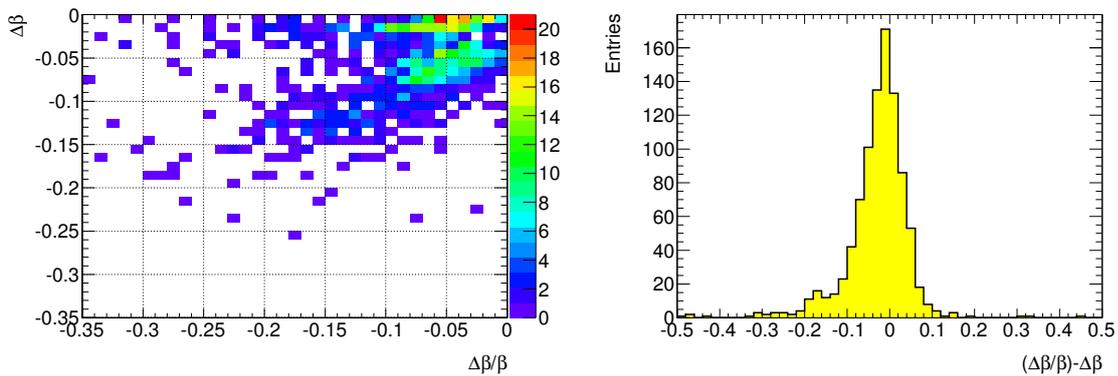

Figure 6.3: (Left); The correlation between $\Delta\beta/\beta$ and β, (Right); the difference between $\Delta\beta/\beta$ and β for sleptons with $\beta_{\text{true}} < 0.6$ in GMSB40 Monte Carlo sample.

there are holes of MDT stations. A small fraction of sleptons running in $\theta < 20°$ and $\theta > 160°$, where muons have few MDT hits due to the CSC regions, can be also found in Fig. 6.5.

- Light sleptons cannot reach the muon spectrometers because they often stop in the calorimeters or move more slowly due to ionization energy loss. Figure 6.7 shows the total energy with the energy loss at the calorimeters taken into account, for sleptons with $\beta_{\text{true}} < 0.5$ in GMSB30 Monte Carlo sample, which cannot be matched with any reconstructed tracks, in terms of true β value. The total energy of sleptons after considering the energy loss at the calorimeters is similar to their mass ($M_{\tilde{e},\tilde{\mu}} = 103.8$ GeV, $M_{\tilde{\tau}} = 101.9$ GeV) as the true value of β becomes lower.

Figure 6.8 shows measured β of muons in the $t\bar{t}$ Monte Carlo sample. Most of muons generated in proton-proton collisions run at the speed of light. MuonBetaRefitTool can measure β of most of muons well. However, this distribution has long tail in $\beta < 0.9$ due to mis-measurement. A treatment for β mis-measurement is described later in detail.
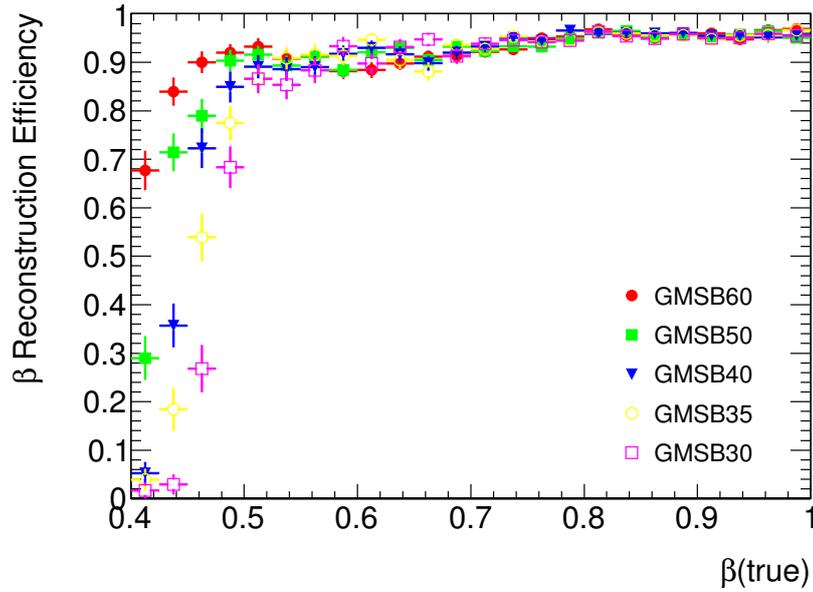
Figure 6.4: The β reconstruction efficiency for the GMSB Monte Carlo samples.
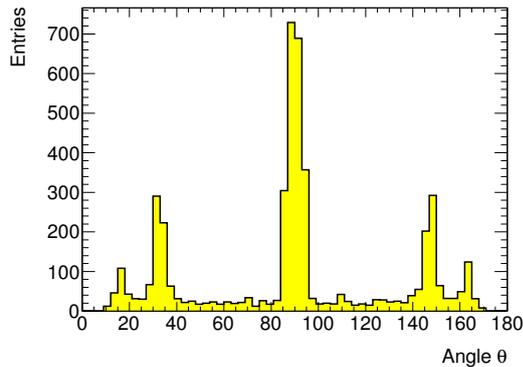

Figure 6.5: The distribution of θ for sleptons with $\beta_{\text{true}} > 0.5$ (using all GMSB samples), which cannot be reconstructed their velocities β.
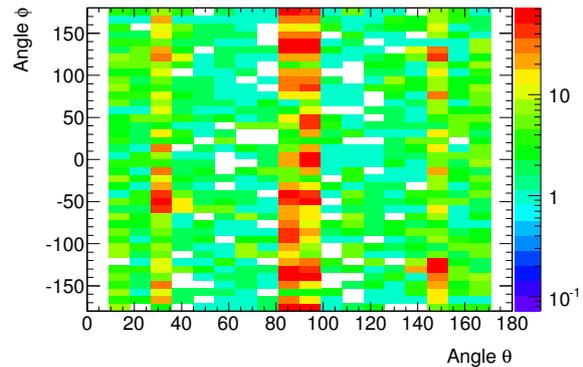

Figure 6.6: The correlation between θ and ϕ for sleptons with $\beta_{\text{true}} > 0.5$ (using all GMSB samples), which cannot be reconstructed their velocities β.

6.1.2 Mass measurement

The mass of the reconstructed particle is calculated with β and momentum p using the following formula:

$$m = \frac{p}{\beta\gamma},\tag{6.3}$$
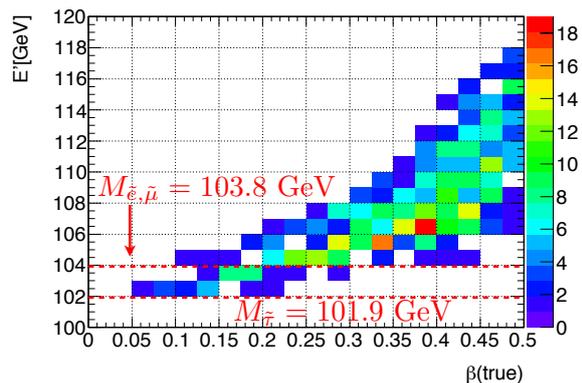
Figure 6.7: The total energy taken into account the energy loss at the calorimeters for sleptons in GMSB30 sample, which didn't match any reconstructed tracks, shown as a function of β.
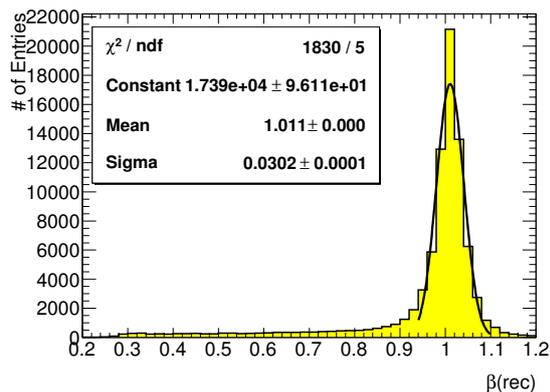

Figure 6.8: β distribution of muons in $t\bar{t}$ Monte Carlo sample.

where $\gamma = 1/\sqrt{1-\beta^2}$. Figure 6.9 shows the distributions of reconstructed mass for sleptons with $\beta_{\rm rec} < 0.9$ in various GMSB Monte Carlo samples. Table 6.1 shows the mean value and width obtained by fitting each mass distribution with a Gaussian function for every GMSB samples. In addition, Table 6.2 shows the mean value and the standard deviation obtained by fitting each distribution of $\Delta M/M$ defined as $\Delta M/M = (M_{\rm rec} - M_{\rm true})/M_{\rm true}$ with a Gaussian Function, which is shown in Fig. 6.10. MuonBetaRefitTool can measure sleptons masses with an accuracy of about 8 %.

	GMSB30	GMSB35	GMSB40	GMSB50	GMSB60
mean	103.5 GeV	117.7 GeV	131.9 GeV	161.3 GeV	190.3 GeV
width	8.9 GeV	9.8 GeV	11.9 GeV	13.2 GeV	14.9 GeV
$M_{\tilde{\tau}}$	101.9 GeV	116.3 GeV	131.0 GeV	160.7 GeV	190.7 GeV

Table 6.1: The mean value and width for each mass distribution of sleptons with $\beta_{\rm rec} < 0.9$.

	GMSB30	GMSB35	GMSB40	GMSB50	GMSB60
mean($\Delta M/M$)	0.009	0.005	0.005	0.003	-0.0001
$\sigma(\Delta M/M)$	0.079	0.080	0.077	0.074	0.075

Table 6.2: The mean value and the standard deviation for each distribution of $\Delta M/M$ for sleptons with $\beta_{\rm rec} < 0.9$.
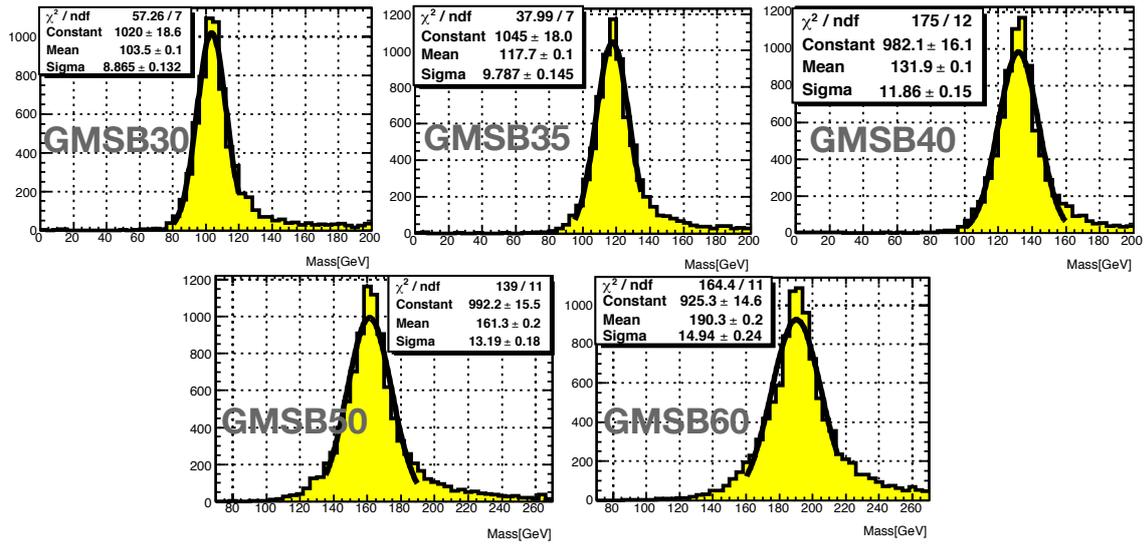
Figure 6.9: The reconstructed mass of sleptons with $\beta_{\text{rec}} < 0.9$ in various GMSB Monte Carlo samples.
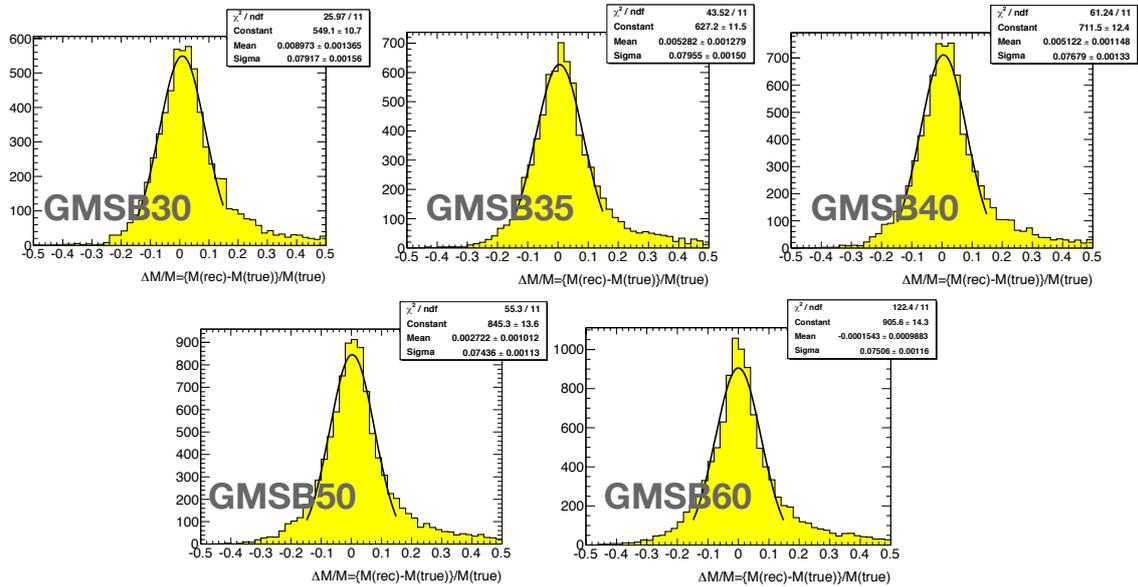

Figure 6.10: The resolution of mass for sleptons with $\beta_{\text{rec}} < 0.9$ in various GMSB Monte Carlo samples.

6.1.3 β mis-reconstruction

Figure 6.11 shows the correlation between the true β and reconstructed β for sleptons in GMSB30 Monte Carlo sample. There are many sleptons with their β reconstructed much lower than the true value.

Figure 6.12 shows the β distribution of muons in a $t\bar{t}$ sample. Since most of muons generated from top decays are running at the speed of light, the tail of the distribution towards lower β value indicates that there are often muons whose β are mis-reconstructed. In the case of muons, β mis-reconstruction may increases the number of background events because it fakes charged SMPs. It is necessary to understand the reason of β mis-reconstruction in order to reject such particles in search for charged SMPs.

Figures 6.13 and 6.14 show the distribution of θ, the angle between the track and the beam direction, for sleptons and muons satisfying with $|\Delta\beta/\beta| > 0.1$. There are four clear peaks at $\theta = 30°, 60°, 120°$ and $150°$. The mis-measurements in these angles are related to the MDT structure. When the β assumption changes, drift circles of the MDT change. In general, if MuonBetaRefitTool fails to measure β, reduced χ^2 for tracking becomes large. However, in the case of slepton tracks running in the direction of the $\theta = 60°$ or $120°$ (barrel regions) or at $30°$ and $150°$ (endcap regions), all radii for tracks are almost the same. Change in the drift radius in all tubes with the same amount do not change the direction of the muon track segment; it change only the position. Therefore, there would be little increase in reduced χ^2 even if β is wrong. An example of the reduced χ^2 as a function of β assumptions for slepton running in the direction of $\theta = 149°$ is shown in Fig. 6.15.

There are two other peaks at the edge of the acceptance, $\theta < 20°$ and $\theta > 160°$. Sleptons running in the direction of these angles are mainly reconstructed using the CSC hits. Since there are smaller number of hits in the MDT tubes and the timing information of the CSC is not used in the β reconstruction with MuonBetaRefitTool, accuracy of the β measurement is worse in these regions.
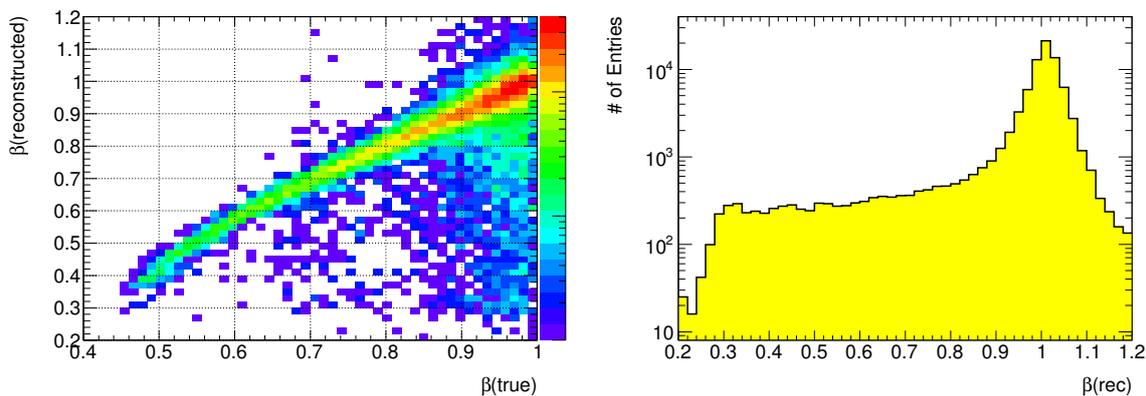

Figure 6.11: The correlation between β_{true} and β_{rec} of sleptons in GMSB30 Monte Carlo sample.

Figure 6.12: β mis-reconstructed muons in $t\bar{t}$ Monte Carlo sample.
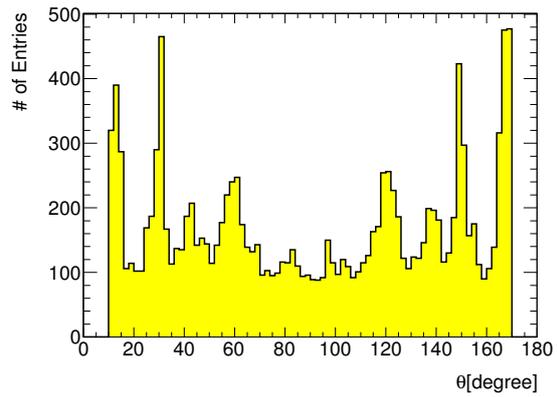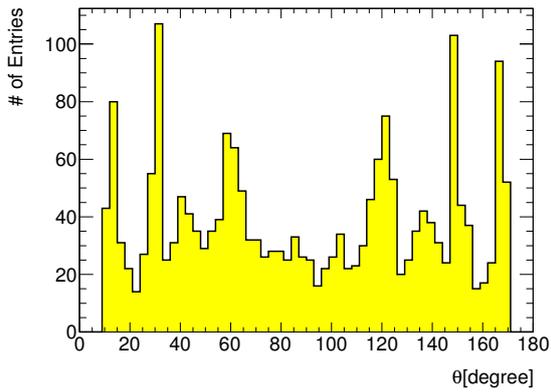
Figure 6.13: The θ distribution of sleptons with $|\Delta\beta/\beta| > 0.1$ in GMSB30 Monte Carlo sample.

Figure 6.14: The θ distribution of muons with $|\Delta\beta/\beta| > 0.1$ in $t\bar{t}$ Monte Carlo sample.
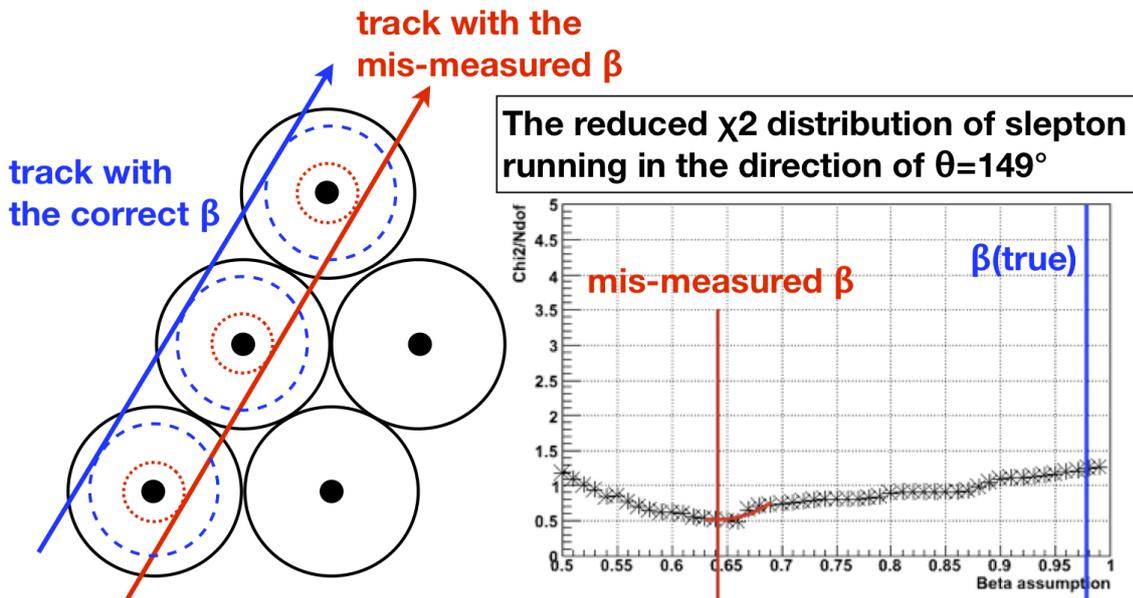

Figure 6.15: A schematic drawing of the drift circles and the track running in the direction of the $\theta = 60°$. The reduced χ^2 distribution of the corresponding track in the direction of $\theta = 149°$, which are reconstructed with mis-measurement β depicted the red line.

6.2   Performance of muon reconstruction in 7 TeV collisions

This section describes the performance of MuonBetaRefitTool evaluated with muons in 7 TeV proton-proton collisions at the LHC.

6.2.1   Data sets

The LHC has started physics run and physics data have been taken. In this study, data collected from August to September 2010 are used. The integrated luminosity is about 3 pb^{-1}. There are muons with $\beta = 1.0$ in the data samples dominantly. Muons reconstructed by MuonBetaRefitTool with $p_T > 10$ GeV and $|\eta| < 2.4$ are used.

Since MuonBetaRefitTool dose not run in the standard event reconstruction chain, it is necessary to re-run the muon tracking algorithms, MOORE and Muid, with MuonBetaRefitTool in order to measure β of muons. The GoodRunList (GRL) produced by the Muon Combined Performance Group is used in order to select events in which the muon spectrometers operate normally. In addition, an updated version of the MDT timing calibration database is used. Imperfect time offset calibration of each drift tube in the MDT stations directly affects the timing reconstruction in MuonBetaRefitTool, as indicated in Eq. 5.6. Figure 6.16 shows the comparison of β measurements with and without the updated version of the MDT timing calibration database. Using this database, the peak position of β distribution for muons shift toward to $\beta \sim 1$. The resolution of β is also improved.
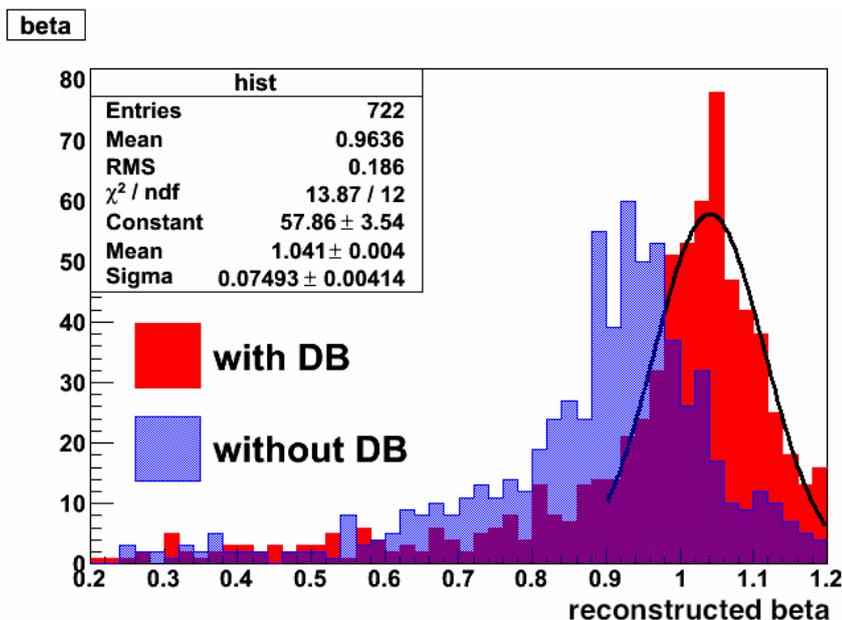

Figure 6.16: The distribution of measured β with and without the updated version of the MDT timing calibration database.

6.2.2 β reconstruction

Figure 6.17 shows the distributions of reconstructed β for muons with $p_T > 10$ GeV and $|\eta| < 2.4$ in 7 TeV collisions. Fitting the β distribution (Fig. 6.17-(a)) with a Gaussian function, the mean value is found to be 1.04 and the width is 0.06. The width is two times larger than that of muons in $t\bar{t}$ Monte Carlo sample (Fig. 6.8) due to imperfect calibration of the MDT. Two figures (b) and (c) in Fig. 6.17 shows the β distributions for the barrel regions ($|\eta| < 1.05$) and the endcap regions ($|\eta| > 1.05$), respectively. In the barrel regions, the mean value is nearly equal to 1.0, however, the resolution is poor. In the endcap regions, although the mean value is larger than 1.0, the resolution is better than that of the barrel regions. The position dependence of the β spectrum can be clearly seen in the two dimensional plot indicated in (d) in Fig. 6.17.
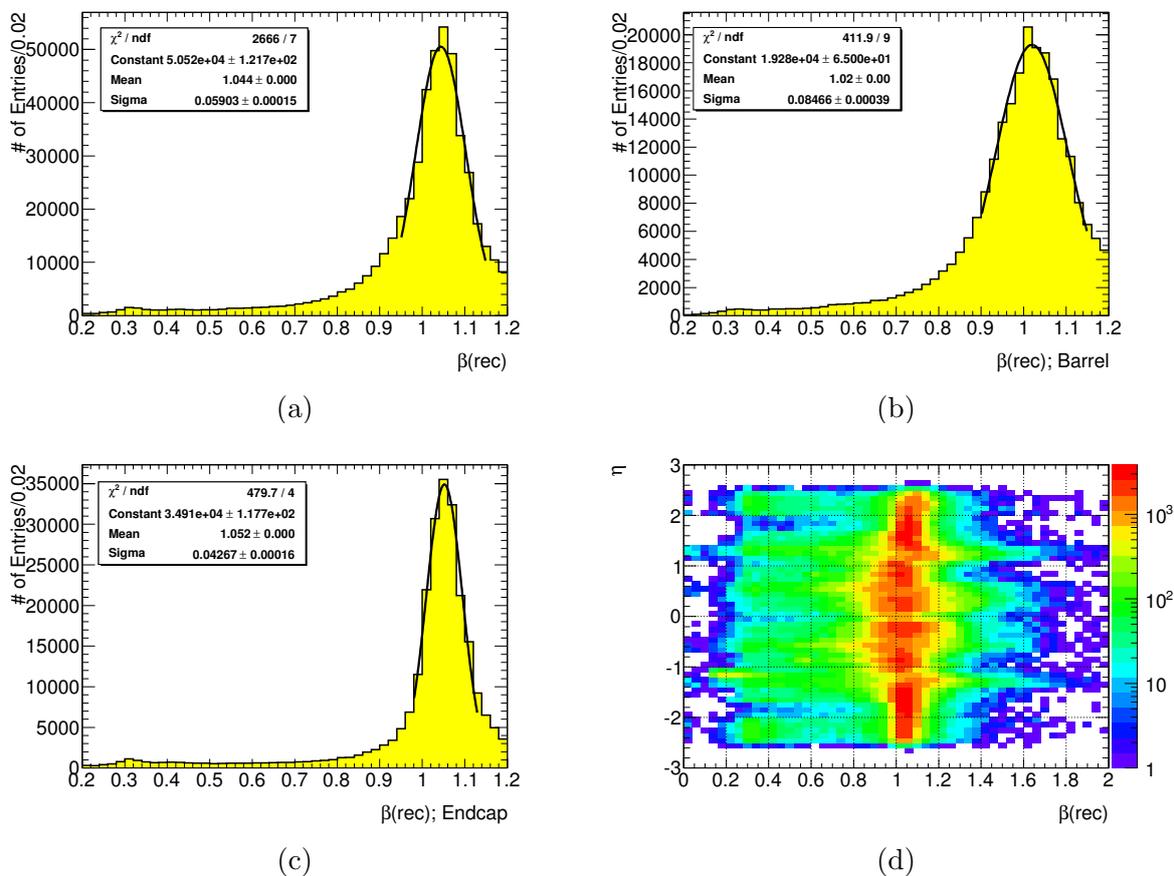

Figure 6.17: Reconstructed β (β_{rec}) distributions for muons with $p_T > 10$ GeV and $|\eta| < 2.4$ in 7 TeV collisions. (a): reconstructed β for muons in all regions. (b): barrel region ($|\eta| < 1.05$). (c): end-cap regions ($|\eta| > 1.05$). (d): correlation between β and η.

6.2.3 β mis-reconstruction

The resolution of reconstructed β for muons in 7 TeV collisions is worse than that in Monte Calro samples. The reason of the mis-reconstruction was further studied using muons with $\beta < 0.7$, where the distribution of reconstructed β becomes flat (Fig. 6.17-(a)) and well away from the peak.

Figure 6.18 shows the θ distribution of muons with $\beta < 0.7$. The shape of the distribution is very similar to that of the Monte Carlo samples. The four peaks at $\theta = 30°, 60°, 120°,$ and $150°$, which are related to the MDT structure, and two other peaks at $\theta < 20°$ and $\theta > 160°$ in the CSC regions are clearly seen. However, the difference from Monte Carlo is that the number of muons at $\theta \sim 150°$ is larger due to the position dependence.
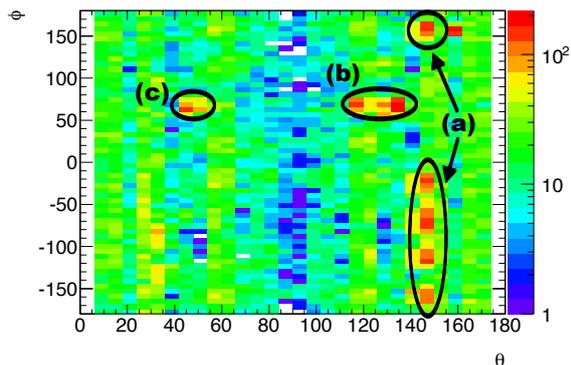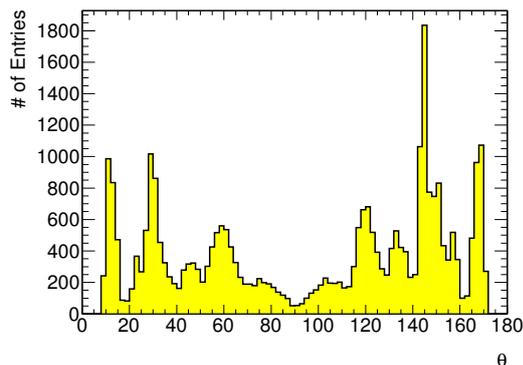

Figure 6.18: The θ distribution for muons with β_{rec} less than 0.7.

Figure 6.19: The correlation between θ and ϕ for muons with $\beta_{\mathrm{rec}} < 0.7$

Figure 6.19 shows the correlation between θ and ϕ for muons with β_{rec} less than 0.7. It shows clear structure in three area, indicated (a), (b) and (c) in Fig. 6.19 where the probability of poorly reconstructed β is high. As mentioned in section 5.1.2, although muon segments with χ^2 minimum are reconstructed using two fitting parameters θ and d in general, the third parameter t_0^{rec} is also used in reconstruction of muon segments in the proton-proton collision events. The parameter t_0^{rec} is the corrected to compensate imperfect timing calibration of each MDT tube. Figure 6.20 shows the distributions of t_0^{shift} defined by t_0^{rec} subtracted by t_0 obtained from the database (t_0^{DB}): $t_0^{\mathrm{shift}} = t_0^{\mathrm{rec}} - t_0^{\mathrm{DB}}$. If t_0 calibrations are done well, t_0^{shift} is almost zero like Fig. 6.20-(d). However, t_0^{shift} distribution for each of three regions indicated in Fig. 6.19 is found to be broader (Fig. 6.20-(a), (b) and (c)). Therefore, the muons reconstructed in the following regions are removed in order to reduce muon backgrounds due to β mis-reconstruction.

- $\theta = 30° \pm 5°, 60° \pm 5°, 120° \pm 5°, 150° \pm 5°$

- $|\eta| > 2.0$

- $140° < \theta < 150°$

- $60° < \phi < 80°$
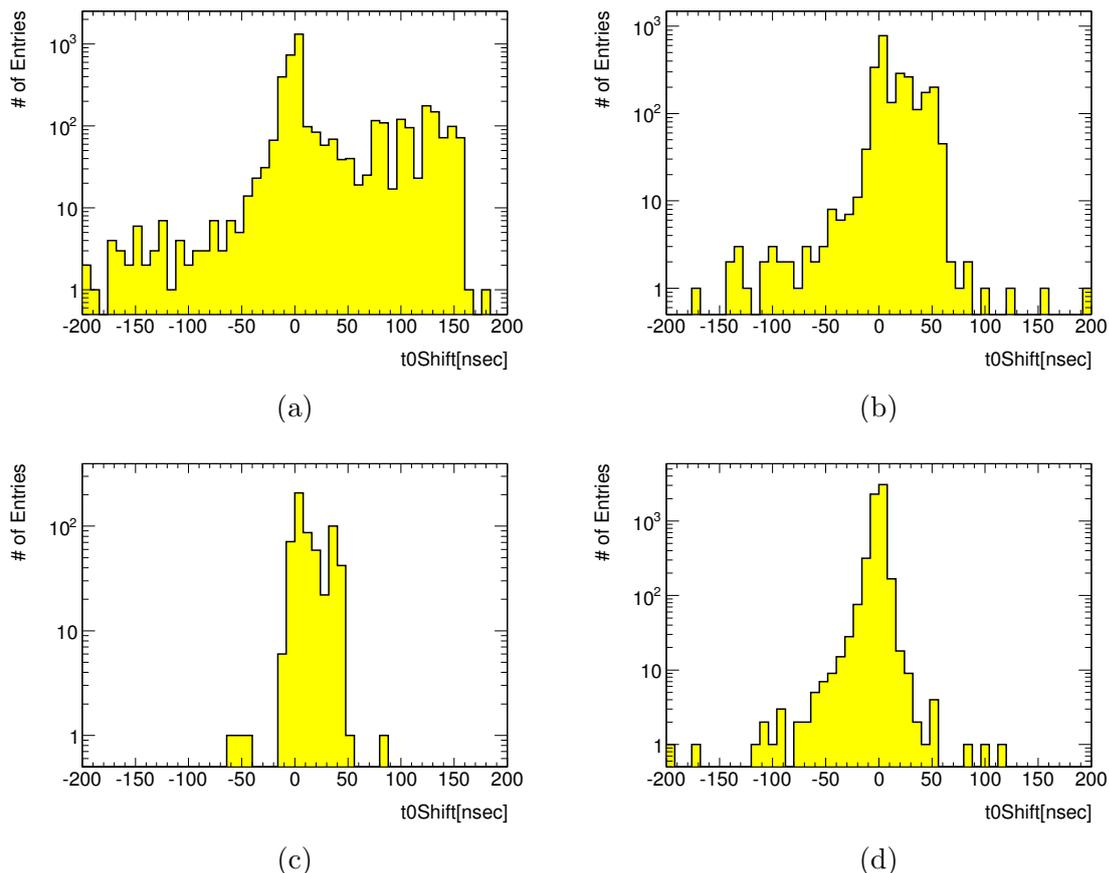
Figure 6.20: The t_0 shift distributions for each region where β are often mis-reconstructed with MuonBetaRefitTool ((a), (b) and (c)). (d) is for muons whose β are successfully reconstructed.

6.2.4 Mass estimation

Figure 6.21 shows the mass distribution for muons with β being reconstructed, $p_T > 10$ GeV and $|\eta| < 2.4$, before the angular cuts described in the previous section. With the angular cuts, the tail in the mass distribution is reduced. However, the remaining muon events still shows a long tail.

Figure 6.22 shows the distribution of the reconstructed mass for the muon sample with $p_T > 10$ GeV and $|\eta| < 2.4$ as a function of η. The long-tail in the mass distribution mainly comes from muons in the direction of the CSC ($|\eta| > 2.0$). In addition, there are also other tails which come from muons running in the direction of the boundary between the barrel and endcap regions ($|\eta| \sim 1$). This is because the number of MDT hits by muons running in these directions is small. MuonBetaRefitTool needs more MDT hits in order to measure β correctly. Mis-measurement of β due to too few MDT hits may cause the long-tail in the mass distribution.

Figure 6.23 shows the correlation between mass and the number of MDT hits. The long-tail comes from muons with the number of MDT hits less than ten. Figure 6.24 shows

the correlation between the pseudo rapidity η and the number of MDT hits for muons with its mis-measured β less than 0.7. It can be confirmed that muons in the CSC regions ($|\eta| > 2.0$) have small number of hits of the MDT clearly. Therefore, further reduction of muon backgrounds will be performed by requiring the number of MDT hits more than ten.

Figure 6.25 shows the mass distribution of muons with and without the angular and the MDT hit selections summarized in Table 6.3. Table 6.4 shows the number of muons with measured mass greater than 50 GeV with and without the selection cuts. The number of background muons is reduced by a factor of about 20.
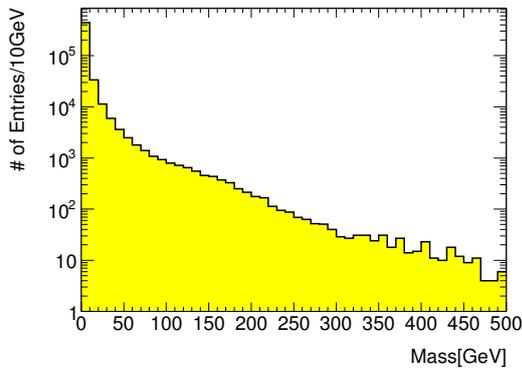
Figure 6.21: Reconstructed mass for muons with $p_T > 10$ GeV and $|\eta| < 2.4$
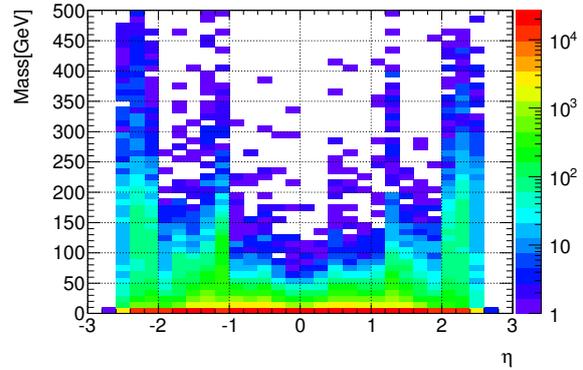
Figure 6.22: The reconstructed mass distribution as a function of η for muon sample with $p_T > 10$ GeV and $|\eta| < 2.4$.
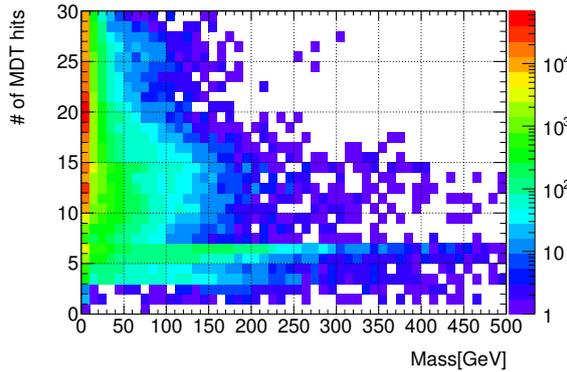
Figure 6.23: The correlation between mass and number of hits of the MDT.
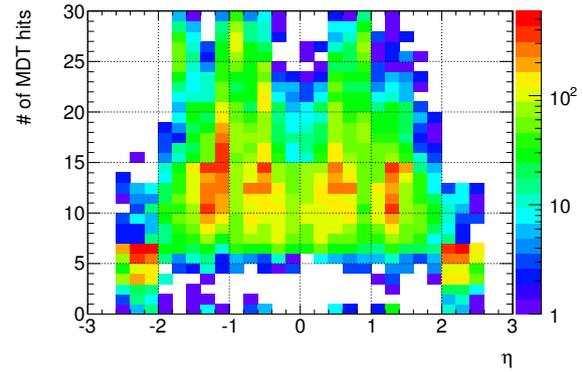
Figure 6.24: The correlation between η and number of hits of the MDT for muons β mis-reconstructed less than 0.7.
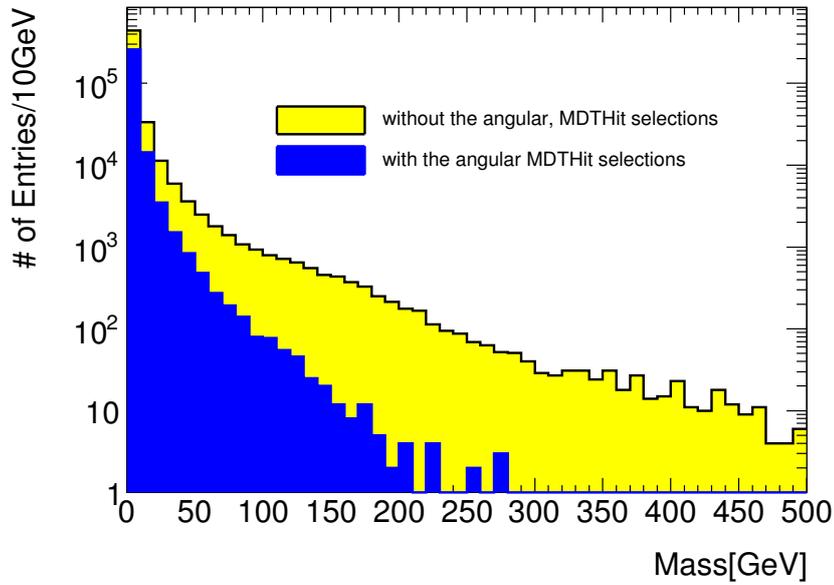
Figure 6.25: The mass distribution of muons with/without the angular and the MDT hit selections.

transverse momentum	$p_T > 10$ GeV is required.
angular cut	$|\eta| < 2.0$ is required.
	$\theta = 30° \pm 5°, 60° \pm 5°, 120° \pm 5°, 150° \pm 5°$ are rejected.
	$140° < \theta < 150°, 60° < \phi < 80°$ are also rejected.
a number of MDT hits	$N_{\text{hits}}^{\text{MDT}} \geq 10$ is required.

Table 6.3: The summary of muon selection criteria.

# of muons without the selection cuts	# of muons with the selection cuts	reduction
6,977	365	$\sim 1/20$

Table 6.4: The reduction of the muon backgrounds.

Chapter 7

Search for charged stable massive particles

Using MuonBetaRefitTool and timing information from Tile Calorimeter, which will be described in this section, search for charged massive stable particles has been performed with 7 TeV proton-proton collision data collected in 2010. Muon backgrounds from the Standard Model processes have been reduced by requiring high-p_T jets and missing transverse energy. No evidence of charged SMPs has been found. Assuming that charged SMPs are generated from the GMSB processes, a 95% C.L. upper limit on the production cross section has been obtained.

7.1 Data and simulation samples

The data samples used for the physics analysis have been collected from July to November in 2010. The total integrated luminosity is 37.4 pb^{-1}. The events were taken by jet triggers as described bellow.

Muon backgrounds were estimated with the Monte Carlo samples. The information for each of the Monte Carlo sample is described in chapter 4 (Tables 4.1 and 4.2).

Figure 7.1 shows a typical SUSY event production and decay including charged SMPs. According to the prediction of the GMSB model, two scalar leptons, which are charged SMPs, are generated in the cascade decays of gluino and/or squarks generated in proton-proton collisions. Multi-jets with high transverse momentum are accompanied because masses of the gluino and squarks are usually more than 500 GeV and much heavier than that of charged SMPs. In addition, when the missing transverse energy is calculated with the Calorimeters and the muon spectrometers, energies of charged SMPs are determined assuming that they are massless particles. The total energy of detectable particles is underestimated because the contributions of masses of charged SMPs are not taken into account correctly. Therefore, the missing transverse energy of events including charged SMPs is large. A search for charged SMPs has been performed by requiring multi high-p_T jets and large missing transverse energy.
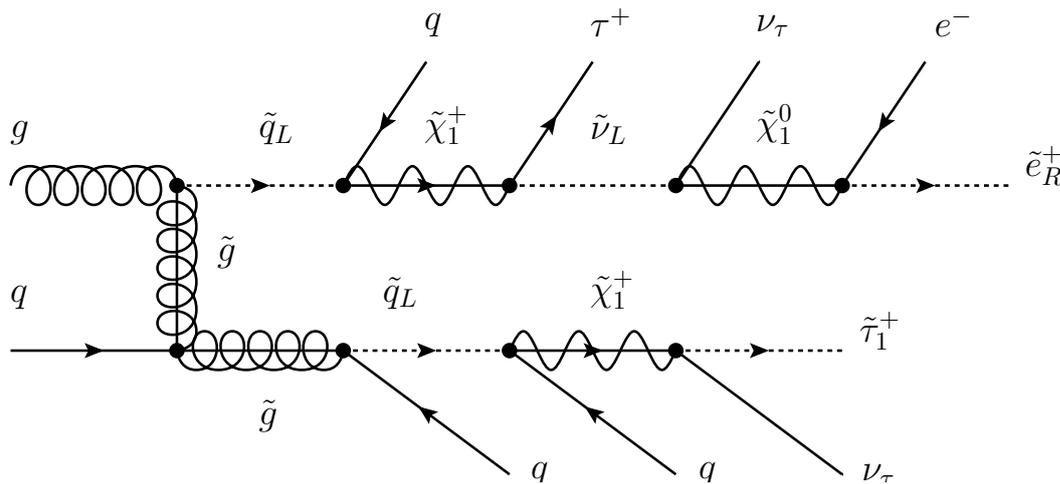
Figure 7.1: A typical decay chain of SUSY events with charged SMPs. Two charged SMPs, $\tilde{\tau}_1^+$ and $\tilde{e}_R^+$, are generated together with three high p_T jets in the cascade decays of gluino $\tilde{g}$ and squark $\tilde{q}_L$, which are generated from proton-proton interaction. In addition, a large missing transverse energy comes from two charged SMPs.

7.2 Trigger requirement

The search for charged SMPs has been performed using data collected with the jet triggers. The reasons why the jet triggers are used in this physics analysis are as follows:

- The muon trigger chambers (the RPC and the TGC) are far from the proton-proton collision points. The trigger decisions are performed within the interval between collisions (25 nsec). Thus, the particles which fires muon triggers are limited by the velocity. When a charged SMP fires the muon trigger, there is the high probability that the velocity of this particle is near $\beta = 1.0$.

- MuonBetaRefitTool, if used in the trigger selection, dose not have sufficient sensitivity to distinguish charged SMPs from large muon background in the range of $\beta > 0.8$ (see Chapter 6). Moreover, the β resolution of muons in 7 TeV collisions is worse than that of Monte Carlo samples as observed from the Gaussian distribution of measured β spreads in $\beta > 0.8$. If the search for charged SMPs are performed in lower β regions (e.g. $\beta < 0.8$), it is necessary to use another triggers.

- As mentioned in the previous section, charged SMPs are generated together with multi high-p_T jets according to the prediction of GMSB model.

In 2010 data taking period, trigger logics are updated with increasing luminosity. Therefore, different trigger branches had to be chosen for charged SMP search depending on the data taking periods. Table 7.1 shows the jet triggers used in this analysis.

Data taking period	Trigger
29 July 2010 – 28 September 2010	L1_J55
28 September 2010 – 18 October 2010	EF_j75_jetNoEF_EFxe20_noMu
24 October 2010 – 29 October 2010	EF_j75_jetNoEF_EFxe25_noMu

Table 7.1: Jet triggers

The LVL1 calorimeter jet trigger L1_J55 selects and records the events which have hit associated jet cluster with the transverse momentum more than 55 GeV in the calorimeter. The efficiency of the L1_J55 trigger is estimated as the number of events which fire both L1_J55 and L1_J5, which is the LVL1 jet trigger and records events including jets with $p_T > 5$ GeV, divided by the total number of events which fire L1_J5 trigger. Figure 7.2 shows the trigger efficiency of L1_J55 as a function of the transverse momentum of the highest p_T jet. The trigger is fully efficient for p_T more than 120 GeV. The plateau efficiency is 98.9 %, obtained by fitting the efficiency ϵ with the following Fermi function:

$$\epsilon = \frac{A}{1 + e^{-a(p_T - b)}}, \tag{7.1}$$

where A, a and b are fitting parameters.

The EF_j75_jetNoEF_EFxe20_noMu (EF_j75_jetNoEF_EFxe25_noMu) trigger is one of the high level triggers recording the events which have jets with $p_T > 75$ GeV and $\not{E}_T > 20$ GeV ($\not{E}_T > 25$ GeV). This trigger is fed by the L1_J55 trigger. As mentioned in previous section, since the events including charged SMPs have multi high-p_T jets and large $\not{E}_T$, these triggers are suitable for this search.

The left side of Fig. 7.3 shows the trigger efficiency of the EF_j75_jetNoEF_EFxe20_noMu trigger as a function of the missing transverse energy. The trigger is fully efficient for $\not{E}_T$ more than 200 GeV. The average of the efficiency is 84.7 % for $\not{E}_T > 50$ GeV. The right side of Fig. 7.3 shows the trigger efficiency as a function of the transverse momentum of the highest p_T jet requiring the missing transverse energy more than 50 GeV. The plateau efficiency is 90.7 %.

Figure 7.4 shows the trigger efficiency of the EF_j75_jetNoEF_EFxe25_noMu trigger as a function of $\not{E}_T$ (a), p_T of the leading highest p_T jet requiring to $\not{E}_T > 50$ GeV (b). The average trigger efficiency is 84.2 % for $\not{E}_T > 50$ GeV. The plateau efficiency in Fig. 7.4-(b) is 88.6 %.
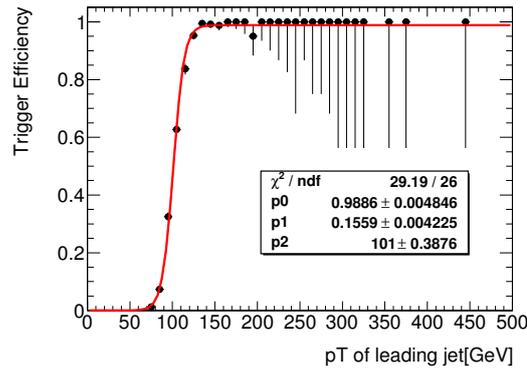
Figure 7.2: The efficiency curve of the L1_J55 trigger.

| (a) | (b) |
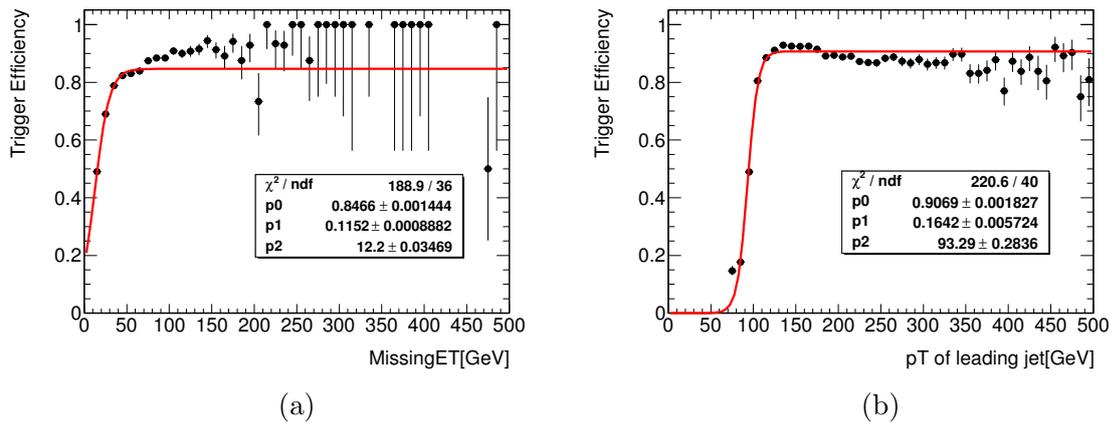
Figure 7.3: (a) The efficiency curve of the EF_j75_jetNoEF_EFxe20_noMu trigger as a function of the missing transverse energy; (b) the transverse momentum of the highest p_T jet (The threshold of $\not{E}_T$ is 50 GeV).

| (a) | (b) |
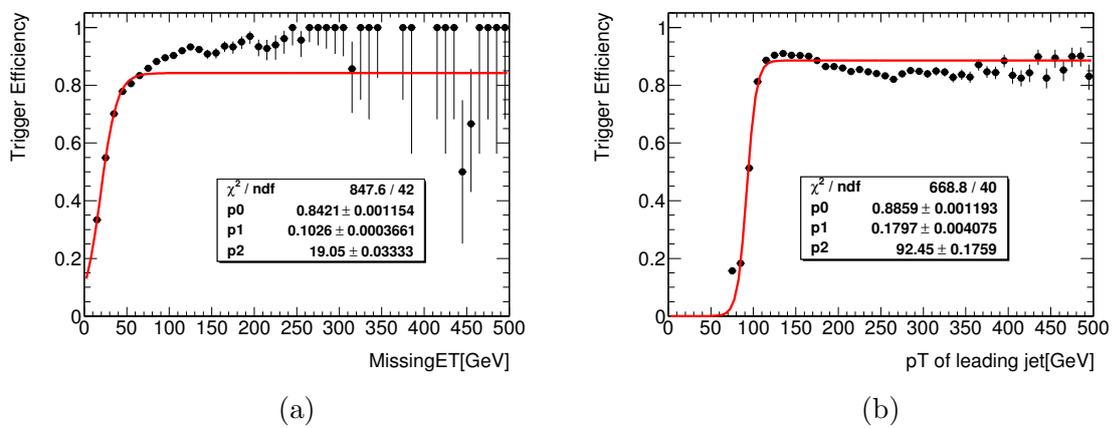
Figure 7.4: (a) The efficiency curve of the EF_j75_jetNoEF_EFxe25_noMu trigger as a function of the missing transverse energy; (b) the transverse momentum of the highest p_T jet (The threshold of $\not{E}_T$ is 50 GeV).

7.3 Object definition

7.3.1 Jets

Jets are reconstructed using the anti-k_T jet algorithm [65] with four-momentum recombination and distance parameter $R = 0.4$ to take into account the large multiplicity. Inputs to the jet algorithm are topological clusters [66] which attempt to reconstruct the three-dimensional shower topology of each particle entering the calorimeter [*1)].

The measured jet transverse momentum p_T^{EMScale}, as determined at the electromagnetic scale [*2)] is corrected for the non-compensating nature of the calorimeter (lower response to hadrons than electrons or photons at the ATLAS calorimeters) and energy losses in inactive regions of the detector (the presence of dead material) using a Monte-Carlo based calibration [67].

7.3.2 Missing transverse energy

The missing transverse energy $\not{E}_T$ in the ATLAS experiments is primarily reconstructed with the energy deposit in the calorimeters and transverse momentum of muon tracks. In this analysis, the $\not{E}_T$ calculation is based on the following vector summation:

$$\vec{\not{E}}_T = \vec{\not{E}}_{T,\,\mathrm{LocHadTopo}} + \vec{\not{E}}_{T,\,\mathrm{Muon}} - \vec{\not{E}}_{T,\,\mathrm{energy\ loss}} \tag{7.2}$$

where $\not{E}_{T,\,\mathrm{LocHadTopo}}$ is the missing transverse energy calculated with the topological clusters calibrated to locally electromagnetic and hadronic scale depending on the energy loss classification. The second term $\not{E}_{T,\,\mathrm{Muon}}$ is calculated as the sum of the following two components: sum of muon momentum of all isolated combined muons and muons in holes ($|\eta| \sim 0$), and sum of all non-isolated muons reconstructed as tracks in the muon spectrometers. The third term $\not{E}_{T,\,\mathrm{energy\ loss}}$ is sum of calorimeter cell energies traversed by isolated muons. The third term is subtracted from the sum of the first two to avoid double-counting of the energy loss already taken into account by the combined muon momentum.

7.3.3 SMP candidates

In this search, muons are defined as combined muons reconstructed with the Muid and their β with MuonBetaRefitTool in $|\eta| < 2.4$. In addition, the transverse momentum (p_T) should be more than 20 GeV, and the total calorimeter energy within a cone of radius $\Delta R = 0.2$ around the muon ($E_T^{\mathrm{cone0.2}}$) should be less than 10 GeV in order to select isolated high-p_T muons.

[*1)] The constituents of jets are groups of calorimeter readout cells from energy deposits induced by particles. The energy deposits are grouped in topological clusters. Topological clusters are developed around calorimeter cells (called seed cells) whose signal-to-noise ratio, which is estimated as the energy deposited in the cell over the RMS of the energy distribution measured in random events, is above a threshold of 4. Cells neighboring the seed that have a signal-to-noise ratio of at least 2 are then included iteratively. Finally, all neighboring cells are added to the topological clusters.

[*2)] The energy of reconstructed jets is calibrated to the energy scale measured by the calorimeters, called the electromagnetic (EM) scale. The EM scale is established using test-beam measurements for electrons and muons in the electromagnetic and hadronic calorimeters, whose calibration factor converts the calorimeter signals, measured as electric charge in pC, to the energy deposited by electrons, which would produce these signals. This energy scale accounts for the energy of electrons and photons correctly. (see Ref. [68])

7.4 β measurement with the Tile Calorimeter

The Tile Calorimeter measures the time of the energy deposition in each cell traversed by particles from the proton-proton collision point. The velocity β can be measured by using the cells of the Tile Calorimeter cluster associated with the muon tracks. In this thesis, the velocity β of charged SMPs has also been measured by the time-of-flight information of the Tile Calorimeter. The merits of measuring β with the Tile Calorimeter are as follows:

- Further reduction of the muon backgrounds are expected by requiring a coincidence of two independent β measurements.

- The measured β with MuonBetaRefitTool can be cross-checked with the measured β by using the Tile Calorimeter.

- The regions where MuonBetaRefitTool often mis-measures β (see Chapter 6) can be recovered by measuring correct β with the Tile Calorimeter.

This section describes the algorithm for determing β of clusters with the Tile Calorimeter. More detailed information can be found elsewhere [69].

7.4.1 The method of β measurement using the TOF information of Tile Calorimeter

At the ATLAS Tile Calorimeter, the cell time (t_{cell}), which is the energy deposition time offset with the arrival time of particle running at the speed of light, is given by:

$$t_{\mathrm{cell}} = t_{\mathrm{meas}} - \frac{d_{\mathrm{cell}}}{c},$$ (7.3)

where t_{meas} is the measured time when a particle generated from proton-proton collisions deposit their momentum in the cell, d_{cell} is the distance between the center of the cell and the interaction point, and c is the speed of light. It is expected that, for cells traversed by muons traveling with $\beta \simeq 1.0$, t_{cell} will have small values with an average at zero. In contrast, for cells with sufficient energy deposit from charged SMPs, t_{cell} will have large values depending on the speed of the particle and the distance between the cell and the interaction point. Figure 7.5 shows the distributions of reconstructed cell time of muons in $t\bar{t}$ Monte Carlo sample (a) and sleptons in GMSB30 Monte Carlo sample (b).

The reconstructed speed β_{cell} for each cell traversed by a muon or a charged SMP is calculated using the cell time t_{cell} with the following formula:

$$\beta_{\mathrm{cell}} = \frac{v}{c} = \frac{d_{\mathrm{cell}}}{t_{\mathrm{meas}}c} = \frac{d_{\mathrm{cell}}}{(t_{\mathrm{cell}} + \frac{d_{\mathrm{cell}}}{c})c} = \frac{d_{\mathrm{cell}}}{t_{\mathrm{cell}}c + d_{\mathrm{cell}}}$$ (7.4)

Employing the weighted average with the cell energies, β_{tile} of a muon track is determined:

$$\beta_{\mathrm{tile}} = \frac{\sum_{i=1}^{n} E_i \beta_i}{\sum_{i=1}^{n} E_i},$$ (7.5)

where n is the number of cells associated with the muon track in the Tile Calorimeter and E_i is the energy deposition in each cell.
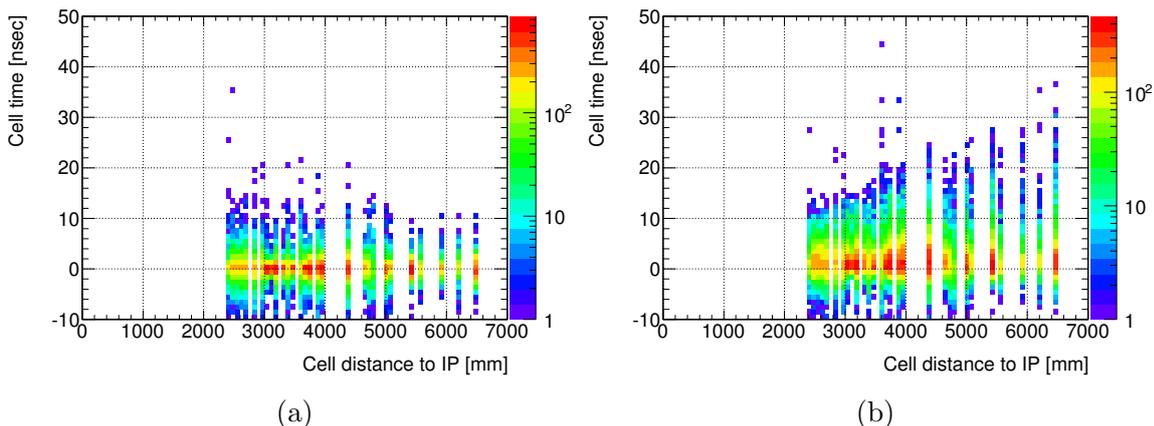
Figure 7.5: The simulated distributions of reconstructed cell time t_{cell} for muons in $t\bar{t}$ Monte Carlo sample (a) and sleptons in GMSB30 Monte Carlo sample (b).

7.4.2   Performance of β measurement

Figure 7.6 shows the distribution of measured β value with the Tile Calorimeter β_{tile} and MuonBetaRefitTool β_{refit}, the correlation between β_{tile} and the energy of calorimeter cluster associated with the muon tracks, and the correlation between β_{refit} and β_{tile} for muons in 7 TeV collisions satisfying the muon definition described in the previous section and the selection criteria described in section 6.2 in order to reject muons in the regions where MuonBetaRefitTool often mis-measures β. Note that the absolute value of the pseudorapidity less than 1.7 is required due to the acceptance of the Tile Calorimeter. From these figures, it can be concluded that;

- the resolution of measured β with MuonBetaRefitTool is better than that of the Tile Calorimeter (Fig. 7.6-(a) and (b)). However, there are clear tail in the region of $\beta < 0.8$ due to β mis-measurement by MuonBetaRefitTool (Fig. 7.6-(c) and (d)).

- The β of muons mis-measured with MuonBetaRefitTool may be recovered correctly with the Tile Calorimeter (Fig. 7.6-(e)).

- The velocity β is measured correctly and the resolution is better when the total energy deposit in the calorimeter is large. (Fig. 7.6-(f)).

7.4.3 β mis-measurement due to the cells with negative β_{cell}

Figure 7.7 shows the distribution of β_{cell}. From this distribution, it can be found that there are cells with negative β_{cell}. When a denominator of Eq. 7.4, $t_{\text{cell}}c + d_{\text{cell}}$, takes a negative value due to wrong measurement of t_{cell} for any reason (e.g. imperfect timing calibration of cells in Tile Calorimeter), a cell with negative β_{cell} appears. If a muon track is associated with a cell with negative β_{cell} and the contribution from the cell is large in calculation of β_{tile}, there is the possibility that β_{tile} takes a median value (e.g. $0.5 < \beta_{\text{tile}} < 0.8$) and the muon track becomes a signal candidate. Figure 7.8 shows the correlation between β_{tile} and β_{cell}. Although the number is very small, there are muons satisfying such situation. To
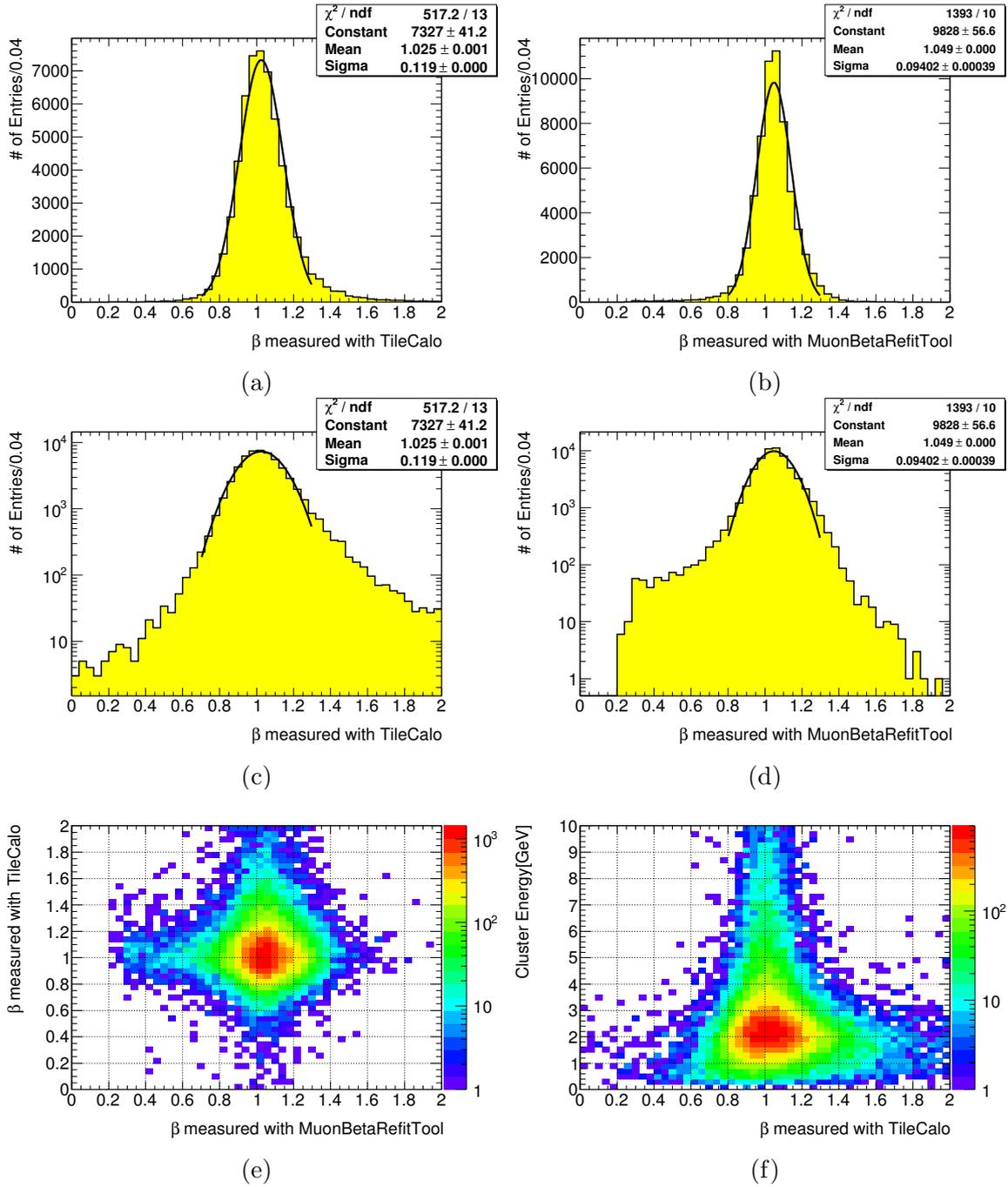
Figure 7.6: (a); The distribution of measured β with the Tile Calorimeter, (b); Muon-BetaRefitTool, (c); the distribution (log scale) of measured β with the Tile Calorimeter, (c); MuonBetaRefitTool, (e); the correlation between β_{refit} and β_{tile}, (f); the correlation between β_{tile} and the energy of calorimeter cluster associated with the muon tracks.

avoid the muon backgrounds due to the cells with negative β_{cell}, muon tracks associated with the cells whose β_{cell} takes a negative value are rejected. In addition, the number of cells associated with muon tracks are required to be more than two in order to keep the accuracy of β_{tile} measurements.
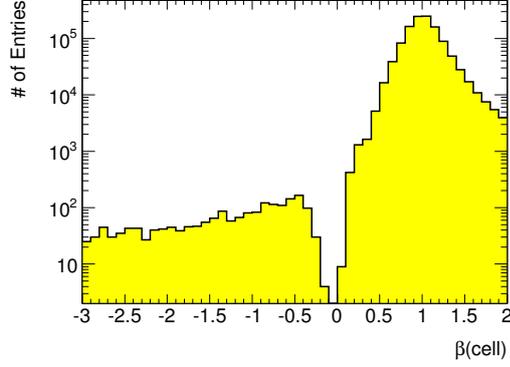

Figure 7.7: The distribution of β_{cell}.
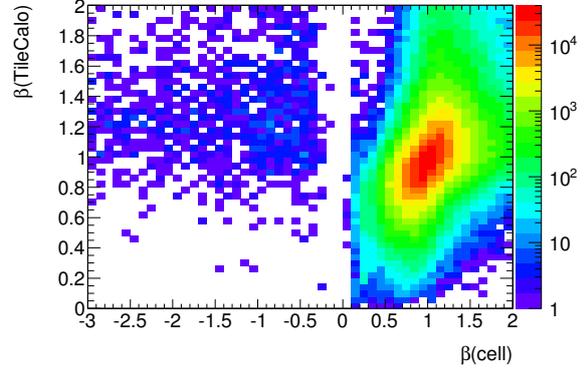
Figure 7.8: The correlation between β_{cell} and β_{tile}.

7.5   Correction on the velocity β

The peak positions of measured β distributions with the two types of β measurement methods, MuonBetaRefitTool and Tile Calorimeter, shift towards larger values. The shift affects the mass determination for charged SMPs. Therefore, a correction method for the β shift was developed.

An arrival time of particles from the proton-proton interaction point to a hit position in the MDT or the Tile Calorimeter is represented as follows:

$$t = \frac{d}{\beta c}, \tag{7.6}$$

where d is the distance between the proton-proton interaction point and a hit. The timing shift Δt is defined as:

$$\Delta t = t(\beta = 1.0) - t(\beta_{\text{rec}}) = \frac{d}{c} - \frac{d}{\beta_{\text{rec}} c}, \tag{7.7}$$

where $t(\beta = 1.0)$ is the expected arrival time with the assumption of $\beta = 1.0$ and $t(\beta_{\text{rec}})$ is the real arrival time. Using data samples collected with the muon triggers, Δt was calculated for each muon track using both MuonBetaRefitTool and the Tile Calorimeter. To obtain the d value, the average distance calculated with the hit positions ($x_{\text{hit}}, y_{\text{hit}}, z_{\text{hit}}$) associated to the combined muon track in each detector is used:

$$d = \sum_{i=1}^{N} \frac{\sqrt{x_{\text{hit},i}^2 + y_{\text{hit},i}^2 + z_{\text{hit},i}^2}}{N}, \tag{7.8}$$
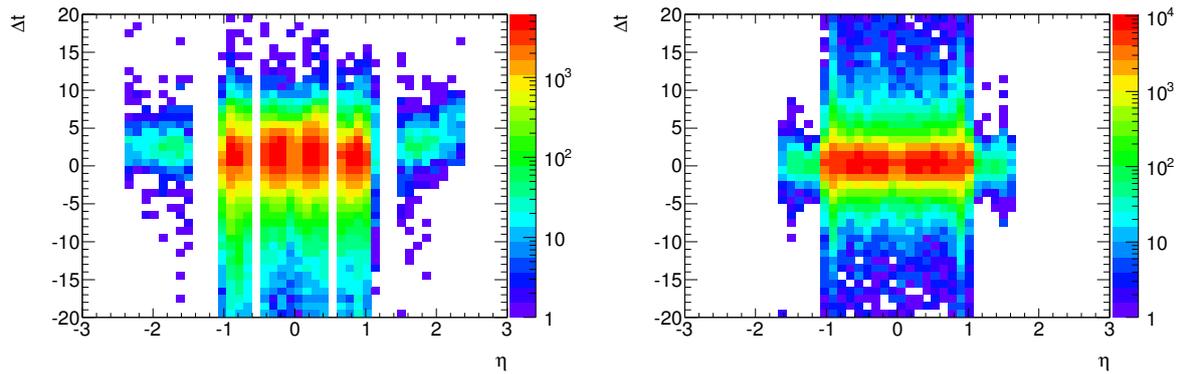
Figure 7.9: The timing shift Δt [nsec] in terms of pseudorapidity η for the MDT (left) and the Tile Calorimeter (right).
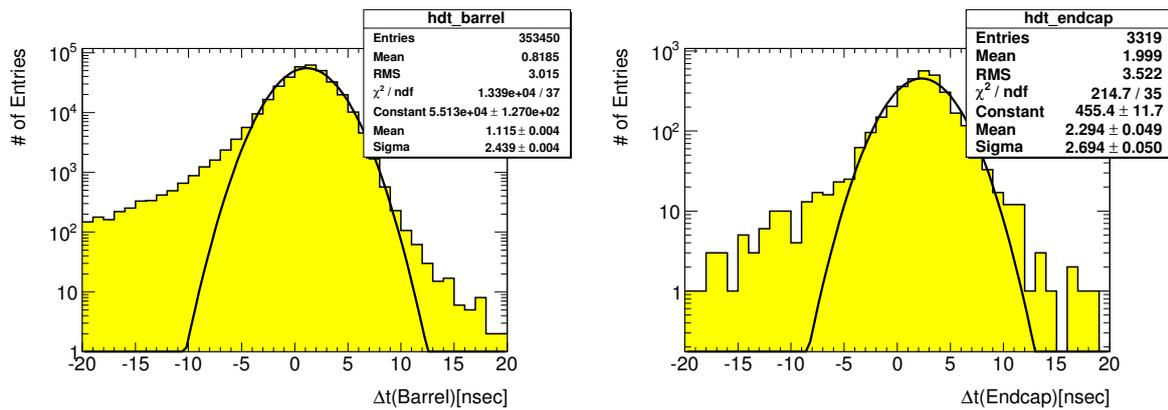

Figure 7.10: The distribution of timing shift Δt for the MDT in the Barrel (left) and the Endcap (right) regions.
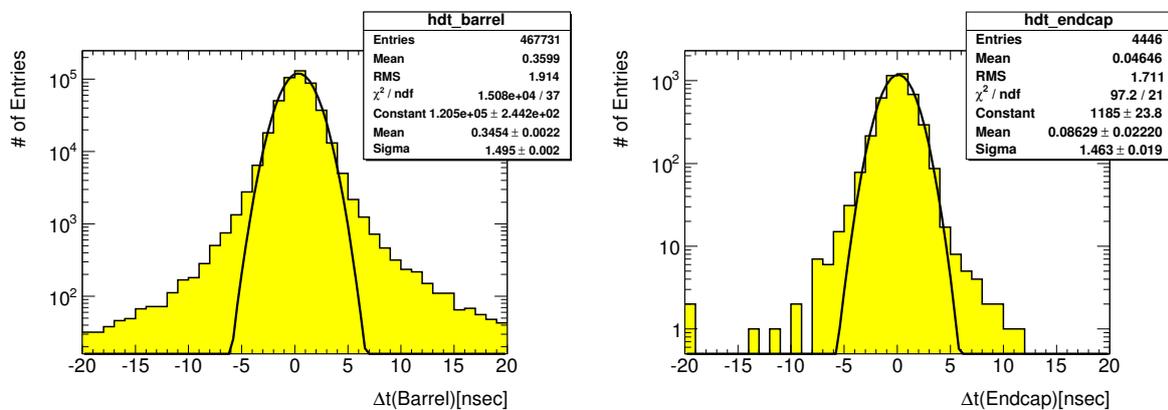

Figure 7.11: The distribution of timing shift Δt for the Tile Calorimeter in the Barrel (left) and the Endcap (right) regions.

where N is the total number of hits in each detector.

Figure 7.9 shows the timing shift Δt in terms of pseudorapidity η for the MDT and the Tile Calorimeter. From these distributions, it is found that Δt depends on η. Therefore, timing shift Δt is parametrized separately for barrel and endcap regions.

Figures 7.10 and 7.11 are the distributions of Δt for the MDT and the Tile Calorimeter, respectively. The mean value of each distribution is taken as the correction factor of timing shift, because the Gaussian function is not fit to each distribution of Δt well. Table 7.2 shows the timing shift for the barrel and endcap regions, respectively.

	MDT	Tile Calorimeter
Barrle ($|\eta| < 1.05$)	+0.89 nsec	+0.36 nsec
Endcap ($|\eta| \geq 1.05$)	+2.00 nsec	+0.05 nsec

Table 7.2: The correction factor for timimg of the MDT and the Tile Calorimeter.

The corrected velocity $\beta_{\text{corrected}}$ can be determined with the timing shift Δt as follows:

$$\beta_{\text{corrected}} = \frac{d}{c(t + \Delta t)}. \tag{7.9}$$

The shift of β, $\Delta\beta$, is defined as:

$$\Delta\beta = \beta_{\text{corrected}} - \beta_{\text{rec}}, \tag{7.10}$$

and is determined by using data samples. Figures 7.12 and 7.13 show the distributions of $\Delta\beta$ for MuonBetaRefitTool and TileCalorimeter. Since the Gaussian function is not fit to each distribution of $\Delta\beta$ well, the mean value of each distribution is taken as the correction factor of β. Table 7.3 shows the correction factor of measured β for each measurement method.
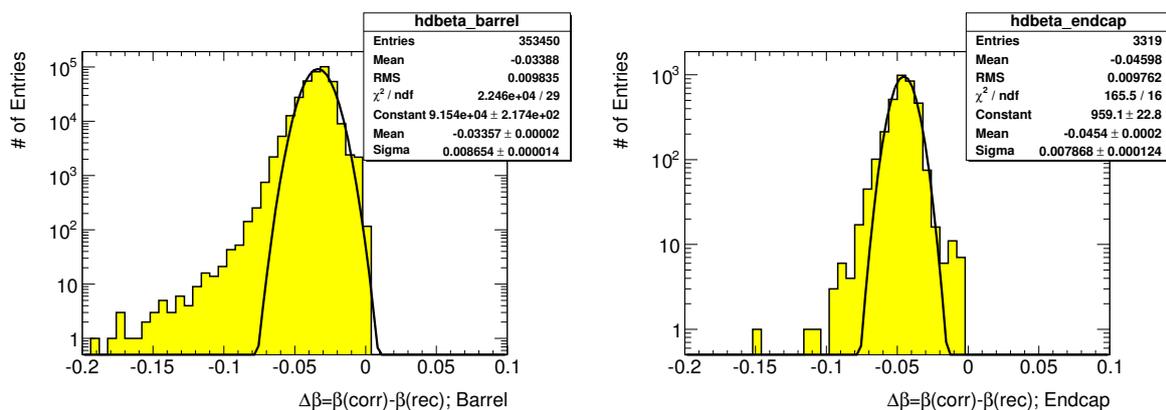
Figure 7.12: The shift of measured β with MuonBetaRefitTool in Barrel (left) and Endcap (right) regions.

Figure 7.14 shows the distribution of β with and without the timing shift correction for each measurement method. Table 7.4 shows the mean value and resolution for each β
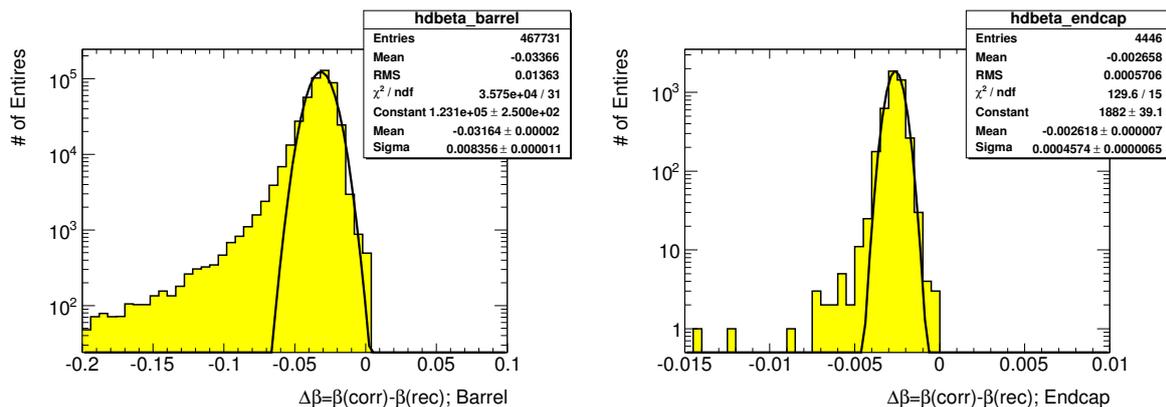
Figure 7.13: The shift of measured β with Tile Calorimeter in Barrel (left) and Endcap (right) regions.

	MuonBetaRefitTool	Tile Calorimeter
Barrle ($|\eta| < 1.05$)	-0.034	-0.034
Endcap ($|\eta| \geq 1.05$)	-0.046	-0.003

Table 7.3: The correction factor of measured β for two types of β measurement methods, MuonBetaRefitTool and Tile Calorimeter.

distribution with and without the correction. It is found that the peak position for each measured β distribution shifts toward $\beta = 1.0$.
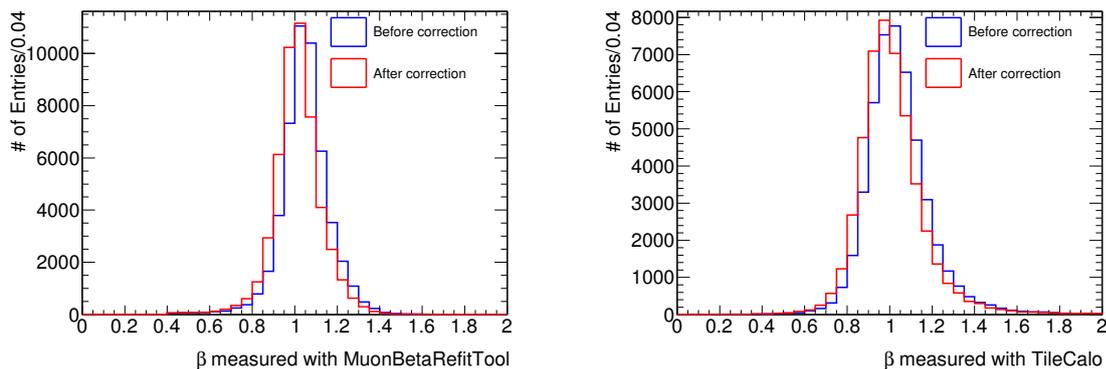
Figure 7.14: The distribution of β with and without β shift correction.

7.6 Event Selection

Charged SMPs are assumed to be generated by GMSB processes. According to the prediction of the GMSB model, two charged SMPs are generated in the cascade decays of gluinos and/or squarks, which are generated by proton-proton interactions, under R-parity conser-

	MuonBetaRefitTool		Tile Calorimeter	
	before	after	before	after
mean	1.044	1.012	1.018	0.987
resolution	0.087	0.088	0.110	0.113

Table 7.4: The mean value and resolution of β with and without β shift correction.

vation. Since the GMSB model predicts that the mass scales of squark and gluino in the GMSB model are more than 500 GeV, it is expected that the signal events have at least two high-p_T jets. In addition, since energies of charged SMPs are calculated assuming that they are massless particles in reconstruction of missing transverse energy, the total energy of detectable particles is to be underestimated. Therefore, events including charged SMPs are also expected to have large missing transverse energy.

7.6.1   Pre-selection

Interesting events are preselected from a very large number of events using the following criteria:

- There are more than two jets in $|\eta| < 2.5$.

- The first and second jets are defined as jets with the largest and the second largest transverse momentum, respectively. They are required to have $p_T^{\mathrm{1stJet}} > 70$ GeV and $p_T^{\mathrm{2ndJet}} > 30$ GeV.

7.6.2   Event selection

After pre-selection, events used for physics analysis are selected with the following criteria. Although charged SMPs are assumed to be generated by the GMSB processes, in general, they are predicted in many models beyond the Standard Model. Therefore, the requirements on jets and missing transverse energy are kept looser than those used in the standard supersymmetry analyses in ATLAS.

- The appropriate jet-trigger (see section 7.2) is fired.

- The missing transverse energy $\not{E}_T$ is required to be more than 50 GeV.

- The events has at least two jets with $p_T^{\mathrm{1stJet}} > 120$ GeV and $p_T^{\mathrm{2ndJet}} > 50$ GeV and in the region $|\eta| < 2.5$.

7.6.3   Charged SMP selection

Charged SMPs reach the muon spectrometers and behave as heavy muons. Events containing at least one combined muon track satisfying following criteria are selected.

- The track is required to have $|z_0 - z_{\mathrm{pv}}| < 20$ mm, where z_0 is the impact parameter and z_{pv} is z coordinate of the primary vertex, in order to reject cosmic muons.

- The transverse momentum is required to be $p_T^{\text{track}} > 20$ GeV.

- The pseudorapidity is required to be $|\eta| < 1.7$ because the Tile Calorimeter covers only this range.

- More than two cells are required to be associated with the combined muon track in the Tile Calorimeter.

- Muon tracks with cells whose β_{cell} takes negative value are rejected. (see section 7.4)

- The velocity β of the combined muon track is measured with MuonBetaRefitTool and the Tile Calorimeter.

- Since MuonBetaRefitTool have no sufficient sensitivity to charged SMPs with $\beta < 0.4$ due to energy loss in the calorimeters (see section 6.1.1), β to be more than 0.4 is required.

- The number of MDT hits is more than 10 because it is highly possible that Muon-BetaRefitTool often mis-reconstructs β of muon tracks with the number of MDT hits less than 10 (see section 6.2).

- Muons running in the direction of $140° < \theta < 145°$ or $60° < \phi < 80°$ are rejected due to the imperfect calibration of the MDT time offset (see section 6.2).

- Muons running in the direction of $\theta = 30° \pm 5°, 60° \pm 5°, 120° \pm 5°$ and $150° \pm 5°$, where MuonBetaRefitTool often mis-measures β, are also rejected (see section 6.2).

7.7   Normalization of the QCD backgrounds

Since PYTHIA QCD calculation is accurate only to leading order in the strong coupling constant, it is not expected to correctly describe absolute normalization of the QCD cross section. Therefore, the QCD sample was normalized using the number of events passing the event selection with the trigger, $\not{E}_T$ and jets described in section 7.6.2. Note that the muon selection was not applied. Events passing the selection are dominated by the QCD events. Contributions from other processes, W/Z and $t\bar{t}$, are much smaller and do not affect the normalization at this level. Therefore, this sample is not sensitive to the normalization of these processes, which are left as predicted by the models.

The total numbers of events in data and the QCD Monte Carlo sample are 102813 and 117752, respectively. The normalization factor is 0.87, which is applied to all the QCD di-jets samples to obtain the QCD expectations.

Figure 7.15 shows $\not{E}_T$, p_T^{1stJet} and p_T^{2ndJet} distributions after the normalization. The normalized QCD Monte Carlo samples provide good descriptions of shapes of the missing transverse energy and the transverse momentum distributions of the first and the second jets in data.

Data	QCD MC sample	factor
102813	117752	0.87

Table 7.5: The normalization factor of QCD Monte Carlo sample.

(a)

(b)

(c)
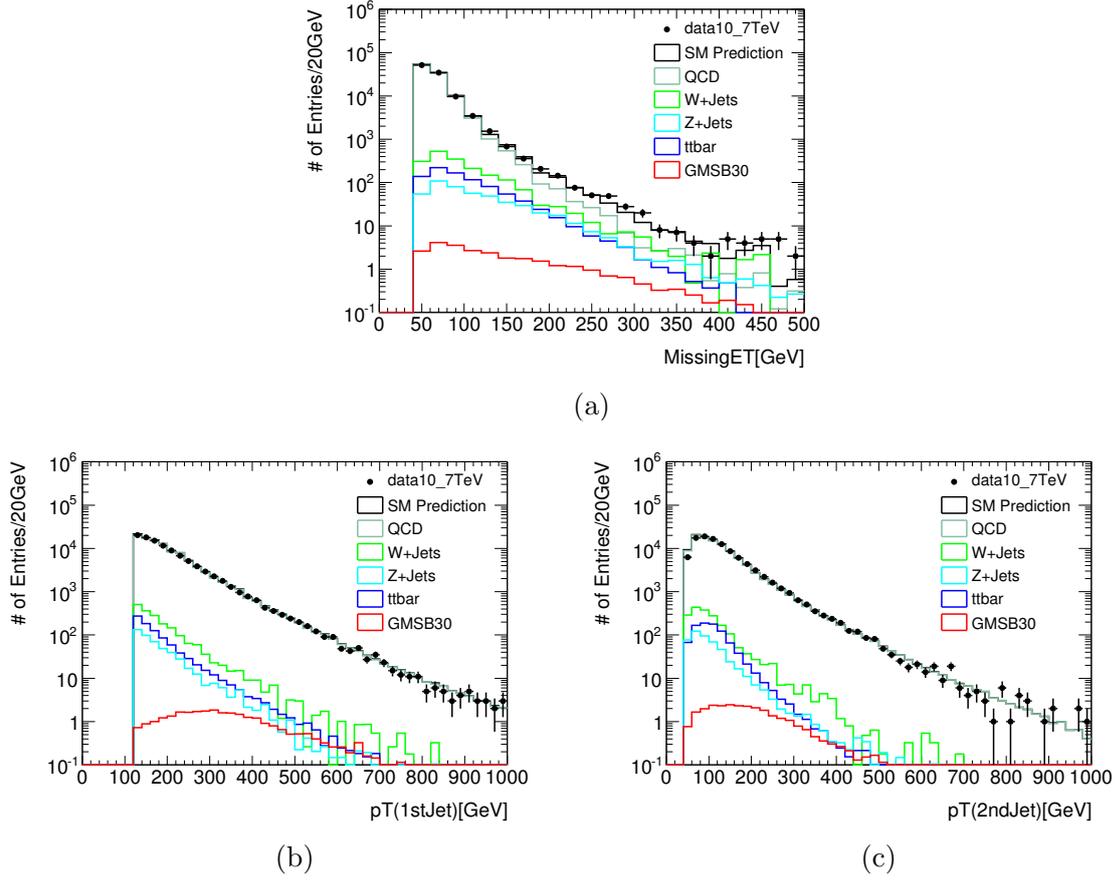
Figure 7.15: The missing transverse energy (a) and transverse momentum of 1st jet (b) and 2nd jet (c) distributions.

Figure 7.16 shows the number of muons per event, pseudorapidity η, azimuthal angle ϕ and transverse momentum p_T for muons satisfying the following selection criteria, which are looser than those in the charged SMP selection described in section 7.6.3:

- $|z_0 - z_{\mathrm{pv}}| < 20$ mm

- $|\eta| < 2.0$

- $p_T > 10$ GeV

- $E_T^{\mathrm{cone0.2}} < 10$ GeV

- Number of MDT hits is more than ten.

- Muons running in the direction of $140° < \theta < 145°$ or $60° < \phi < 80°$ are rejected.

- Muons running in the direction of $\theta = 30° \pm 5°, 60° \pm 5°, 120° \pm 5°$ and $150° \pm 5°$ are rejected.

Here the QCD sample is normalized by the factor 0.87. Contribution of the QCD events becomes very small by requiring muons. Although the Monte Carlo samples overestimate the total number of muons, they estimate the number of events with muons well. The Monte Carlo samples can describe the shape of each distribution (η, ϕ and p_T^{track}) reasonably well.
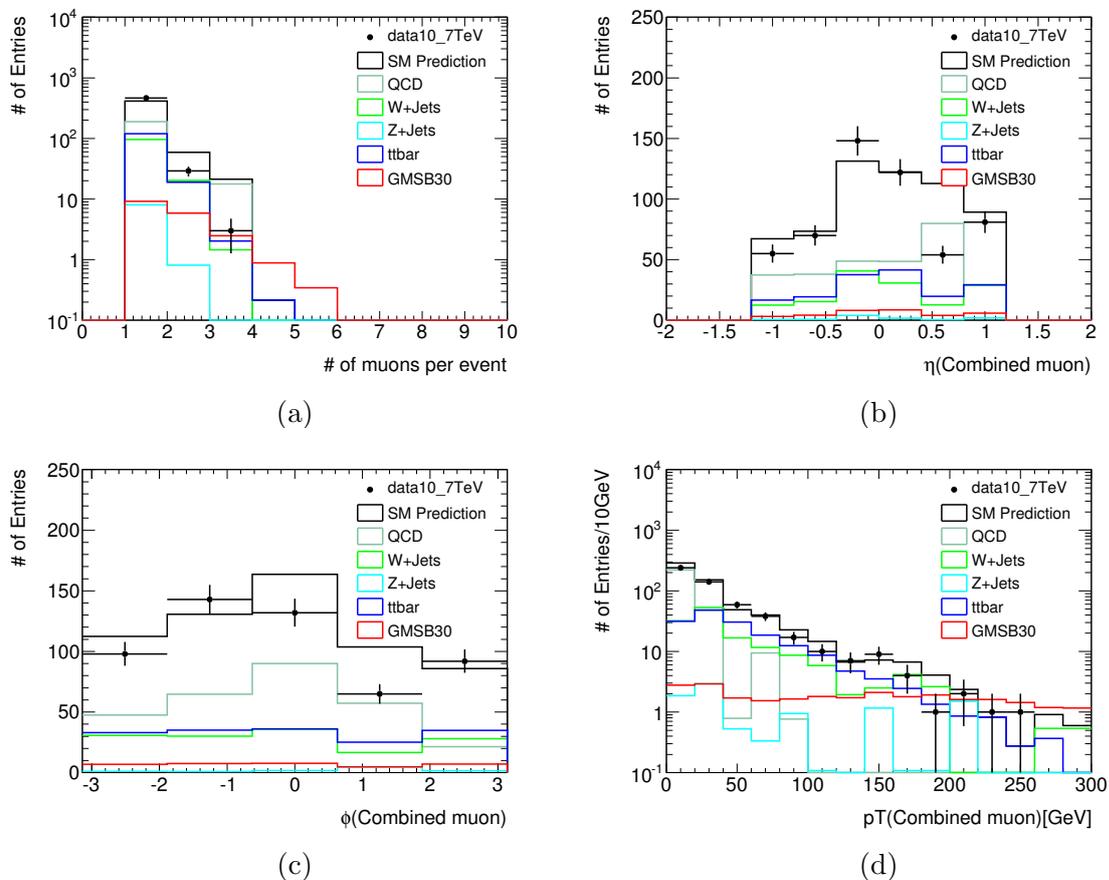
Figure 7.16: (a): The number of muons per event, (b): pseudorapidity η, (c): azimuthal angle ϕ, (d) transverse momentum p_T^{track} for muons satisfying the selection described above.

	Data	Monte Carlo
# of events after event selections	102,813	$106,039 \pm 326$
# of events after event and muon selections	495	494 ± 22
# of muons	530	596 ± 24

Table 7.6: The number of events passing the event and muon selections described above, for data and for the Monte Carlo samples normalized to the same integrated luminosity.

7.8 Event properties of the signal sample before final selection

From this section, results of a search for charged SMPs with data, corresponding to an integrated luminosity is 37.4 pb^{-1}, are described. Distribution of kinematical variables for these events are shown.

Table 7.7 shows (1) the number of events passing the event selections, which consists of jet trigger, missing transverse energy and jet selections, (2) the number of events which have charged SMP candidates satisfying the charged SMP selection criteria, and (3) the total number of charged SMP candidates for the data and the prediction from the Monte Carlo samples. The QCD Monte Carlo samples have been normalized in a way described in section 7.7. The Monte Carlo simulation can describe the number of observed events and charged SMP candidates well.

	Data	Monte Carlo
# of events after event selections	102,813	$106,039 \pm 326$
# of events after event and charged SMP selections	273	268 ± 16
# of charged SMP candidates	290	301 ± 17

Table 7.7: The number of events passing the event and charged SMP selections described in section 7.6.2, for data and for the Monte Carlo samples normalized to the same integrated luminosity.

Figure 7.17 shows the missing transverse energy (a), transverse momentum of first jet (b) and second jet (c). The Monte Carlo sample describes the shapes of three types of the distributions reasonably well. Requiring at least one muon, contributions of $W^{\pm}$ bosons and $t\bar{t}$ production become as large as that of QCD events. In the case of the missing transverse energy, for the instance, contribution of the QCD events is larger than others up to $\not{E}_T = 100$ GeV. However, the contributions from $W^{\pm}$ and $t\bar{t}$ dominate in the region $\not{E}_T > 100$ GeV.

The velocity β of charged SMP candidates are measured with MuonBetaRefitTool and the Tile Calorimeter. The Monte Carlo samples can also describe the shapes of the distributions for charged SMP candidates reasonably well. Figure 7.18 shows (a) the number of candidates per event, (b) the pseudorapidity η, (c) the azimuthal angle ϕ and (d) the transverse momentum. The distributions of the GMSB30 Monte Carlo sample include not only muons but also stable massive sleptons. Muons from the QCD events dominate up to $p_T = 40$ GeV while $W^{\pm}$ and $t\bar{t}$ processes dominate in the region $p_T > 40$ GeV. If sleptons exist in nature, the p_T distribution spreads up to high p_T region (~ 500 GeV) because their mother particles are massive. A candidate with $p_T \simeq 250$ GeV originated from 7 TeV collisions has been found in the p_T distribution.

Figure 7.19 (a) is the distributions of the quantity, $\Delta p/p$, defined as follows:

$$\frac{\Delta p}{p} = \frac{p_{\mathrm{ID}} - p_{\mathrm{MS}}^{\mathrm{extr}}}{p_{\mathrm{ID}}}, \tag{7.11}$$
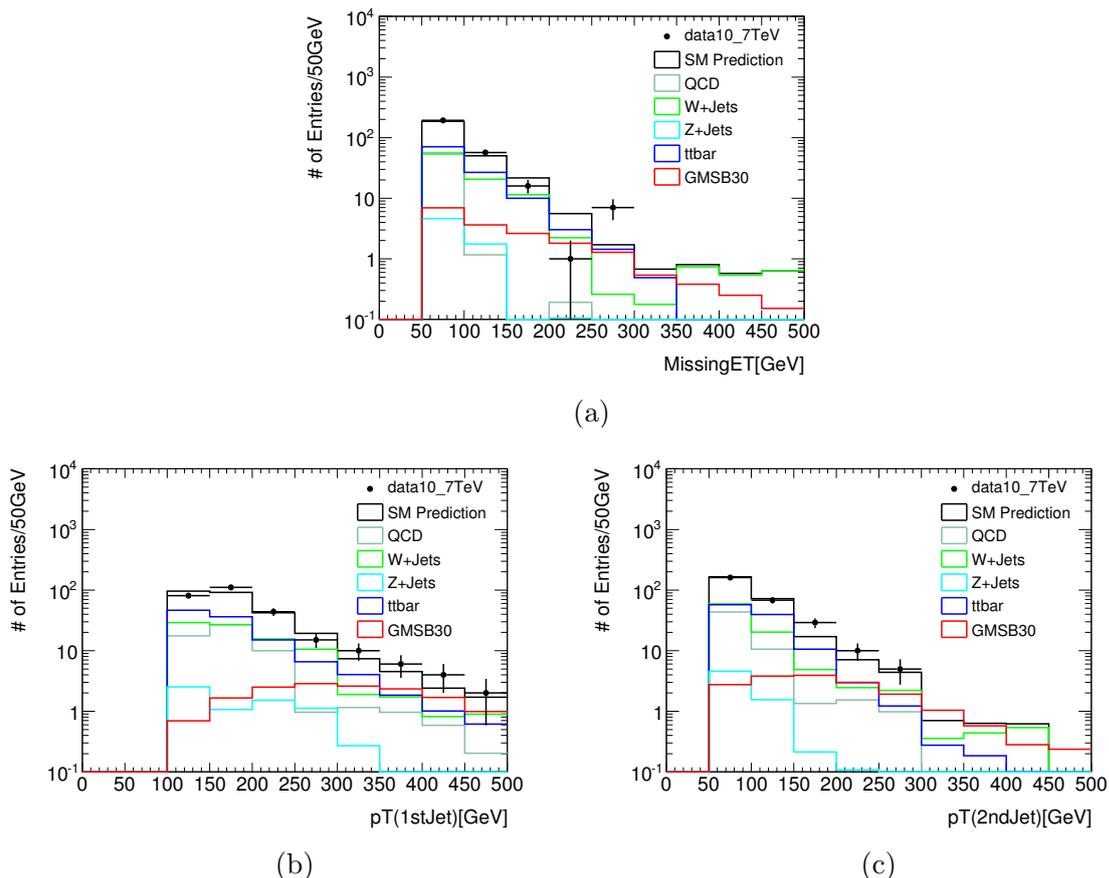
Figure 7.17: The missing transverse energy (a) and transverse momentum of 1st jet (b) and 2nd jet (c) distributions after the event and muon selection cut

where p_{ID} and $p_{\mathrm{MS}}^{\mathrm{extr}}$ are momentum of the ID track and the extrapolated MS track, which make up a combined muon track. In the case of well reconstructed combined tracks with low momentum, two momenta are similar. In fact, the values of $\Delta p/p$ of most of candidates are within ± 0.2. In addition, in the case of a decay muon from π/K, $\Delta p/p$ takes values much more than zero because p_{ID} is a momentum of π/K and $p_{\mathrm{MS}}^{\mathrm{extr}}$ is a momentum of muon, which may be generated from π/K decay in the calorimeters. This quantity is available for the reduction of decay muons [70]. The tail in the larger $\Delta p/p$ region may comes from decay muons.

Figure 7.19 (b) shows the transverse mass (m_T) distribution,

$$m_T^2 = 2\left(|\vec{p}_T^{\,\mathrm{muon}}||\vec{E}_T| - \vec{p}_T^{\,\mathrm{muon}}\vec{E}_T\right).\tag{7.12}$$

where p_T^{muon} is the transverse momentum of the muon with highest p_T in each event. A Jacobian peak from $W \to \mu\nu$ process is observed at $m_T \simeq 80$ GeV.

Figure 7.20 shows the distributions of measured β with MuonBetaRefitTool (a) and the time-of-flight information of the Tile Calorimeter (b). The mean value and the resolution for their β distributions are summarized in Table 7.8. The resolutions are worse than those
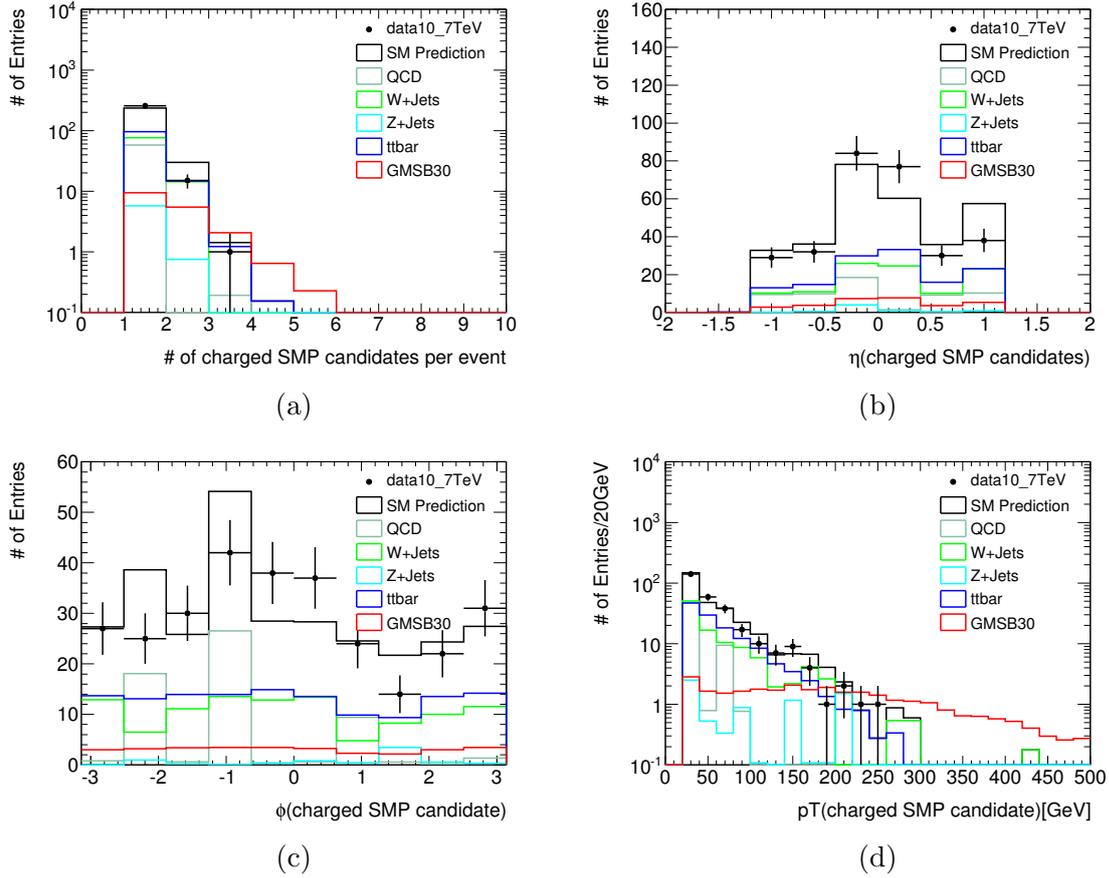
Figure 7.18: The missing transverse energy (a) and transverse momentum of 1st jet (b) and 2nd jet (c) distributions after the event and muon selection cut

of the Monte Carlo samples.

	mean value	resolution
MuonBetaRefitTool	1.03	0.10
Tile Calorimeter	1.00	0.11

Table 7.8: The measurement of β with MuonBetaRefitTool and the Tile Calorimeter.

However, the shapes of the tails are very different between the two independent β measurements. In the distribution of measured β with MuonBetaRefitTool, a flat tail exists up to $\beta = 0.8$ while there is no such a tail in that of the Tile Calorimeter. The Monte Carlo samples can describe the tail in both distributions reasonably well.

Figure 7.21 shows distributions of the calculated mass using measured β with (a) Muon-BetaRefitTool and (b) the time-of-flight information of the Tile Calorimeter. The distribution of mass measured with MuonBetaRefitTool for charged SMP candidates in data samples has a tail, which may be related to the β mis-measurements. The Monte Carlo
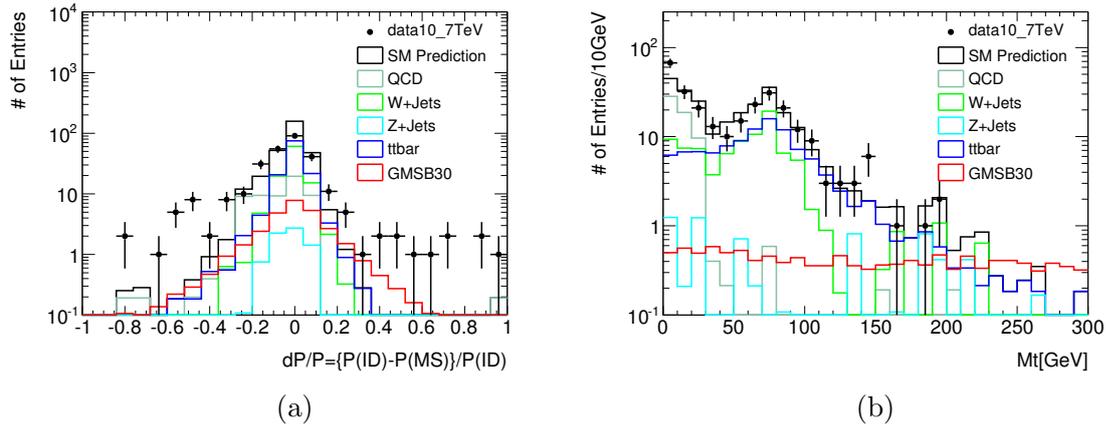
Figure 7.19: (a) $\Delta p/p$ and (b) the transverse mass m_T distributions.
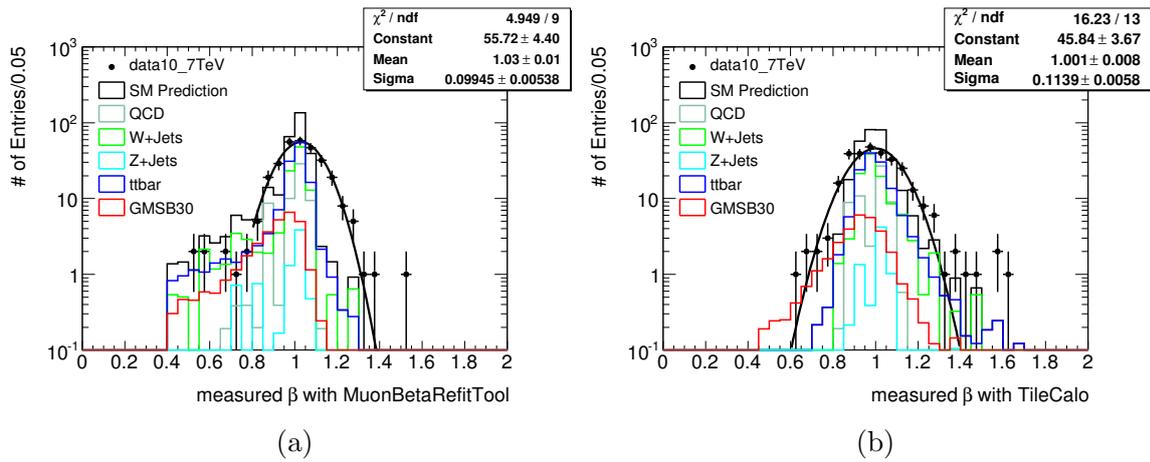
Figure 7.20: The results of β measurements with (a) MuonBetaRefitTool and (b) the Tile Calorimeter's information.
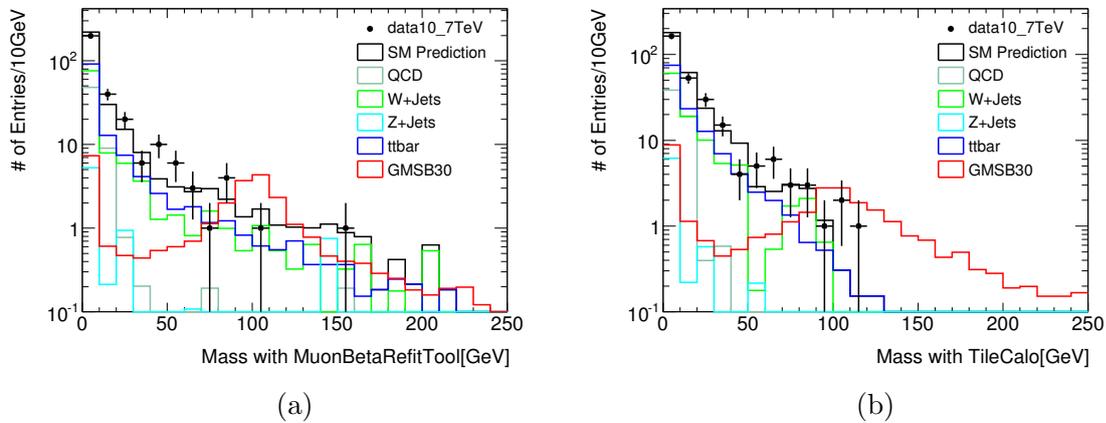

Figure 7.21: The results of mass measurements with (a) MuonBetaRefitTool and (b) the Tile Calorimeter's information.

samples can describe the tail reasonably well. Comparing the distributions of the mass measured with the two methods for candidates, the tail in the mass distribution measured with the Tile Calorimeter seems to be smaller than that of MuonBetaRefitTool.

The correlations between β_{refit} and β_{tile}, M_{refit} and M_{tile} are shown in the Fig. 7.22. Even if mass calculations are wrong due to the β mis-reconstruction with MuonBetaRe-fitTool, correct values can be mostly obtained with the Tile Calorimeter. The opposite is also true. Therefore, further reduction of muon backgrounds are expected by comparing measured masses with the two methods. If charged SMPs are reconstructed well with MuonBetaRefitTool and the Tile Calorimeter, it is expected that the plots line up on the diagonal in each distribution.


(a)   (b)
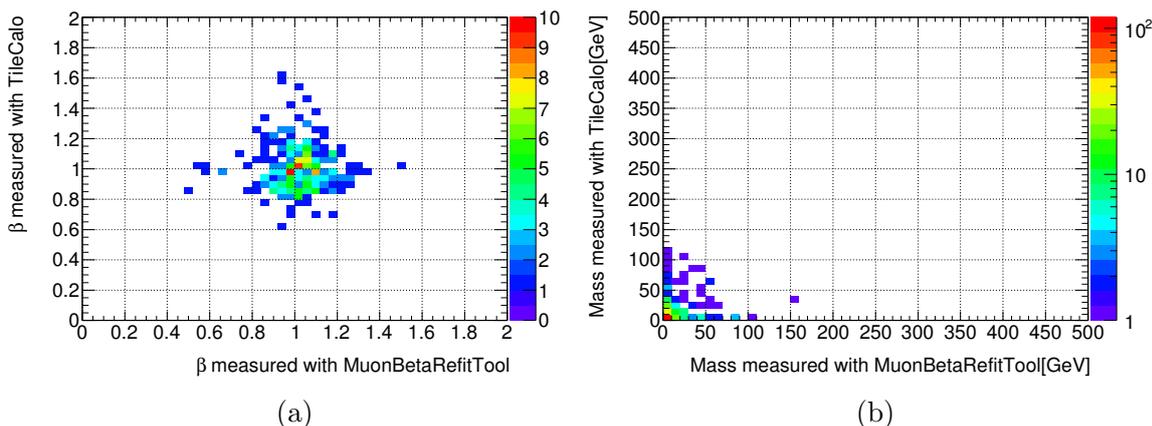
Figure 7.22: (a) β_{refit} vs β_{tile} and (b) M_{refit} vs M_{tile} for muons in the data sample.

7.9   Estimation of muon backgrounds

As described in the previous section, the shape of the β distribution (see Fig. 7.20) is very different between data and the Monte Carlo samples. Although the peak position of the β distribution in data is similar to that of the Monte Carlo samples due to the correction described in section 7.5, the resolution is worse than that of the Monte Carlo samples. Since the mis-measured β affects mass estimation, the accurate estimation of muon backgrounds using the Monte Carlo samples is not possible. Therefore, using muons in the control region defined below, a data-driven estimation of muon backgrounds has been performed. Muons are considered to be background muon if the following conditions are satisfied.

- Both β_{refit} and β_{tile}, which are measured β with MuonBetaRefitTool and Tile Calorimeter, respectively, are less than 0.8.

- Both measured masses with β_{refit} and β_{tile} are more than 90 GeV.

These conditions are the same as the final charged SMP selection criteria.

In order to obtain a background sample for the charged SMP candidate, the control region is defined as $\not{E}_T < 50$ GeV, $p_T^{\text{1stJet}} < 120$ GeV and $p_T^{\text{2ndJet}} < 50$ GeV. This region is expected to be dominated by the Standard Model processes. The data samples used
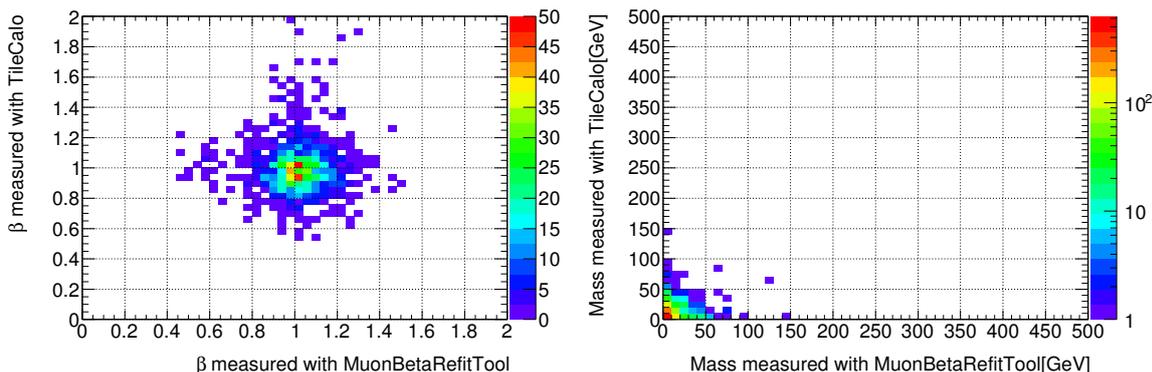
Figure 7.23: β_{refit} vs β_{tile} (left) and M_{refit} vs M_{tile} (right) for muons in the control region. The data samples were collected with the jet triggers.
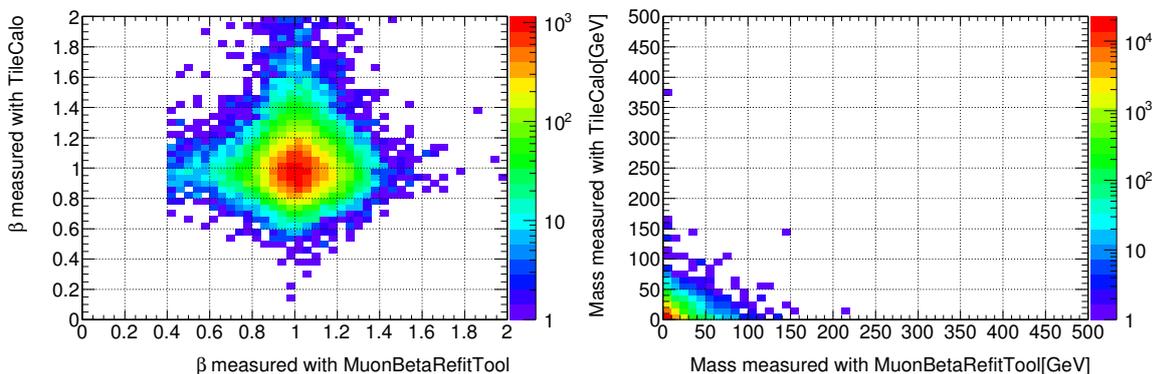
Figure 7.24: β_{refit} vs β_{tile} (left) and M_{refit} vs M_{tile} (right) for muons in the control region. The data samples were collected with the muon triggers.

for the calculation of the probability are the same data samples which are used in search for charged SMPs described in section 7.1. In addition, other data samples collected by the muon triggers are also used. The muon-trigger samples are expected to have a large number of pure muons by requiring muon with its transverse momentum larger than 13 GeV at the trigger level.

The left plot of Fig. 7.23 shows the correlation between β_{refit} and β_{tile}, and the right plot shows the correlation between M_{refit} and M_{refit} for muons in the control region of the data sample collected with the jet triggers. Similarly, Fig. 7.24 shows those of the data samples collected with the muon triggers.

Table 7.9 shows the total number of events with muons passing the muon selections described in section 7.6, the number of events with background muons, and the probability that muons become backgrounds. The probabilities are 0 % (Jet triggers) and 0.002 % (Muon triggers).

The nature of only one event with a background muon was investigated in detail. Table 7.10 shows the observed values for missing transverse energy, jets and muons for the

	total number of events with muons	number of events with background muons	ratio
Jet triggers	1,392	0	0 %
Muon triggers	41,083	1	0.002 %

Table 7.9: The data-driven estimation of muon backgrounds

event with the background muon. It can be seen that β_{refit} and β_{tile} correspond to each other approximately.

It is possible that the event has a cosmic muon. In general, cosmic muons run from the outer layer to the inner layer and traverse the ATLAS detector at the speed of the light. However, if events have cosmic muons, the ATLAS tracking algorithms including MuonBetaRefitTool reconstruct their tracks and measure wrong β assuming that they are generated from the proton-proton collision points. For example, if a cosmic muon fires the muon trigger of the RPC in the region of $\phi > 0$, the muon track in the region of $\phi < 0$ may be reconstructed with β less than 1.0 because the estimated arrival time of each hit on the muon track may be later than that of the muon generated from collisions. Figure 7.25 shows an event display of the event. The muon track is depicted using a green line. There is no other combined muon track back-to-back to the candidate track. It is unlikely that the candidate is a cosmic muon.

Run#	166658	$E_T^{\mathrm{cone0.2}}$	0.06 GeV
Event#	112729099	p_T	96.17 GeV
Event Stream	physics_Muons	p	119.18 GeV
$\not{E}_T$	27.48 GeV	p_{ID}	117.55 GeV
p_T^{1stJet}	64.49 GeV	$p_{\mathrm{MS}}^{\mathrm{extr}}$	2437.77 GeV
p_T^{2ndJet}	7.34 GeV	$\frac{p_{\mathrm{ID}} - p_{\mathrm{MS}}^{\mathrm{extr}}}{p_{\mathrm{ID}}}$	-19.74
η	0.68	β_{refit}	0.63
ϕ	100.00°	β_{tile}	0.64
θ	53.80°	M_{refit}	149.47 GeV
d_0	7.52×10^{-4} mm	M_{tile}	141.99 GeV
z_0	-17.69 mm	M_T	97.69 GeV
$z_0 - z_{\mathrm{pv}}$	3.49 mm		

Table 7.10: The event summary.

The background muon runs in the direction of $\theta = 53.80°$, which is just outside the $\theta = 60° \pm 5°$ cut, where the uncertainty on β is large.

Table 7.11 shows the energy deposit ΔE, the cell time t_{cell}, which is the energy deposit time offset with the arrival time of particle running at the speed of light (see Eq. 7.3), the measured time of energy deposition t_{meas} calculated by using Eq. 7.3, the distance to the interaction point d_{cell} and the velocity β_{cell} calculated with t_{cell} and d_{cell} by using Eq. 7.4 for all the cells associated with the muon track in the Tile Calorimeter. In this table, it can be seen that:
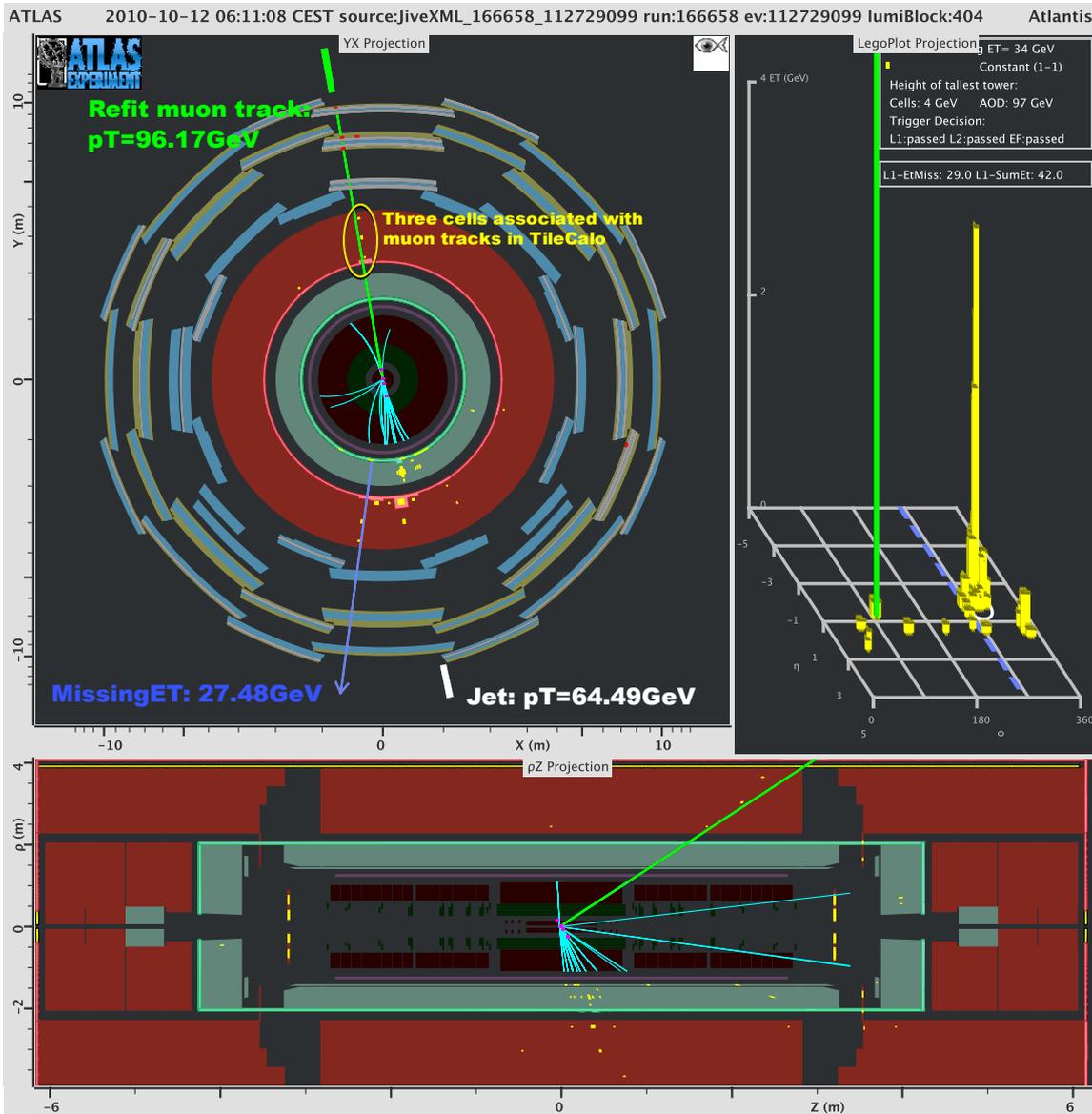
Figure 7.25: The event with muon, which is depicted by using green line, satisfying all selection criteria used in the search for charged SMPs (Run# 166658, Event# 112729099).

- The velocities β_{cell} of the cell #1 and cell #2 roughly take similar values. These values are also matched with β_{refit} reasonably well assuming that β_{refit} is correct. On the other hand, β_{cell} of the cell #3 is very different from other two cells.

- Although the cell #3 is far away from the proton-proton interaction point, the measured time (t_{meas}) when muon deposits its kinetic energy in the cell #3 is earlier than that of the cell #2.

As described in section 7.4.3, the presence of cells with negative β_{cell} shows poor calibration of Tile Calorimeter. In such a situation, since the β_{cell} value of the cell #3 is larger than that of the cell #1 and #2, the uncertainty on β_{tile} may be large.

	ΔE	t_{cell}	t_{meas}	d_{cell}	β_{cell}
cell#1	0.31 GeV	5.83 nsec	15.77 nsec	2.98 m	0.63
cell#2	1.74 GeV	9.57 nsec	21.84 nsec	3.68 m	0.56
cell#3	1.21 GeV	2.49 nsec	16.98 nsec	4.34 m	0.85

Table 7.11: The status of the cells in the Tile Calorimeter associated with the muon track (Run# 166658, Event# 112729099).

From the fake charged SMP background probability measured by using the muon trigger sample, expected number of background events among the selected charged SMP candidate can be estimated, assuming that the probability to have charged SMP fake signal are the same for the muon sample and charged SMP signal sample of 273 events. The expected number of muon background events is 0.005 when the probability calculated by the muon trigger sample is used. It can be concluded that the background events due to the fake charged SMP signal are negligible.

7.10 The event passing all selection criteria

A search for charged SMPs has been performed by requiring the following final selection criteria:

- As seen in Fig. 7.20, the Gaussian distribution fitting each β distribution for charged SMP candidates in data is broad in the region $\beta > 0.8$. There may be muons in the range of $\beta > 0.8$. To avoid fake charged SMP signals due to muons, both measured velocities, β_refit and β_tile, with the two β measurement methods are required to be less than 0.8.

- Since charged SMPs with the mass below 100 GeV has been excluded by the previous searches at LEP, both measured masses with β_refit and β_tile are required to be more than 90 GeV. The mass cut value in the final selection will be changed with respect to the mass of charged SMPs which are targets in search.

All event selection criteria used in the search for charged SMPs are summarized in Table 7.12.

Event selection	Jet Trigger
	$\not{E}_T > 50$ GeV
	$p_T^\text{1stJet} > 120$ GeV, $p_T^\text{2ndJet} > 50$ GeV, $\|\eta\| < 2.5$
Charged SMP selection	$\|z_0 - z_\text{pv}\| < 20$ mm, $p_T^\text{track} > 20$GeV, $\|\eta\| < 1.7$,
	The velocities, β_refit and β_tile, can be measured.
	$\beta_\text{refit} > 0.4$, $N_\text{hits}^\text{MDT} \geq 10$,
	$N_\text{cell}^\text{TileCalo} \geq 2$,
	Muons associated with cells with $\beta_\text{cell} < 0$ are rejected.
	$140° < \theta < 145°$, $60° < \phi < 80°$ are rejected.
	$\theta = 30° \pm 5°, 60° \pm 5°, 120° \pm 5°, 150° \pm 5°$ are also rejected.
Final selection	$\beta_\text{refit} < 0.8$, $\beta_\text{tile} < 0.8$.
	$M_\text{refit} > 90$ GeV, $M_\text{tile} > 90$ GeV (e.g. GMSB30)

Table 7.12: The summary of event selection criteria in the search for charged SMPs assuming that charged SMPs are generated based on the prediction of GMSB30 Monte Carlo simulation.

Table 7.13 shows the number of events which have muons satisfying the final selection criteria for the signal (GMSB30), the background and the data. There are no events remained after the final selection in the data, while 0.03 events are predicted from the standard model background simulation, which comes from the top quark pair production. For the GMSB30 model, 2.87 events are predicted. Figure. 7.26 shows the distribution of the measured mass with β_refit after the final event selection.

Table 7.14 shows the summary of the background event from the top quark pair production. There is a reconstructed track whose velocities measured with MuonBetaRefitTool and Tile Calorimeter are $\beta_\text{refit} = 0.73$ and $\beta_\text{tile} = 0.76$, respectively.

It is obvious that there are no charged SMPs in the event because this is a Monte Carlo event of top pair production. Therefore, it should be just accidental that the track

	Signal (GMSB30)	Background	Data
# of events	2.87	0.03	0

Table 7.13: The number of events satisfying all event selection criteria and the predictions from the Monte Carlo samples.
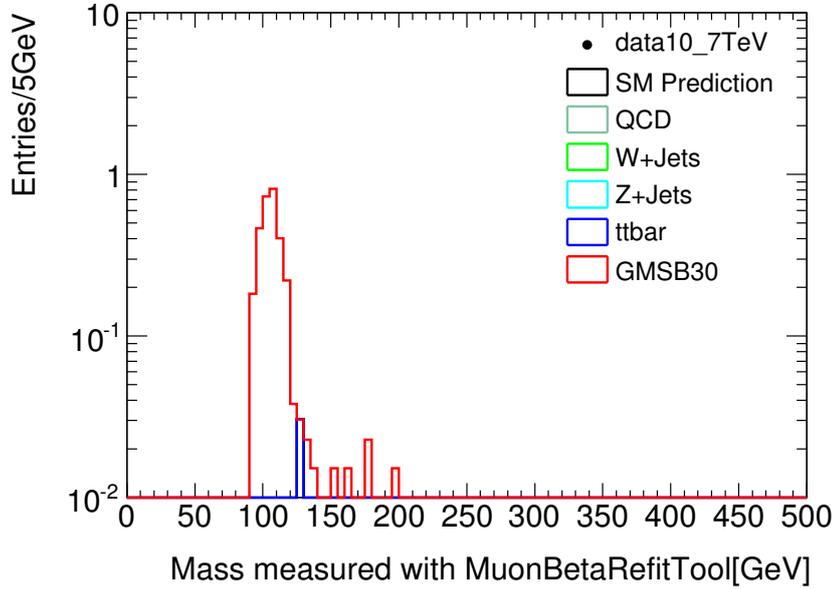

Figure 7.26: The distribution of measured mass with MuonBetaRefitTool after applying the final selection criteria.

Run#	150200	$E_T^{\text{cone}0.2}$	0.04 GeV
Event#	145633	p_T	130.6 GeV
Event Stream	—	p	132.2 GeV
$E̸_T$	100.1 GeV	p_{ID}	130.74 GeV
p_T^{1stJet}	153.6 GeV	$p_{\text{MS}}^{\text{extr}}$	155.6 GeV
p_T^{2ndJet}	62.7 GeV	$\frac{p_{\text{ID}}-p_{\text{MS}}^{\text{extr}}}{p_{\text{ID}}}$	0.2
η	−0.2	β_{refit}	0.73
ϕ	39.2°	β_{tile}	0.76
θ	99.1°	M_{refit}	125.2 GeV
d_0	4.7×10^{-3} mm	M_{tile}	113.1 GeV
z_0	−8.9 mm	M_T	195.7 GeV
$z_0 - z_{\text{pv}}$	0.1 mm		

Table 7.14: The event summary of $t\bar{t}$ background (MC).

	η	ϕ	dR	p	p_T
reconstructed	-0.159	0.683	7.75×10^{-4}	132.25 GeV	130.58 GeV
truth	-0.159	0.684	—	137.94 GeV	136.22 GeV

Table 7.15: The comparison of reconstructed value (η, ϕ, p and p_T) with true value from Monte Carlo simulation.

is reconstructed with other hit patterns in the MDT by using the assumption of a lower β value. The track may not be able to be matched with any truth muon tracks. To ensure it, the reconstructed track is tried to match with the truth muon tracks by using the distance between the track and the truth muon track in η-ϕ plane, dR, defined as $dR = \sqrt{d\eta^2 + d\phi^2}$. Table 7.15 shows the comparison of reconstructed values, η, ϕ, p and p_T, with true values from Monte Carlo simulation. It is concluded that the reconstructed track with lower β is matched with truth muon track.

The muon runs in the direction of $\theta = 99.1°$, where MuonBetaRefitTool is usually expected to have sensitivity of the β measurement. Table 7.16 shows detailed information on the cells in the Tile Calorimeter associated with the muon tracks, which have been used in calculation of β_{tile}. The timing mis-measurements of cells in the Tile Calorimeter are also simulated by Monte Carlo simulation.

Although further reduction of muons is performed by using tight selection with measured β and mass, this top quark pair production event shows that a muon running in the direction, where both MuonBetaRefitTool and the Tile Calorimeter usually measure its β correctly, may become a fake charged SMP because both β_{refit} and β_{tile} are wrong due to mis-measured timing of detectors. The Monte Carlo samples predict to find more than one fake signal event with muons satisfying the condition described above at thirty times the integrated luminosity used in this analysis.

	ΔE	t_{cell}	t_{meas}	d_{cell}	β_{cell}
cell#1	0.27 GeV	6.76 nsec	16.95 nsec	3.05 m	0.61
cell#2	0.42 GeV	1.94 nsec	14.37 nsec	3.72 m	0.86

Table 7.16: The status of the cells in the Tile Calorimeter associated with the muon track.

7.11   Limit on production cross section of charged SMPs

No charged SMP candidates satisfying all selection criteria including the final selection have been observed. With these numbers, the 95 % confidence level upper limit on the production cross section for a hypothetical charged SMP has been set by using the Bayesian approach. Note that this is not a generic charged SMP search but a model-dependent search because the GMSB model is used as the signal sample and jet and missing transverse energy are required in event selection.

For each of charged SMP candidates, a likelihood function L is defined as a product of Poisson factors computed for each bin i of the mass distribution (e.g. Fig. 7.26):

$$L(s) = \prod_i \frac{(s_i + b_i)^{d_i}}{d_i!} e^{-(s_i+b_i)} = e^{-(s+b)} \prod_i \frac{(f_i s + b_i)^{d_i}}{d_i!}, \qquad (7.13)$$

$$b = \sum_i b_i, \qquad (7.14)$$

$$s = \sum_i s_i, \qquad (7.15)$$

$$f_i = \frac{s_i}{s}, \qquad (7.16)$$

where d_i, b_i and s_i are the observed number of data events, the backgrounds and the predicted signals in bin i, respectively, s and b are the total number of the backgrounds and the predicted signals and f_i is the scale factor in order to normalize the number of the signal events in bin i.

The 95 % confidence level upper limit on the signal events $s_{\rm up}$ can be determined with the following equation:

$$\frac{\displaystyle\int_0^{s_{\rm up}} L(s)ds}{\displaystyle\int_0^{+\infty} L(s)ds} = 0.95. \qquad (7.17)$$

This equation has been solved by using a numerical integration method. Using the $s_{\rm up}$, The 95 % C.L. upper limit on the production cross section $\sigma_{\rm up}$ can be determined:

$$s_{\rm up} = \int \mathcal{L}dt \times \sigma_{\rm up} \times \mathcal{A} \qquad (7.18)$$

The integrated luminosity is 37.4 pb^{-1}. The acceptance $\mathcal{A}$ is defined as the number of the signal events with at least one charged SMP satisfying the all selection criteria divided by the total number of the signal events. $\mathcal{A}$ has been calculated by using the GMSB Monte Carlo samples.

Table 7.17 and Fig. 7.27 show the observed 95 % C.L. on the production cross section as a function of the charged SMP mass, assuming the GMSB model as described in section 4.2. The upper limit on the production cross section is about 2 pb, with little dependence on the charged SMP mass in the range of the search. The lower limit on mass of charged SMPs was measured about 101 GeV in this analysis at 95 % C.L., assuming the GMSB cross section as the source of the charged SMP production. However, the lower limit on the mass of charged SMPs, which was set to be 102.0 GeV at the LEP experiment, is not be updated (see Fig. 7.28).

	GMSB30	GMSB35	GMSB40	GMSB50	GMSB60
$M_{\tilde{\tau}}$ [GeV]	101.3	116.3	131.0	160.7	190.7
Mass cut window [GeV]	90 - 500	100 - 500	110 - 500	130 - 500	160 - 500
Acceptance	3.69 %	3.52 %	3.73 %	4.10 %	4.54 %
Signal	2.87	1.21	0.61	0.19	0.08
Background	0.03	0.03	0.03	0	0
Data	0	0	0	0	0
σ(95% C.L.) [pb]	2.17	2.28	2.14	1.95	1.76
σ(theory) [pb]	2.00	0.84	0.39	0.11	0.04

Table 7.17: The 95 % C.L. upper limit on the production cross section.
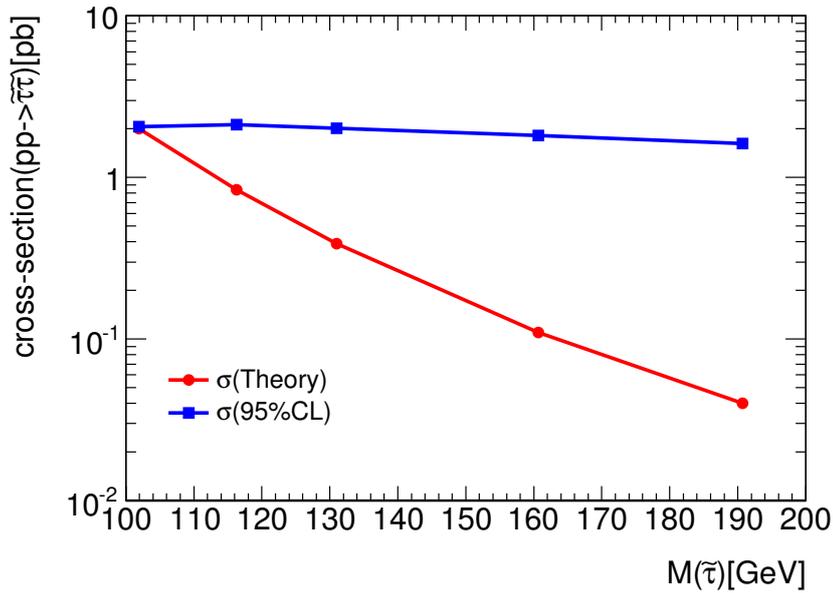
Figure 7.27: The 95 % C.L. upper limit on the production cross section as a function of tau-slepton mass.
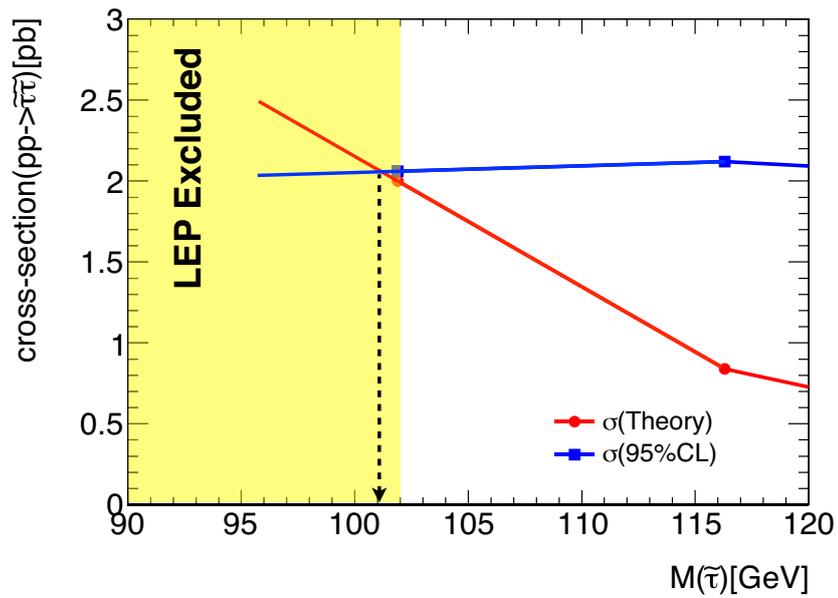
Figure 7.28: The lower limit on mass of scalar tau was measured about 101 GeV in this analysis, which could not exceed the LEP limit.

Chapter 8

Summary

Charged stable massive particles predicted by some models of beyond the Standard Model are expected to generate with high transverse momentum in proton-proton collisions at the LHC and behave as "slowly-moving heavy muons" in the ATLAS muon spectrometers.

The ATLAS standard muon track reconstruction algorithm reconstructs muon tracks by using drift circles of the MDT calculated with an assumption of $\beta = 1.0$. If charged SMPs reach the muon spectrometers, their tracks are reconstructed as muons. However, the drift circles for the charged SMPs are reconstructed larger than the real drift circles due to late arrival in the muon spectrometers. To reconstruct charged SMPs by finding an optimal β correctly, MuonBetaRefitTool has been developed and implemented in the ATLAS event reconstruction software.

A performance study has been performed using the GMSB Monte Carlo samples, where two charged massive sleptons are generated from cascade decay of gluinos and/or squarks. MuonBetaRefitTool can reconstruct the sleptons well. The velocity β of sleptons is measured to 3 to 5 % accuracy. The efficiency of β reconstruction is about 90 % in $\beta > 0.5$. However, sleptons running in the direction of $\theta = 30°$, $60°$, $120°$ and $150°$ are often mis-reconstructed. The β mis-measurements are related to the structure of the MDT. MuonBetaRefitTool also measures the mass of sleptons with 8 % accuracy.

The LHC has started physics run at the center of mass energy of 7 TeV with a luminosity of 10^{31}cm^{-2}sec^{-1} from March, 2010. The performance study of MuonBetaRefitTool has been performed with high-purity muons collected by the muon triggers. The peak of measured β distribution was shifted toward higher β. The resolution of measured β is worse than that of the Monte Carlo simulation. In addition, it is found that there are other regions where MuonBetaRefitTool dose not have accuracy on the β measurement in addition to the regions around $\theta = 30°$, $60°$, $120°, 150°$. Since the β measurement affects mass estimation directly, these regions are excluded in the search of charged SMPs.

Using the data samples collected by jet triggers, a search for charged SMPs has been performed assuming that charged SMPs are generated based on the prediction of GMSB models. Missing transverse energy and two jets with high transverse momentum were required in order to increase the signal sensitivity. The velocity β of muons is also measured using time-of-flight information of Tile Calorimeter to reduce the muon backgrounds further. Since the resolution of measured β with MuonBetaRefitTool and Tile Calorimeter are found to be larger than that of the Monte Carlo samples, the signal is selected by requesting β well away from the background peak. No events satisfy all selection criteria

in data. A 95 % C.L. upper limit on the production cross section is obtained. The lower limit on the mass of charged SMPs is not updated due to a finite amount of data which are available for this analysis. The LHC will collect much more data of 7 TeV collision, which will correspond to an integrated luminosity of 1 fb^{-1}. The update of lower limit on their mass is expected in near future.

Acknowledgement

References

[1] S.Weinberg, Phys. Rev. Lett. **19** (1967) 1264

[2] A.Salam, "Elementary Particle Theory", ed. N.Svartholm (Almquist and Wiksells, Stockholm, 1968) 367

[3] S.L.Glashow, J.Iliopoulos and L.Maiani, Phys. Rev. **D2** (1970) 1285

[4] K. Nakamura et. al (Particle Data Group; PDG), Journal of Physics G **37** 075021 (2010).

[5] P.W. Higgs, "Broken symmetries, massless particles and gauge fields", Phys. Lett. **12** (1964) 132-133.

[6] P. W. Higgs, "Spontaneous symmetry breakdown without massless bosons", Phys. Rev. **145** (1966) 1156-1163.

[7] P. W. Higgs, "Broken symmetries and the masses of gauge bosons", Phys. Rev. Lett. **13** (1964) 508-509.

[8] LEP Collaborations and LEP Electroweak Working Group, "A Combination of Preliminary Electroweak Measurements and Constraints on the Standard Model", LEPEWWG/2005-01, hep-ex/0511027, 9 November 2005

[9] J.F.de Troconiz and F.J.Yndurain, Phys. Rev. **D71** (2005) 073008.

[10] Krisztian Peters, "Higgs Searches" arXiv:0911.1469 (hep-ex), November 2010.

[11] Bernd Stelzer, "Review of Top Quark Measurement" arXiv:1004.5368 (hep-ex), April 2010.

[12] Pierre Pétrof, "W and Z production and properties", in2p3-00472101, April 2010.

[13] M.Spira and P.M.Zerwars, "Electroweak Symmetry Breaking and Higgs Physics", hep-ph/9803257 (1997)

[14] S.Asai et al., "Prospects for the Search for a Standard Model Higgs Boson in ATLAS using Vector Boson Fusion", Eur. Phys. J. **C32S2** (2004) 19-54

[15] J. Wess and B. Zumino, Nucl Phys. B70, (1974) 39.

[16] P. Fayet and S. Ferrara, Phys. Rep. 32, (1977) 249.

113

[17] H. P. Nilles, Phys. Rep. 110, (1984) 1.

[18] H, Haber and G. Kane, Phys. Rep. 117, (1985) 75.

[19] R, Barbieri, Riv. Nuovo Cimento. 11, (1988) 1.

[20] W. de Boer and C. Sander, Phys. Lett. B585 (2004) 276.

[21] J. R. Ellis, S. Heinemeyer, K. Olive and G. Weiglein, JHEP 0502 (2005) 13.

[22] H. Baer, C. H. Chen, F. Paige and X. Tera, Phys. Rev. D52, (1995) 2746.

[23] A. Chamseddine, R. Arnowitt and P. Nath, Phys. Rev. Lett. 49 (1982) 970.

[24] R. Barbieri, S. Ferrara and C. Savoy, Phys. Lett. B119 (1982) 343.

[25] N. Ohta, Prog. Theor. Phys. 70 (1983) 542.

[26] L. Hall, J. Lykken and S. Weinberg, Phys. Rev. D27 (1983) 2359.

[27] L. Randall, and R. Sundrum, Nucl. Phys. **B557** (1999) 79.

[28] G. F. Giudice, M. A. Luty. H. Murayama and R. Rattazzi, JHEP **9812** (1998) 027.

[29] M. Dine and A. Nelson, Phys. Rev. **D48** (1993) 1277.

[30] M. Dine , A. Nelson, Y. Nir and Y. Shirman, Phys. Rev. **D53** (1996) 2658.

[31] S.Yamamoto, "Strategy for early SUSY searches at ATLAS", ATL-PHYS-CONF-2008-001; ATL-COM-PHYS-2007-081

[32] M. Fairbairn, A.C. Kraan, D.A. Milstead, T. Sjöstrand, P. Skands and T. Sloan, "Stable massive particles at colliders", PhysicsReports 438(2007)1?63

[33] CERN Public home, http://public.web.cern.ch/public/

[34] LHC Design Report, CERN/-2004-003, 4 June 2004.

[35] Luminosity and Run Statistics Plots for 2010 Beam Data, https://twiki.cern.ch/twiki/bin/view/AtlasPublic/RunStatsPublicResults2010

[36] ATLAS Collaboration, ATLAS DETECTOR AND PHYSICS PERFORMANCE Technical Design Report Volume I, CERN/LHCC/99-14 ATLAS TDR (1999)

[37] ATLAS Collaboration, Calorimeter Performance Technical Design Report, CERN/LHCC 96-40 (1997).

[38] ATLAS Collaboration, Muon Spectrometer Technical Design Report, CERN/LHCC 97-22 (1997).

[39] ATLAS Collaboration, The ATLAS Experiment at the CERN Large Hadron Collider, JINST 3 S08003 (2008)

[40] ATLAS Collaboration, ATLAS Trigger Performance Status Report, CERN/LHCC 98-15 (1998)

[41] ATLAS Collaboration, ATLAS Level1 Trigger Technical Design Report, ATLAS TDR-12 (1998)

[42] T. Sjostrand, and S. Mrenna and P. Skands, JHEP **05** (2006) 026.

[43] G. Corcella et al., JHEP **01** (2001) 010; G. Corcella et al., "HERWIG 6.5 release note", hep-ph/0210213, 2002.

[44] J. Butterworth, J. Forshaw and M. Seymour, Z. Phys. **C72** (1996) 637?646.

[45] The ATLAS collaboration, "ATLAS Monte Carlo tunes for MC09", ATL-PHYS-PUB-2010-002, 2010.

[46] S. Agostinelli et al., Nucl. Instrum. Meth. A506 (2003) 250?303.

[47] A. Sherstnev and R.S. Thorne, Eur. Phys. J. **C55** (2008) 553?575.

[48] M. Mangano et al., JHEP **07** (2003) 001.

[49] D. Stump et al., JHEP **10** (2003) 046.

[50] C. Anastasiou, L.J. Dixon, K. Melnikov, and F. Petriello, Phys. Rev. **D69** (2004) 094008.

[51] S. Frixione and B.R. Webber, The MC@NLO 3.2 event generator, hep-ph/0601192, 2006.

[52] S. Frixione and B.R. Webber, JHEP **06** (2002) 029.

[53] S. Moch and P. Uwer, Nucl. Phys. Proc. Suppl. **183** (2008) 75?80.

[54] F.E. Paige, S.D. Protopopescu, H. Baer, and X. Tata, "ISAJET 7.69: A Monte Carlo event generator for p p, anti-p p, and e+ e- reactions, hep-ph/0312045, 2003

[55] The CDF Collaboration, "Search for charged massive stable particles", CDF note 8701, February 2007.

[56] The D0 Collaboration, "A Search for Charged Massive Stable Particles at D0", D0note 4746-CONF, March 2005.

[57] Niels van Eldik, "The ATLAS muon spectrometer: calibration and pattern recognition", Ph.D thesis, NIKHEF, 2007.

[58] Jochem Snuverink, "THE ATLAS MUON SPECTROMETER: COMMISIONING AND TRACKING", Ph.D thesis, 2009.

[59] J. Illingworth and J.Kittler, "A survey of the hough transform", Computer Vision, Graphics and Image Processing **44** (1988) 87.

[60] A.J. Storkey, N.C. Hambley, C.K.I. Williams, and R.G. Mann, "Cleaning sky survey data bases using Hough transform and renewal string approaches", Monthly Notices of the Royal Astronomical Society **347** (2004) 36.

[61] P.V.C. Hough, "Machine Analysis of Bubble Chamber Pictures", In International Conference on High Energy Accelerators and Instrumentation, CERN, 1959.

[62] P.V.C. Hough, "Methods and means to recognize complex patterns", 1962, U.S. Patent No. 3069654.

[63] Dimitrios Fassouliotis, Theodota Lagouri, Alan Poppleton, Simon Robins, Giorgos Stavropoulos and Irene Vichou, "Muon Identification using the MUID package", ATL-COM-MUON-2003-003.

[64] S. Hassani, L. Chevalier, E. Lanc-on, J.-F. Laporte, R. Nicolaidou and A. Ouraou, "A muon identification and combined reconstruction procedure for the ATLAS detector at the LHC using the (MUONBOY, STACO, MuTag) reconstruction packages", Nuclear Instruments and Methods in Physics Research A 572 (2007) 77-79.

[65] M. Cacciari, G.P. Salam and G. Soyez, JHEP **04** (2008) 063.

[66] W. Lampl et al., Calorimeter Clustering Algorithms: Description and Performance, Internal Report ATL-LARG-PUB-2008-002, CERN, Geneva, Apr 2008.

[67] The ATLAS collaboration, "Jet energy scale and its systematic uncertainty in ATLAS for jets produced in proton-proton collisions at $\sqrt{s} = 7$ TeV", ATLAS-CONF-2010-056, June 2010.

[68] The ATLAS collaboration, "Readiness of the ATLAS Tile Calorimeter for LHC collisions", The European Physical Journal C (2010) 70: 1193-1236, November 2010.

[69] S. Hellman, M. Johansen, R. Mackeprang, P. Mermod, D. Milstead, C. Ohm and A. Solodkov, "Measuring time-of-flight and identifying exotic stable massive particles with the ATLAS Tile calorimeter", ATL-COM-TILECAL-2009-028, September 2010.

[70] The ATLAS Collaboration, "Measurement of the $W \to \ell\nu$ and $Z \to \ell\ell$ production cross-sections in proton-proton collisions at $\sqrt{s} = 7$ TeV with the ATLAS detector", arXiv:1010.2130 [hep-ex] (2010)

[71] ATLAS Collaboration, "Early supersymmetry searches in channels with jets and missing transverse momentum with the ATLAS detector", ATLAS-CONF-2010-065, July 2010.

[72] ATLAS Collaboration, "Early supersymmetry searches with jets, missing transverse momentum and one or more leptons with the ATLAS Detector", ATLAS-CONF-2010-066, July 2010.

[73] Naoko Kanaya, "Search for Supersymmetric Particles with the OPAL Detector at LEP2", Ph.D thesis, Kobe University, 2002.

[74] Hironori Kiyamura, "Study of ATLAS LVL1 Muon Trigger Performance using Dimuon events", Ph.D thesis, Kobe University, 2009.

[75] Chihiro Omachi, "Study of muon trigger performance with the ATLAS detector at the LHC", Ph.D thesis, Kobe University, 2010.